Master of Science Thesis

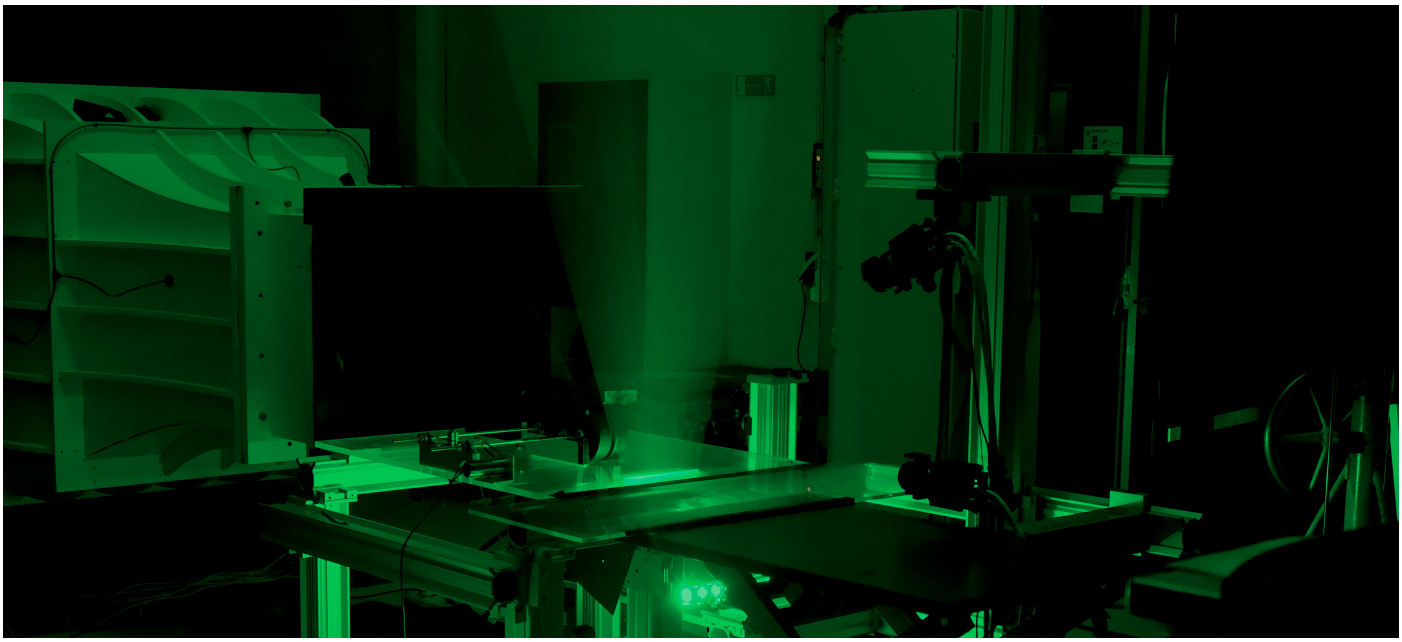

Aerodynamics of trailer wheels in tandem:

Experimental investigation into the effects of wheel rotation, trailer side-skirts, and wheel cavity covers

Rishabh Jakhar

Aerodynamics

TU Delft

Faculty of Aerospace Engineering

Delft University of Technology

Aerodynamics of trailer wheels in tandem:
Experimental investigation into the effects of wheel rotation, trailer side-skirts, and wheel cavity covers

Master of Science Thesis

To obtain the degree of Master of Science in Aerospace Engineering at the Delft University of Technology

Rishabh Jakhar

30th September 2021

Thesis committee:	Dr. A. Sciacchitano	TU Delft - Aerodynamics (supervisor)
	R. Veldhuizen	Wabco
	E. Saredi	TU Delft - Aerodynamics
	Dr. B.W. van Oudheusden	TU Delft - Aerodynamics
	Dr. G.E. Elsinga	TU Delft - 3mE

TU Delft Delft University of Technology

Preface

As this thesis, and with it my master's study in aerodynamics, comes to an end, I would like to take a moment to thank the people who contributed to its success.

Firstly, I would like to thank my daily supervisor, Dr. Andrea Sciacchitano, for the knowledge he chose to share with me and for the direction he provided to the project. I thank Roy Veldhuizen, both for motivating the topic of research for this thesis, and for all the valuable input provided since. My gratitude also goes to Edoardo Saredi, without whom a successful experimental campaign would not be possible.

Secondly, I would like to thank the staff of the aerodynamic laboratories: Frits Donker Duyvis, Peter Duyndam, Dennis Bruikman, and Nico van Beek. The importance of their expert and timely help cannot be overstated.

Finally, I would like to thank my parents, and my sister, for their unrelenting support during my endeavors. None of this would be possible without them, and therefore, to them, I owe the highest debt of gratitude.

Rishabh Jakhar
Delft, September 2021

Abstract

The increasing importance of drag reduction in commercial vehicles, traditionally motivated by rising energy costs, and more recently accelerated through policymaking in a bid to reduce emissions, has resulted in the development of increasingly sophisticated add-on aerodynamic devices for the semi-trailer. Of these devices, the greatest uptake amongst trucking fleets has been for devices fitted to the underbody, primarily on account of allowing free movement of freight into and out of the trailer, hence incentivizing a better understanding of the flowfield in this region. The current research addresses the aerodynamics of trailer wheels in tandem, which form a key component of the semi-trailer underbody, by investigating the effects of wheel rotation, trailer side-skirts, and wheel cavity covers on the flowfield and drag. The configurations tested include a short side-skirt terminating before the front edge of the leading wheel, a long side-skirt covering both the wheels, wheel covers without openings (solid disks), and wheel covers with openings varying in coverage area and radial position.

Stereoscopic (2D-3C) PIV is applied to examine the flow topology in the near wake and on selected planes besides the wheels. The measured velocity data in the wake is further used to derive the pressure field (by solving the Poisson equation for pressure), which together are then used to calculate the drag using a control volume approach. The uncertainty in the derived pressure field and drag values is determined using linear uncertainty propagation.

The largest drag reduction from the baseline case, i.e. without a side-skirt or wheel covers, is seen for the long side-skirt, followed by the short side-skirt with wheel covers, short side-skirt only, and wheel covers only, in that order. The effectiveness of both the long side-skirt and wheel covers is seen to increase with wheel rotation, with an appreciable reduction in drag with the wheel covers fitted only seen for rotating wheels. Investigation of the flowfield in the wake shows significant differences between the stationary and rotating wheel, particularly within the region of the projected wheel profile, and indicates to an earlier separation of flow along the upper surface of the rotating wheel. The effect of the side-skirt on the velocity in the wake is seen primarily in a lower streamwise velocity deficit, narrower wake, and higher horizontal symmetry of the wake for the skirted configuration. Wheel covers show a comparatively limited effect on the velocity field in the wake, showing a marginally wider wake and a slightly higher velocity deficit for the uncovered wheel. On planes beside the wheels, the side-skirt and wheel covers show a greater influence than wheel rotation, considered to be a consequence of a static floor combined with a gap between the wheel and the ground. The non-skirted configurations here exhibit a larger region of separated flow and greater velocity deficit whereas the uncovered wheels

show an outflow at the bottom of the wheel cavity and an inflow at the top. Finally, the wheel covers with openings show a behavior between that of a covered and an uncovered wheel, with the inflow/outflow depending significantly on the coverage percentage and radial position.

Contents

Nomenclature

Abbreviations

CARB	California Air Resources Board
COE	Cab over engine
CVP	Counter-rotating vortex pair
DOE	Department of Energy
GCM	Generalized Conventional Model
GHG	Greenhouse gas
LDA	Laser Doppler Anemometry
LIC	Line Integral Convolution
NRC	National Research Council of Canada
PIV	Particle Image Velocimetry
RANS	Reynolds-averaged Navier-Stokes
SORHT	SOLUS and ODU representative Heavy Truck
TKE	Turbulent Kinetic Energy

Mathematical Symbols

ΔT	Time interval between image pairs
Δt	Pulse separation
δt	Pulse duration (pulse width)
δz	Focal depth
$\mathbf{U}_p$	Tracer particle velocity
$\mathbf{U}_s$	Slip velocity
$\overline{p}$	Mean pressure
$\overline{u},\ \overline{v},\ \overline{w}$	Mean velocity terms
ρ_p	Particle density
τ	Tunnel shape factor
τ_s	Relaxation time
ε_n	Nozzle blockage correction factor
ε_{qn}	Nozzle blockage factor
ε_s	Jet expansion correction factor
C	Duplex nozzle exit area

C_e	Effective nozzle area
D	Wheel diameter
d_τ	Particle image diameter
d_p	Particle diameter
d_s	Diffraction-limited spot diameter
f	Focal length of the lens
$f_\#$	Aperture number or f-stop number
g	Wheel to ground gap
L	Model length
M	Optical magnification
p	Pressure
p'	Fluctuating pressure
p_∞	Freestream pressure
S	Duplex model area
S_k	Particle Stokes number
$u,\ v,\ w$	Velocity components in $x,\ y,\ z$ directions respectively
$u',\ v',\ w'$	Fluctuating velocity terms
U_∞	Freestream velocity
V	Model volume
W	Wheel width
x_m	Distance from center of the model to the nozzle
Z_o	Image distance
z_o	Object distance

List of Figures

List of Tables

Chapter 1

Introduction

Drag reduction of commercial vehicles has long been accepted as a worthy goal for both economic and societal reasons. Historically it has been motivated by rising energy costs and lately also by the increasing environmental constraints. At highway speeds of around $25\ m/s$ $(90\ km/hr)$, typically associated with long-haul road transport, aerodynamic drag accounts for nearly 40% of the delivered engine power (power at the crankshaft) (Van Raemdonck 2012), hence its reduction greatly helps both fuel consumption and emissions.

A breakdown of drag generation for a tractor with a semi-trailer (schematic in figure 1.1) shows that a little more than 30% of it comes from the underbody (Van Raemdonck 2012), on account of large-scale separation due to the cluttered geometry. The complexity associated with such flow makes the optimization of drag reduction technologies targeted at this region challenging. An important part of meeting this challenge is an increased understanding of the flow around the tandem wheels of a semi-trailer. The current project aims to investigate this region in an attempt to quantify the interaction between the rotating wheels and the associated drag reduction devices.

1.1 Early Research and Adoption

Comprehensive experimental investigations into many of the drag reduction devices seen today were performed as early as the 1950s (K. R. Cooper 2004). Wind tunnel tests at the University of Maryland

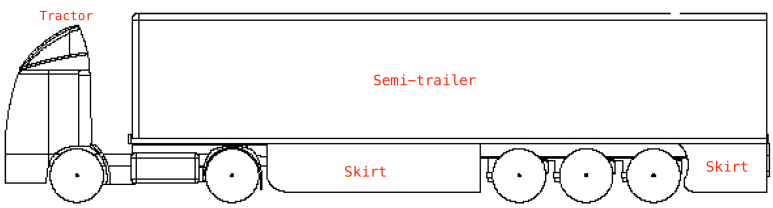

Figure 1.1: Schematic diagram of a tractor with a semi-trailer (Credit: R. Stephens and Babinsky 2016)

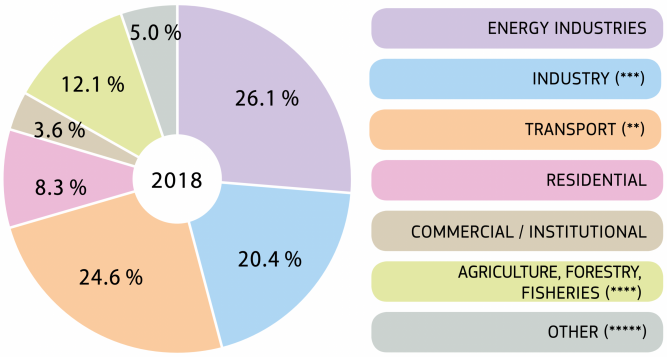

Figure 1.2: Green house gas emissions in EU by sector (Credit: European Commission, EU Transport in figures 2020 (Figures 2020))

during this period (Sherwood 1974a; Sherwood 1974b) provided an early look at the drag benefits of technologies like cab shaping, roof fairings, tractor-trailer gap seals, trailer side skirts, and rear boat tailing. Even so, the adoption of these by the trucking industry was slow, primarily due to low fuel prices in the years that followed. This changed with the oil crisis of the 1970s when increasing energy costs accelerated the adoption of some of these devices.

Amongst the drag reduction technologies that got adopted, most if not all applied to the tractor, with trailer-mounted devices remaining largely unused, a situation that persisted till about a decade ago. As late as 2010, the market penetration of trailer side-skirts, the most widely used trailer-mounted add-on device, was still below 5% in both North America and the EU (Rodríguez et al. 2017). Trailer-mounted devices make a weaker economic case; there are more trailers than tractors (currently 3:1 in North America (Sharpe, Delgado, and Lutsey 2014) and 1.4:1 in Europe (Hill et al. 2011; Meszler et al. 2018)) which diminishes the economic advantage of any add-on device. Moreover, trailers often are leased or client-owned, further disincentivizing spending on fuel savings (K. R. Cooper 2003).

1.2 Environmental Considerations and Impact of Regulations

In the last decade though, the deployment of trailer aerodynamic devices (and fuel-saving technologies in general) has been accelerated through policymaking in a bid to reduce emissions. Road-based freight transport is a significant contributor to net greenhouse gases (GHG) emissions. In 2018, considering GHG emissions by sector in the EU-27, Transport accounted for the second-highest emissions after Energy (figure 1.2) (Figures 2020). Within the transport sector, road transport accounted for a 71.8% share, of which 19% was attributable to heavy-duty trucks and busses. Therefore, heavy-duty vehicles accounted for nearly 5% of all GHG emissions in the EU. A similar situation can be extended to other industrialized economies, cementing the need for these policies.

The U.S. Environmental Protection Agency's SmartWay program, which includes a comprehensive repository of trailer-specific verification data on aerodynamic devices, has had a far-reaching impact on the acceptance of trailer-mounted aerodynamic devices. Another leading example is the California Air Re-

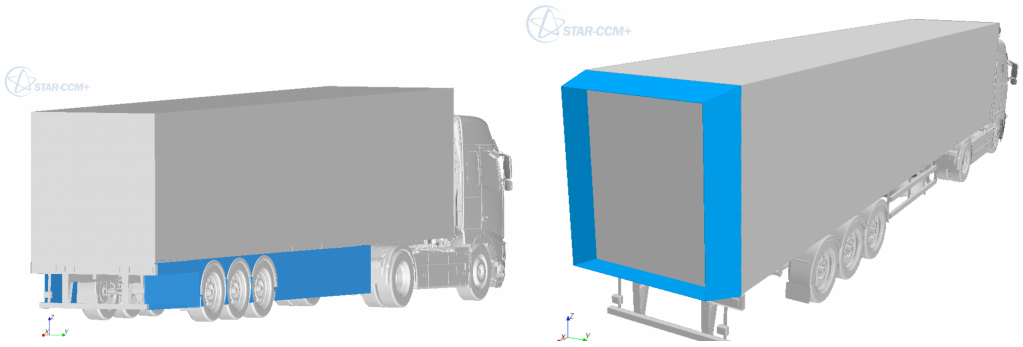

(a) Trailer Skirt (b) Boat tail

Figure 1.3: Trailer mounted aerodynamic devices (Credit: Hakansson and Lenngren 2010)

sources Board's (CARB) tractor-trailer GHG regulation. This leverages the SmartWay program and mandates aerodynamic and tire rolling resistance requirements for trucking fleets in California, in turn affecting nearly 30% of all tractor-trailers in the United States ((CARB) 2008). Building off the SmartWay program and California's fleet requirements is the second phase of regulatory standards in the United States that promote the efficiency attributes of trailers ((EPA) 2016). These recent changes set standards for trailers using a system of aerodynamic bins (I through VII, each higher bin signifying a higher reduction in drag), and mandate an increased deployment of trailers performing at the higher aerodynamic bins over time. The net effect of these legislations has been a significant ramp up in investments into trailer aerodynamics by trucking fleets. Among efficiency-conscious fleets in North America, adoption of trailer skirts has grown from near 0% in 2008 to over 80% in 2015 (Mihelic, Schaller, and Roeth 2016).

1.3 Prevalence of Trailer Side-Skirts and Case for Wheel Covers

While regulations continue to drive the adoption of all trailer-mounted aerodynamic devices, the highest uptake, by far, has been for trailer side skirts, making them of particular importance. A comparison between side skirts (figure 1.3a) and boat tails (figure 1.3b), two devices that can offer similar aerodynamic gains, shows that adoption for skirts is 40% as compared to 3% for boat tails when considering new trailer sales in North America (Mihelic, Schaller, and Roeth 2016). The reason is that underbody systems, such as skirts, are perceived to offer fewer operational challenges as they do not impede the free movement of freight while being as effective as trailer front/rear devices in saving fuel (3 to 7% fuel saving in real-world testing (Patten et al. 2012)).

Wheel covers as aerodynamic devices have a more modest impact. It is generally accepted that they offer less than 1% saving in fuel in real-world usage (Mihelic, Schaller, and Roeth 2016). In standardized SAE road tests (SAE J1321) for EPA SmartWay verification, a wheel cover of a certain design was shown to produce fuel savings of 1.3% (Wood 2012). They are however also proportionally easy and cheap to install, and are a recommended aerodynamic accessory, amongst others like vented mud flaps, by organizations such as the North American Council for Freight Efficiency.

1.4 Motivation for Design Cases

Despite offering fewer operational impediments, there are still practical considerations to covering the undercarriage of a trailer that greatly inform and often complicate skirt design. There is a considerable drag benefit (as much as 4% (Van Raemdonck 2012)) in covering the wheels entirely, when viewed from the side, using a long skirt as compared to terminating the skirt in front of the leading tandem wheel. However, legally mandated trailer width restrictions, resulting in clearance issues between the wheel and skirt, do not always allow this. Trailers with steered axles are also not compatible with this design. Moreover, long, continuous skirts also impede access to undercarriage components, making them less popular with fleets. Another factor that complicates design in this region is the sliding of trailer axles for weight balancing which creates a gap between the rear edge of the skirt and the leading wheel of the tandem. Therefore the region around the trailer tandem wheels is functionally constrained while being aerodynamically important, making its investigation significant.

Wheel covers also have to meet certain operational requirements that demand design alterations with aerodynamic implications. A key requirement is a view of and access to the wheels for inspection. Current designs accomplish this by either having physical openings or by the use of transparent panels with a quick-release mechanism. Another requirement is adequate airflow to the brakes for cooling. In general, the effect of aerodynamic devices such as skirts on brake temperatures has been shown to be small ($5°C - 9°C$ (Mihelic, Schaller, and Roeth 2016)), when compared to the operating temperature range ($170°C - 260°C$ (Fancher, Winkler, and Campbell 1992)). However, most suggestions on the adoption of wheel covers (such as the one by the National Research Council Canada (Patten et al. 2012)) do advise evaluation of their effect on the cooling of the brake assembly. The intersection of the above two operational requirements makes the aerodynamic evaluation of openings in wheel covers relevant.

1.5 Objective

The current project aims to experimentally investigate the region around rotating dual wheels in tandem as seen on semi-trailers used in long-haul transport. For this purpose, wind tunnel tests will be performed on model wheels which include the requisite geometrical features, shrouded by a bluff body, using stereoscopic particle image velocimetry.

With these tests, the objective is to study the effects of the following on the flowfield and drag:

- wheel rotation
- trailer side skirt and wheel cavity cover
- openings in the cover, particularly the size and radial placement

The motivation for the above stated objectives is elaborated upon in section 2.6, which summarizes the outcomes of the literature study (Chapter 2), conducted as part of this thesis.

Chapter 2

Literature Study

This chapter summarizes the findings of the literature survey conducted as part of the investigation into the influence of trailer side skirts and wheel cavity covers on the drag and flowfield of dual semi-trailer wheels. There is no particular, detailed body of literature that concentrates on the aerodynamics of trailer wheels and their interaction with surrounding geometry, such as trailer side skirts. Therefore this literature survey is structured around the individual components that were deemed relevant to the flowfield in this region of the trailer.

Section 2.1 details the aerodynamics of automotive wheels in isolation, covering the following:

- forces generated by rotating and stationary wheels in contact with the ground (sub-section 2.1.1)
- surface pressure around the circumference of the wheel and the impact of rotation on this pressure (sub-section 2.1.2)
- flowfield and critical structures in the near wake of a stationary and rotating wheel (sub-section 2.1.3)
- mechanism of formation of the vortical structures that define the flowfield around the wheel (sub-section 2.1.4)

The studies in this field are largely divided into 2 categories: those that examine wheels in isolation and those that investigate wheels housed in a wheel cavity of a vehicle. Of these two, the wheels of a semi-trailer, especially those used in North America, are better represented by isolated wheels, and hence the scope of the survey was limited to these.

Section 2.2 looks into the various methods of simulating the correct ground boundary conditions, as seen on the road, in the wind tunnel. Particular importance has been given to the effects of using a stationary ground plane instead of a moving one, and therefore breaking the contact of the wheel with the ground in order to allow for rotation.

Section 2.3 characterizes the flow in the underbody of a tractor with a semi-trailer, particularly with regard to the conditions upstream of the trailer wheels.

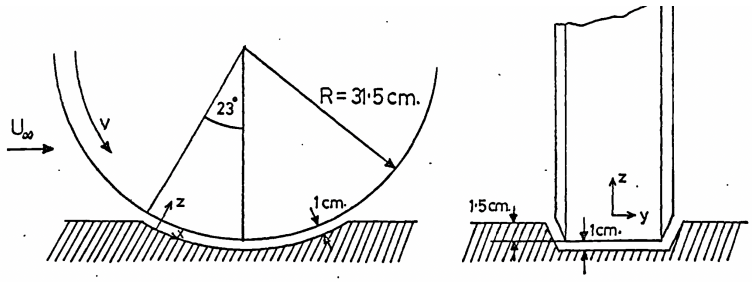

Figure 2.1: Experimental configuration for wheel rotation as used by Morelli 1969 (Credit: Fackrell 1974)

The impact of trailer side skirts on the drag of the tractor semi-trailer and underbody flowfield is presented in section 2.4. With regards to drag, specific attention was paid to studies that quantified the effect of skirt geometries in the vicinity of the trailer wheels, particularly in terms of coverage and offset of the skirt to the leading edge of the trailer wheels.

Finally, section 2.5 covers the influence of wheel covers on drag reduction. Sub-section 2.5.1 looks at the effect of covers on the drag, tread surface pressure, and rim surface pressure for an isolated wheel. Following this, sub-section 2.5.2 looks at various passenger car studies for an insight into the most relevant design parameters with regards to openings in the covers. Lastly, the effect of wheel covers on the drag of tractors with semi-trailers is included in sub-section 2.5.3.

2.1 Wheel Aerodynamics

2.1.1 Drag and Lift

The first investigation into the aerodynamics of automotive wheels was presented by (Morelli 1969), with the attempt to characterize the effects of geometry, yaw and ground clearance on the time-averaged lift and drag. A full sized racing car wheel was used with a diameter of $625\ mm$. The Reynolds number based on diameter ranged between 5×10^5 to 2×10^6. Due to the use of a stationary floor and to accommodate the use of a traditional wind tunnel force balance, the contact between the wheel and ground was broken, with the wheel made to protrude through the ground plane. The projection of the wheel into the slot was $15\ mm$, and a gap of $10\ mm$ remained between the wheel and the ground, resulting in a ground clearance to wheel diameter ratio of 0.016 (figure 2.1). A negative lift value was reported for the base case of a unyawed wheel with no fairing, attributed to the air flow accelerating in the region below the wheel. This was qualitatively confirmed by the results of (Stapleford and G. W. Carr 1970), who also reported a negative lift at a gap (g) to diameter (D) ratio of 0.016.

(Stapleford and G. W. Carr 1970) performed experiments on model wheels, rotating and stationary, with varying width - diameter ratios and ground clearances. An idealized Formula One car model was used, with the forces due to the wheels obtained by deducting those due to the body alone. The wheels were $162.5\ mm$ in diameter and the Reynolds number based on wheel diameter was 2×10^5. A static ground

plane was used primarily, with a limited study using a moving floor. For both the stationary and rotating cases (with stationary floor), the lift became increasingly negative as the ground clearance was reduced until a point, after which the trend reversed. For the stationary case, a positive lift was first recorded somewhere between $g/D = .17$ and $g/D = .08$. For the rotating wheel, positive lift was only reported for the case where the gap was sealed with strips of paper (reported as zero ground clearance). The drag coefficient, considering the range $0 \leq g/D \leq 0.1$, increased for the stationary case, and slightly decreased for the rotating case. Moreover, for all clearances except zero, the drag for the stationary case was lower. These results are discussed in further detail in section 2.2. A limited study with moving floor was also performed, but since the clearance gap could not sealed for this case, the general error in simulation remained. In fact, due to the significantly reduced ground boundary layer thickness, the error due to the gap was possibly exasperated.

(Cogotti 1983) performed a two-part study, part one of which was on isolated wheels. Both stationary and rotating wheels were tested using a fixed ground plane. The experimental setup comprised of two full-scale wheels on an axle rotated by a faired electric motor. The height of the assembly was made adjustable to vary the ground clearance. For the case of zero ground clearance, small foam rubber pads were inserted between the wheel and the ground. The motor was rotated at 1500 RPM giving a Reynolds number based on wheel diameter of 1.1×10^6. Lift and drag were measured using a force balance and found to be positive while being lower for the rotating case, in agreement qualitatively with the results of (Stapleford and G. W. Carr 1970).

The first experiments to correctly simulate a rotating wheel in contact with moving ground were conducted by Fackrell (Fackrell 1974; Fackrell and Harvey 1975; Fackrell and Harvey 1973). A 'Formula One' style model wheel was used, with a diameter of approximately $416\ mm$ and a wheel diameter based test Reynolds number of 5.3×10^5. Six different configurations were tested: two edge profiles (figure 2.2) and three widths (table 2.1). As opposed to previous studies which made use of a force balance, Fackrell used surface pressure integration to measure the lift and drag of the rotating wheel. The measurement system included a condenser microphone and the associated oscillator, which were placed on the axis of rotation. Pressure taps were mounted across the span of the wheel. The signal from the microphone was transmitted through slip rings into a reactance converter, whose output was proportional to the pressure. The results were in qualitative agreement with those of (Stapleford and G. W. Carr 1970).

Table 2.1 summarizes the drag and lift coefficients (based on frontal area), as well as the important geometric parameters, of the wheels tested by (Fackrell 1974), (Stapleford and G. W. Carr 1970), and (Morelli 1969). Also included are the numerical results of (McManus and Zhang 2005), for the 'A2' geometry of Fackrell. For the 'B2' geometry, both rotating and stationary cases were measured, and are included in the table. The values reported by (Fackrell 1974) have since been validated by various studies (Mears, Dominy, and Sims-Williams 2002; Mears, Crossland, and Dominy 2004; Dimitriou and Klussmann 2006), and are therefore a fair representation of the actual drag and lift of an isolated wheel in contact with the ground.

Looking at the lift, it can be seen that the lift for a wheel in contact with the ground is positive. The

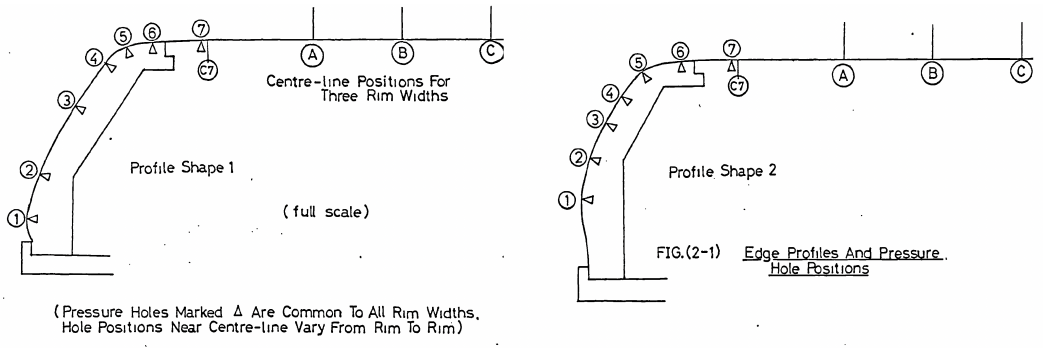

(a) Profile 1 (b) Profile 2

Figure 2.2: Side profile shapes of the wheels tested by Fackrell, ie. profile 1 and 2 for each of the widths A, B, and C (Credit: Fackrell 1974)

Author and Wheel Configuration	Wheel Rotation / Ground Simulation	Total Width (mm)	Tread Width (mm)	Aspect Ratio	C_D	C_L	Reynold's Number
Fackrell - **A1**	Rotating / Moving	208	108	0.50	0.52	0.28	5.3×10^5
Fackrell - **B1**	Rotating / Moving	274	170	0.66	0.63	0.40	5.3×10^5
Fackrell - **C1**	Rotating / Moving	337	233	0.81	0.70	0.43	5.3×10^5
Fackrell - **A2**	Rotating / Moving	191	108	0.46	0.51	0.28	5.3×10^5
McManus and Zhang - **A2**	Rotating / Moving	191	108	0.46	0.434	0.156	5.3×10^5
McManus and Zhang - **A2**	Stationary / Fixed	191	108	0.46	0.482	0.357	5.3×10^5
Fackrell - **B2**	Rotating / Moving	254	170	0.61	0.58	0.44	5.3×10^5
Fackrell - **B2**	Stationary / Fixed	254	170	0.61	0.77	0.76	5.3×10^5
Fackrell - **C2**	Rotating / Moving	316	233	0.76	0.70	0.43	5.3×10^5
Stapleford and Carr (M.I.R.A)	Rotating / Fixed	81.25	81.25	0.5	0.64	0.40	2×10^5
Morelli	Rotating / Fixed	243.75	175	0.39	0.45	-0.1	1.25×10^6

Table 2.1: Wheel configurations, drag and lift from (Fackrell 1974), (Stapleford and G. W. Carr 1970), (Morelli 1969) and (McManus and Zhang 2005)

coefficient of lift also increases with the increasing tread width of the tire, although the change in overall width seems to make little difference (comparing geometry '1' with '2'). The results reported by (Morelli 1969) show a negative lift on account of the gap left below the wheel. (Stapleford and G. W. Carr 1970) measured the forces for various ground clearances of the wheel, the result included here is for zero clearance and shows a positive lift (further discussion in section 2.2). The numerical study by (McManus and Zhang 2005), performed using the RANS approach, also shows the expected positive lift, however it underpredicts the lift considerably compared to the experimental result of the same wheel. For this study two turbulence models were used, the one-equation Spalart - Allmaras (SA) model and the two-equation Realizable $k - \epsilon$ (RKE) model. The result mentioned in the table is for the Realizable $k - \epsilon$ model with the fine grid. Comparing the stationary and rotating cases of the 'B2' wheel, rotation causes a reduction in lift. Differences between rotating and stationary wheel in terms of surface pressure, near wake velocity, and vortical structures are discussed in detail in upcoming sub-sections.

Moving on to the drag values, and looking at the results of Fackrell, similarly to the lift coefficient, the drag coefficient increases with an increase in the tread width although the absolute width seems to have little effect on the drag (except the 'B' geometry, but this was inferred by Fackrell as a consequence of the lower angular resolution of pressure measurement for this geometry rather than a difference in actual flow physics). Comparing the drag coefficients of stationary and rotating cases, it can be seen that just like the lift, rotation also suppresses the drag of a wheel in contact with the ground.

2.1.2 Surface Pressure

As detailed previously, the first measurements of surface pressure for a rotating wheel in contact with a moving ground were made by Fackrell (Fackrell 1974). Similar to Fackrell, surface pressure measurements were made by Mears et al. (Mears, Dominy, and Sims-Williams 2002; Mears, Crossland, and Dominy 2004), on both stationary and rotating wheels, utilizing a radio telemetry system to measure surface pressure. A front go-kart wheel was used, allowing for deformation at the contact patch, although the inflation pressure used in this study was high enough to render the wheel rigid. The tire was mounted on a multi-element wheel rim, allowing for easy installation of the telemetry system and possible variations of the wheel centers (although none were tested). The wheel had a diameter of $247\ mm$ and an aspect ratio of 0.53; the Reynolds number based on wheel diameter being 2.5×10^5. The surface pressure results were in agreement with those reported by Fackrell, with the exception of the post contact patch suction peak, which was observed in this study but only theoretically predicted by Fackrell.

Figure 2.3 shows the pressure measured along the centerline of various stationary and rotating wheels from the experiments of (Fackrell 1974) and (Mears, Dominy, and Sims-Williams 2002). From the results presented by Fackrell, pressure distributions for both the 'A2' and 'B2' configurations are plotted. The 'A2' configuration was tested by Fackrell at a higher angular resolution $(0.5°)$ as compared to the 'B2' configuration $(5°)$, however, the differences are relatively small. On the other hand, the 'B2' configuration was the only configuration to be tested for both the stationary and rotating cases and is therefore

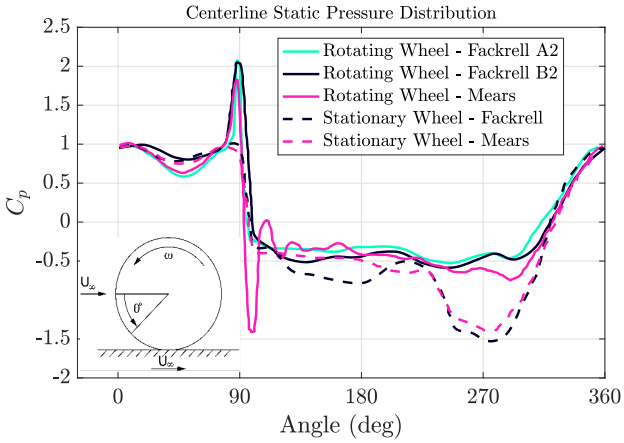

Figure 2.3: Centerline Static Pressure Distribution (after Fackrell 1974 and Mears, Dominy, and Sims-Williams 2002)

used to highlight the effects of rotation.

For the rotating wheel, starting at $0°$ and moving anti-clockwise along the wheel, the first interesting feature is the pressure peak in front of the contact patch, with a pressure coefficient in excess of 2. This is due to the viscous action on the flow by the moving boundaries - the rotation of the wheel and the moving ground plane. The resulting outward flow from near the front of the contact patch is termed the 'jetting' phenomenon (Fackrell 1974; Axon 1999). Just as there is a positive pressure peak due to converging boundaries, Fackrell predicted a negative peak due to diverging boundaries downstream of the contact patch but did not observe it in his results. This was attributed to the lifting of the moving floor in the low-pressure region behind the wheel. The results of (Mears, Dominy, and Sims-Williams 2002; Mears, Crossland, and Dominy 2004), however, as seen in figure 2.3, do show this negative peak. This difference is significant from the point of view of net lift. Looking at the same angular region for a stationary wheel, it is seen that in the absence of converging boundaries, the jetting phenomenon is absent and the pressure coefficient near the contact patch is close to unity.

Moving to the top of the wheel ($\theta = 270°$), a pressure drop is observed as the flow accelerates over the curvature of the wheel. The suction however is much stronger for the stationary wheel when compared to the rotating wheel, more than compensating for the pressure peak near the contact patch seen for the rotating wheel and resulting in a higher net lift for the stationary wheel. For the rotating wheel, the pressure distribution shows an adverse pressure gradient from ($\theta = 300°$ to $280°$), with a reversal of slope after this. Based on this, as well results from flow visualization and pitot tube traverses of the boundary layer in this region, Fackrell concluded $\theta = 280°$ to be the point of separation. By contrast, the separation point for the stationary wheel is around $\theta = 210°$, $70°$ later than the rotating wheel (Fackrell 1974; Axon 1999). Looking at the base of the wheel, the pressure is lower for the stationary wheel, resulting in a higher drag when compared to the rotating wheel. This is despite a later separation of flow for the stationary wheel, which would usually mean a higher base pressure. This led Fackrell to conclude that the action of rotation, in itself, was significant on the pressure in the separated region.

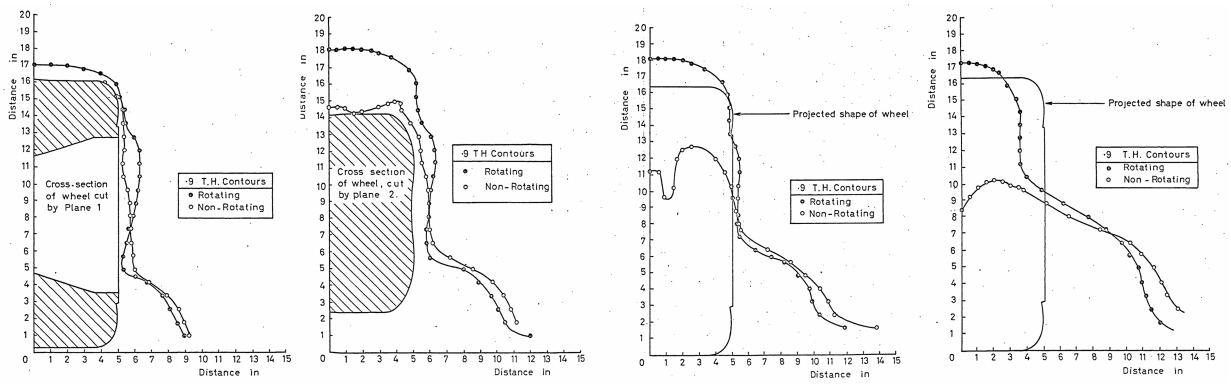

(a) Plane 1 - 0.10D (b) Plane 2 - 0.35D (c) Plane 3 - 0.51D (d) Plane 4 - 0.86D

Figure 2.4: Total pressure contours in wake of stationary and rotating wheel (Credit: Fackrell 1974)

2.1.3 Near Wake

The earliest work on the downstream flowfield of an automotive wheel was performed by (Fackrell 1974), presenting the total pressure in the wake using a Kiel tube insensitive to inflow angles of $\pm 35°$, on four crossflow planes positioned at 0.10, 0.35, 0.51, and 0.86 times the wheel diameter from the axis of rotation. The size of the wake, comparing rotating and stationary wheels, was presented as contours lines of $C_p = 0.9$ for only one-half of the wheel, opposite to the side with the support structure (figure 2.4). An 'L' shaped wake was seen (or an inverted 'T' shape if the result is extended symmetrically to the other half), with the top portion following the wheel outline closely and the bottom showing a wider region of disturbed flow. At the first measurement plane, the contour for the rotating case already extended above the top surface of the wheel, suggesting separation before this point. The flow for the stationary case remained attached and as a result, the wake was shorter. Concerning the lower part of the wake, the stationary case had a wider separated region. This was surprising as the expectation was for the stronger contact patch jet of the rotating wheel to cause a larger disturbance. Fackrell postulated that the larger lobe for the stationary case could be attributed to the boundary layer separating ahead of the contact patch and rolling up to form a horseshoe vortex.

Further work was presented on wheel wake structures by (Bearman et al. 1988), who used one of Fackrell's wheels and made measurements using a 9-hole probe 2.5 wheel diameters downstream of the axis of rotation. Total pressure, static pressure, and flow direction were measured, using which the local velocity components and streamwise vorticity were computed. The Reynolds number for this test was slightly higher than Fackrell's at 5.5×10^5. The vorticity data showed the presence of a counter-rotating vortex pair (CVP) in the wake of the wheel. The CVP behind the stationary wheel showed higher intensity and was present closer to the ground compared to the rotating case. Figure 2.5b shows the schematic representation of the vortex structure in the near wake based on the velocity data of Bearman. This contradicts the model proposed earlier by (Cogotti 1983), based on theoretical considerations (figure 2.5a). Another such theoretical model was proposed by (Mercker and Berneburg 1992), which includes the lower CVP as witnessed in the results of (Bearman et al. 1988). However, the vortex pairs near the top

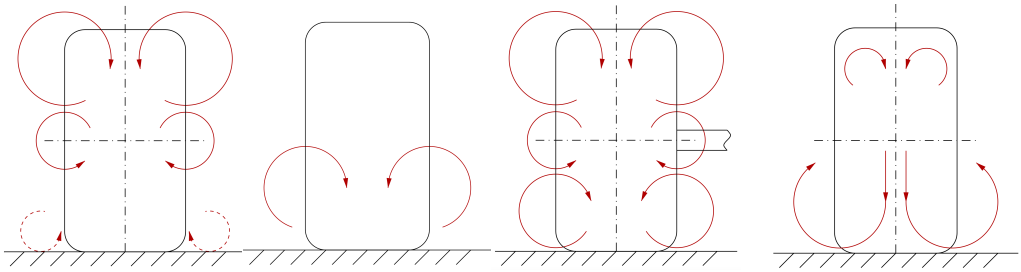

(a) Cogotti 1983 (b) Bearman et al. 1988 (c) Mercker and Berneburg 1992 (d) Saddington, R. D. Knowles, and K. Knowles 2007 $x/D < 1$

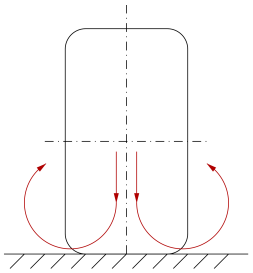

(e) Saddington, R. D. Knowles, and K. Knowles 2007 $x/D \geq 1$

Figure 2.5: Models for the trailing vortex system of a rotating wheel in ground contact (Credit: Saddington, R. D. Knowles, and K. Knowles 2007)

and at the hub as shown in figure 2.5c, have not been confirmed by experimental or numerical results. As an improvement of these models, (Saddington, R. D. Knowles, and K. Knowles 2007) proposed a new model based on experimental data (figure 2.5d and 2.5e). The investigation by (Saddington, R. D. Knowles, and K. Knowles 2007) used Laser Doppler Anemometry (LDA) to study the wake structure of a rotating Formula One wheel. A 1:2 scale model was used with a test Reynolds number, based on wheel diameter, of 6.8×10^5. Measurements were made at 3 streamwise locations, 0.6, 0.75, and 1 diameter downstream of the axis of rotation. The derived model consisted of two CVPs, one at ground level and another near the top of the wheel. The top vortex pair was proposed to exist only within one diameter of the wheel's axis, after which it merged with the ground vortex pair.

Figure 2.6 shows the non-dimensionalized streamwise velocity in the wake of an isolated rotating wheel as measured by (Saddington, R. D. Knowles, and K. Knowles 2007). At a plane 0.6 diameters downstream of the wheel axis (figure 2.6a), the upper region of the wake was seen to have approximately the same dimensions as the projected wheel profile. In the lower part, two lobes of lower velocity flow were seen on either side of the wheel. The authors proposed that these ground lobes were a result of the freestream getting deflected by the sideways jet created ahead of the contact patch due to converging boundaries. The asymmetry in the contours was attributed to the support structure on one of the sides. This inverted 'T' shape of the wake agrees with the results presented earlier by (Fackrell 1974), (Nigbur 1999), (Wäschle et al. 2004), and others.

Similarly to (Saddington, R. D. Knowles, and K. Knowles 2007), (Wäschle et al. 2004) also used Laser

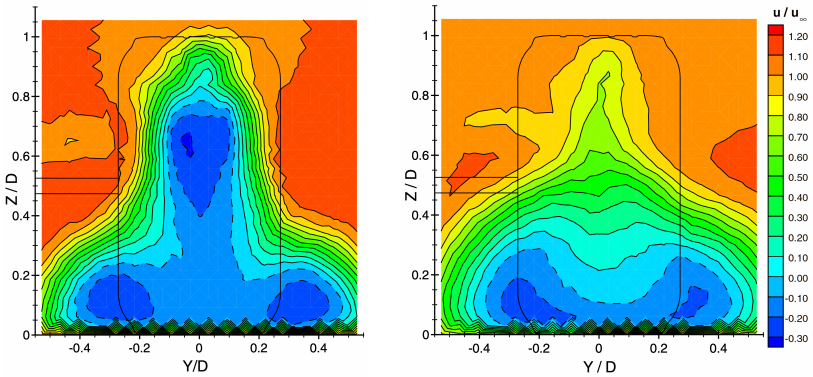

(a) $x/D = 0.6$ (b) $x/D = 1$

Figure 2.6: Contours of mean streamwise velocity (after Saddington, R. D. Knowles, and K. Knowles 2007), meausred using LDA on a rotating wheel in contact with moving ground. Reynolds number based on wheel diameter of 6.8×10^5

Doppler Anemometry (LDA) to measure the velocity field in the wake of an isolated Formula One wheel, both rotating and stationary. A 1:3 scale model of the front wheel was used, $215.8\ mm$ in diameter and with $80\ mm$ tread width. All tests were conducted at $45\ m/s$ resulting in a wheel diameter based Reynolds number of 5.37×10^5. Lift and drag were also measured using a force balance connected to both the support sting and the moving mini-belt used for wheel rotation. Using these results to compare the wake of a rotating wheel with a stationary one, it is seen that the inverted 'T' shape discussed above is less pronounced. Figure 2.7 compares the near wake of a stationary and a rotating wheel at 2 downstream locations. Two major differences can be seen. The first is that the wake of the rotating wheel is taller, as a result of earlier separation on the top surface when compared to a stationary wheel. The second difference is in the pair of counter-rotating vortices on the ground, which are further apart and stronger for the stationary wheel. Both of these trends are seen further downstream as well, where the wake of the stationary wheel remains both wider and shorter than the rotating wheel. The possible reasons for this are discussed in sub-section 2.1.4.

2.1.4 Vortex Structures

The flow behind an isolated wheel is dominated by the counter-rotating vortex pair (CVP) near the ground. According to (Axerio and Laccarino 2012), the ground vortex pair originates near the front of the contact patch due to the sideward directed flow caused by the contracting volume between the wheel and the ground. This flow then separates at the tire shoulders and forms a vortex pair. (Wäschle 2007) termed this as the 'wheel squash' vortex (marked ③ in figure 2.8) and saw its presence for both stationary and rotating wheels.

The ground vortex pair develops further at the rear of the wheel and is stronger for a stationary wheel than for a rotating wheel. (Wäschle 2007) termed the dominant vortex structure in the wake as the 'wake horseshoe vortex', marked ① in figure 2.8. For a stationary wheel, it is generally well agreed that the

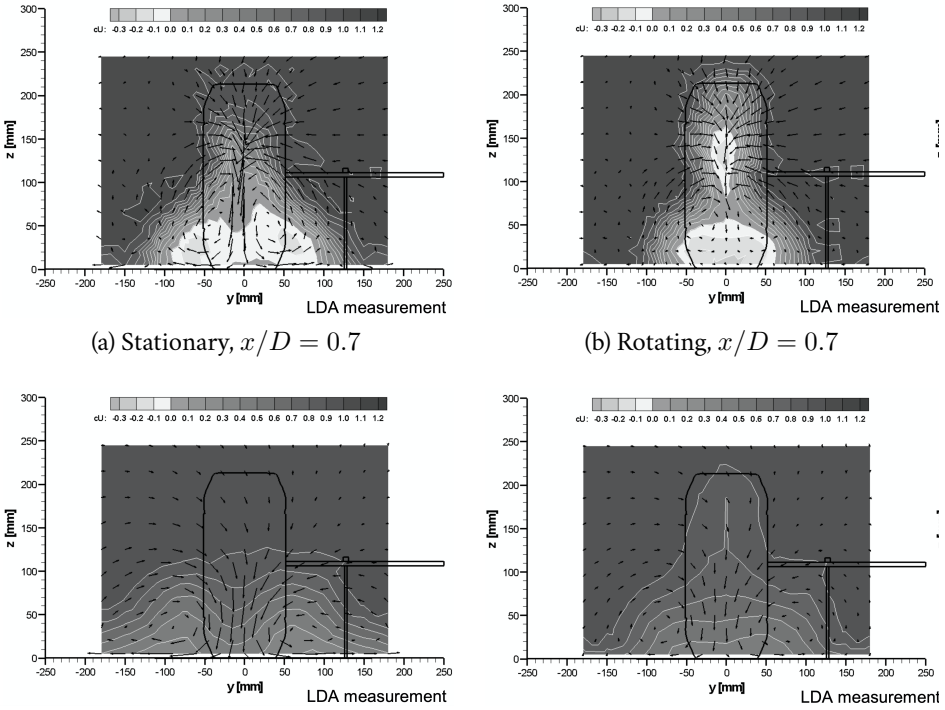

(a) Stationary, $x/D = 0.7$ (b) Rotating, $x/D = 0.7$

(c) Stationary, $x/D = 1.9$ (d) Rotating, $x/D = 1.9$

Figure 2.7: Velocity field behind rotating and stationary wheels (after Wäschle et al. 2004)

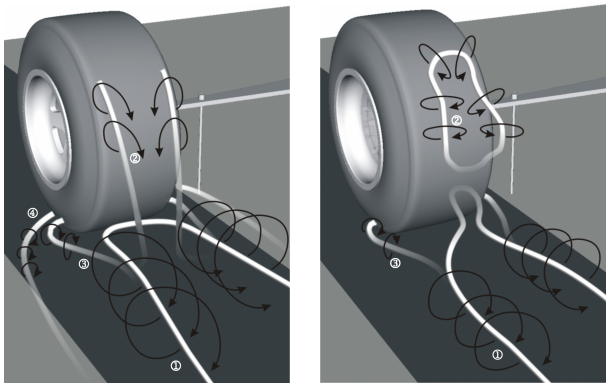

(a) Stationary Wheel (b) Rotating Wheel

Figure 2.8: Vortex Structures for Stationary and Rotating Wheels (after Wäschle 2007)

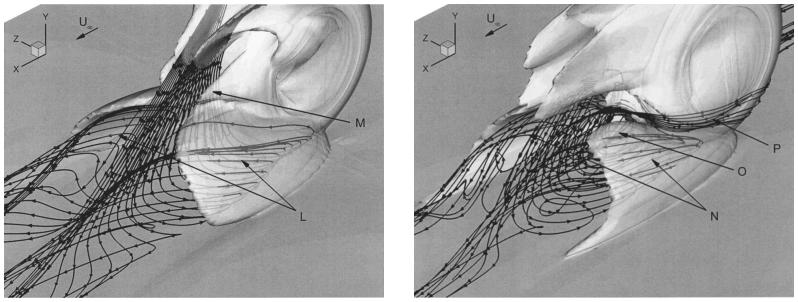

(a) Stationary Wheel (b) Rotating Wheel

Figure 2.9: Lower near wake (Credit: McManus and Zhang 2005)

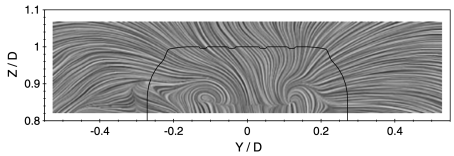

Figure 2.10: Isolated rotating wheel - top vortices at $x/D = 0.4$ (after Saddington, R. D. Knowles, and K. Knowles 2007)

vortex pair is created by the flow down the rear face of the wheel impinging on the ground and rolling up (figure 2.9a). The flow down the rear face in turn originates from the high momentum flow on the sides of the wheel getting entrained into the flow over the central upper and rear surfaces, energizing it and keeping it attached (McManus and Zhang 2005). For a rotating wheel, (Axerio and Laccarino 2012) mention of a similar mechanism, perhaps to a lesser extent. However, (McManus and Zhang 2005) explain the vortex pair for rotating wheels simply as areas of recirculation in the lower wake enhanced by the entrainment of flow from the sides of the wheel (figure 2.9b). Besides the 'wheel squash' vortex, (Wäschle 2007) observed the presence of a very weak stagnation horseshoe vortex (marked ④) for the stationary wheel. The presence of a horseshoe matrix in the front of the contact patch was postulated by (Fackrell 1974) to explain the larger lower wake region beside the stationary wheel when compared to the rotating wheel, but not observed experimentally. Since then, certain numerical investigations (eg. by (Wäschle 2007)) have shown the presence of this vortex, whereas others like (McManus and Zhang 2005) did not observe it and gave alternate explanations for the greater lateral spread of the separation region of stationary wheels. They argued that the cause for the difference was in the oncoming flow conditions, that the slower flow resulting from a thicker boundary layer for the stationary wheel and floor combination deflected the separation region to a lesser extent, allowing it to grow larger.

Experiments by (Saddington, R. D. Knowles, and K. Knowles 2007) and (Axerio and Laccarino 2012) have also shown the presence of a top vortex pair in rotating wheels, not shown in results of (Wäschle 2007) (figure 2.8). Figure 2.10 shows these upper vortices at a plane 0.4 diameter downstream of the wheel axis. Beyond this plane, these vortices were observed to convect downwards and merge with the lower vortex pair.

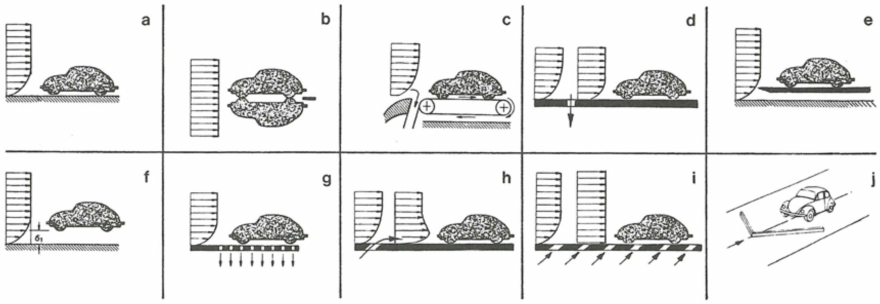

Figure 2.11: Various options for reproducing the road in a wind tunnel (Credit: Hucho 1998)

2.2 Ground Simulation

Apart from the earliest studies by (Morelli 1969), (Stapleford and G. W. Carr 1970), and (Cogotti 1983), most investigations into the aerodynamics of automotive wheels have been performed using the correct boundary conditions at the ground. This correct representation of a rolling wheel in the wind tunnel is to move the floor at the same velocity as the air and to have the wheel contact the ground and rotate at a circumferential velocity that equals the floor. This practice however does not transfer readily to testing of entire vehicles, either full-scale or scaled-down, due to practical limitations such as a sufficiently sized moving ground plane, force measurement instrumentation, etc. Therefore, simpler techniques have been developed to represent the road. Figure 2.11 shows the most common options of representing a road in the wind tunnel.

The simplest setup is to place the vehicle on the stationary floor of the wind tunnel, as shown in figure 2.11(a). However, this places the vehicle in the thick boundary layer of the wind tunnel floor. Figure 2.11(f) suggests lifting the vehicle off the floor to evade the boundary layer, however, this would change the flowfield around the vehicle drastically. The mirror image technique (figure 2.11(b)) is effective for inviscid flows, but for viscous flows, the wakes of the two bodies tend to interact, resulting in an incorrect flowfield. Figure 2.11(e) represents the use of a ground board that is elevated from the wind tunnel flow, thus resulting in a thinner boundary layer at the model. This method is quite effective as a low-cost option for ground simulation. The setups in figure (d), (g), (h), and (i) further improve on this method by adding either boundary layer suction or tangential blowing to the setup. Setups (d) and (h) show suction and blowing respectively, upstream of the model, whereas (g) and (i) show distributed suction and blowing over the length of the model respectively.

Various studies have compared the use of low-level suction or blowing as an alternative to moving ground plane. (G. Carr 1988) tested various representations of road cars and race cars with a moving ground plane and distributed suction. For one of these, a 1:6 scale fast-back model, drag and lift were also reported with boundary layer suction upstream of the model. Using the moving ground plane as a baseline, the distributed suction system resulted in around a 5% increase in drag whereas upstream suction resulted in about a 4% decrease in drag. These differences can be considered relatively small, especially considering the low ground clearance (12.5 mm) and smooth underbody used. According to (K. R. Cooper 1993), a stationary floor with a thinned boundary layer is sufficient for automotive

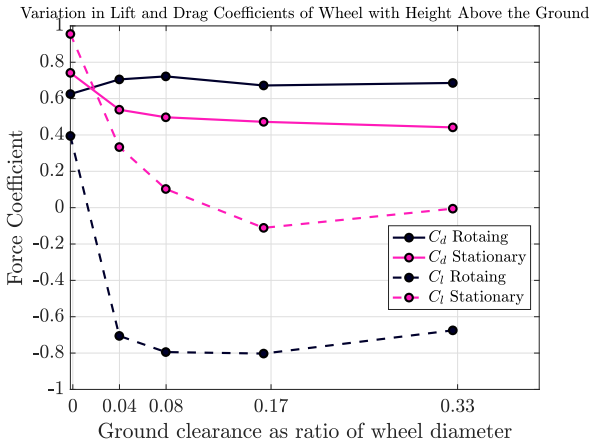

Figure 2.12: Variation in Lift and Drag Coefficients of Wheel with Height Above the Ground (plotted based on data from Stapleford and G. W. Carr 1970)

and commercial vehicle testing, especially if the underbody clearances are large and the underbodies are rough. Moreover, it is suggested to provide wheel rotation to further improve drag accuracy (K. R. Cooper 1993; Hackett et al. 1987).

For setups that do not include a moving ground plane, a commonly used workaround to allow for wheel rotation is to leave a certain clearance between the wheel and the ground. From the point of view of wheel aerodynamics, the shortcomings of this incomplete simulation are quite clear. Potential theory suggests that with a small gap between the wheel and the ground, a Venturi effect is created, accelerating the air through the gap and creating a negative lift force. At very small gaps, viscous effects dictate the flow, causing separation before the trailing edge of the body in question, drastically reducing this effect and essentially reversing the direction of the lift force. This trend can be seen in the results reported in the work of (Stapleford and G. W. Carr 1970), and plotted in figure 2.12. The results in this figure are for rotating wheels with stationary ground, including the zero ground clearance case, in which the gap was sealed.

Similar to (Stapleford and G. W. Carr 1970), the results for the lift and drag of full-size automotive wheels presented by (Morelli 1969) also show the same negative lift coefficients on account of the 10mm gap left between the wheel and the floor to allow for balance measurements. Morelli argued on basis of the normal boundary layer assumption that this suction effect would be small and correctable for small values of the clearance to wheel radius ratios. However, as detailed by (Fackrell 1974), based on the solution of flow between parallel plates in (Batchelor 2000), the correction given by Morelli ignores the effect of the streamwise pressure gradient across the wheel contact line. Because of the interdependency between the volume flux and this streamwise pressure gradient, any correction for the erroneous negative lift force is difficult to implement.

However, as can be seen in figure 2.12, the variability of drag with ground clearance, for both the stationary and rotating wheels, is much lower than the variation in the lift. This, in general, is positive for the testing of passenger and commercial vehicles where the measurement of drag is of primary impor-

tance. When studying the overall drag of vehicles, even when the emphasis is on changes in the wheel assembly, a good correlation has been seen between the correct and limited ground simulations. Investigations by (Arora and Lyu 2016) compared the drag coefficient deltas between configuration changes for a full-scale Volvo aerodynamics concept vehicle utilizing a moving ground plane and a 1:5 scale model with its wheels off the ground by 2mm and reported an agreement between the setups. The same scale model setup was also used by (Bolzon, Sebben, and Broniewicz 2019), to study variations in wheel rim geometry and wheel thread pattern, and agreement was reported with studies using moving ground plane and numerical simulations.

In the context of tractors and semi-trailers, the study detailed in (Leuschen 2013) looked at the effects of ground simulation on the force and pressure data of a half-scale model of a tractor with a semi-trailer with rotating tractor wheels. The tests were conducted at the 9-meter wind tunnel of the National Research Council (NRC) of Canada, at full-scale Reynolds number (not reported but expected to be between 5×10^6 and 7×10^6). The ground simulation at this tunnel was reported to include a $1\ m\times5.7\ m$ center belt and 4 wheel rollers. However, because the wheel rollers were spaced for passenger vehicles, the tractor wheels were lifted off the ground and rotated using internal motors. The trailer wheels were not rotated. In the results discussed below, "full ground simulation" refers to the use of the upstream boundary layer suction, rolling center belt, and rolling wheels, whereas "fixed floor" refers to the use of boundary layer suction only.

Figure 2.13a shows the effect of ground simulation on drag for the baseline vehicle. As can be seen, the movement of the center belt caused the most change in drag, regardless of the yaw angle. By comparison, the effect of rotating wheels was small. In general, the drag for cases with a moving belt was higher, attributable to the higher underbody velocity resulting from the thinner boundary layer.

Figure 2.13b shows the effect of ground simulation on the performance of side-skirts. As can be seen, skirts resulted in a reduction in drag regardless of the method of ground simulation. The effectiveness of the skirts can also be seen to increase with yaw angle. Also, full ground simulation resulted in a higher drag compared to a fixed floor, for both the baseline case as well as with the skirts fitted, as can be expected based on the results discussed above. Perhaps most importantly, the deltas between the drag of skirted and non-skirted trailers remain very similar across yaw angles notwithstanding the method of ground simulation. This suggests that as far as judging the performance of skirts is concerned, using a setup with a fixed floor and wheels (but with upstream boundary layer suction) would yield results as good as a moving belt with rotating wheels.

In conclusion, as far as ground simulation for testing of commercial vehicles is concerned, an elevated ground plane with thinned boundary layer, preferably with distributed suction/blowing, is quite suitable. Moreover, the addition of rotating wheels is useful, especially if the properties of rims or tires are of interest. For this purpose, either rollers fitted below the ground can be used or a gap can be left between the wheel and the ground. This gap should ideally be kept around 0.5% of the wheel diameter (K.R. Cooper 1984), though, in practice, gaps between 1 to 2 % are more common and have still shown good results.

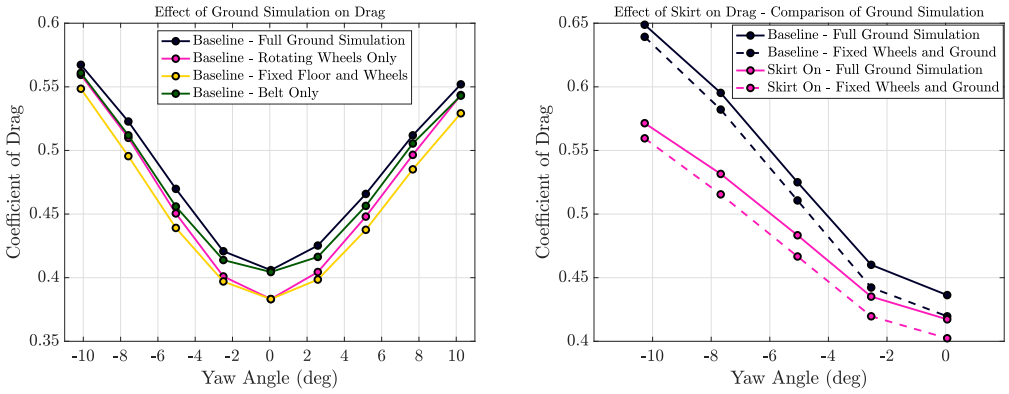

(a) Effect of Ground Simulation on Drag

(b) Effect of Skirt on Drag - Comparison of Ground Simulation

Figure 2.13: Effect of Ground Simulation on Drag (after Leuschen 2013)

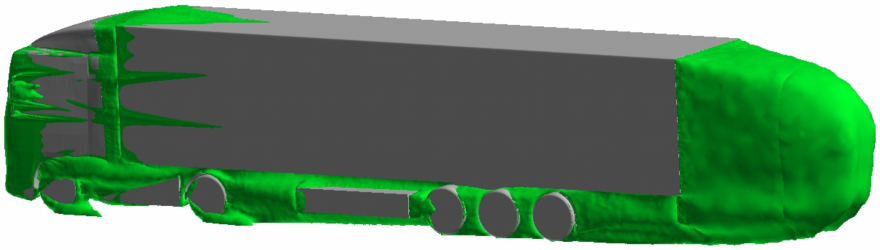

Figure 2.14: Iso-surfaces of $P_T - P_\infty = 0$. (Credit: Van Raemdonck 2006)

2.3 Tractor-trailer Underbody Flow

The underside of a tractor with a semi-trailer accounts for about 32% of its total drag (Van Raemdonck 2006) and is characterized by highly turbulent and separated flow, resulting from a plethora of bluff geometries like support legs, storage boxes, reefer tanks, spare tires, suspension, axles, and wheels. Figure 2.14 indicates the areas with recirculating flow as the iso-surface of a zero pressure difference between the local total pressure and the ambient pressure. It shows the underside as one of three regions with highly separated flow, others being the tractor-trailer gap and the base of the trailer.

Looking at the streamlines in the underbody region, as illustrated in figure 2.15, it is seen that the flow is largely attached as it traverses the rounded front bumper and underside of the tractor, although it must be considered that this model did not include the complex geometry of the engine compartment. Further on, large-scale separation is seen behind the rear tractor axle and in the region surrounding the trailer tandem axles.

Further insight into the flowfield in the undercarriage is gained through the experiments of (R. G. Stephens, Stevens, and Babinsky 2016), wherein a 1/10 scale model of tractor-semi-trailer was tested in a water towing tank to correctly replicate the ground boundary condition and wheel rotation. The measurement system included a planar PIV setup and velocity data was presented on 4 horizontal planes in the underbody as seen in figure 2.16, where $'z'$ is the vertical coordinate and $'b'$ is the width of the

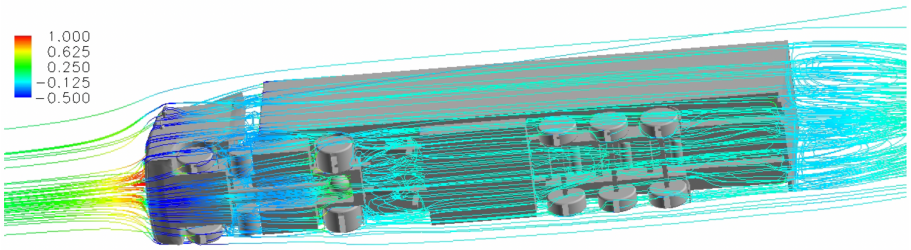

Figure 2.15: Streamlines around a tractor with semi-trailer. (Credit: Van Raemdonck 2006)

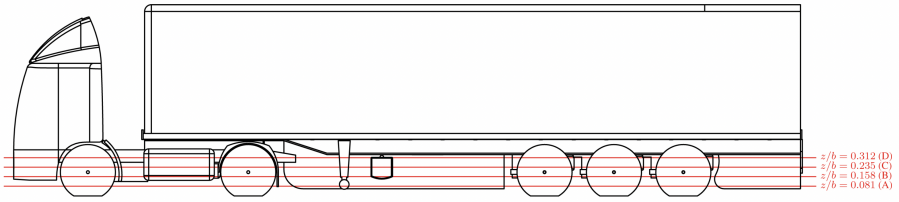

Figure 2.16: Location of measurement planes. (Credit: R. G. Stephens, Stevens, and Babinsky 2016)

model, equaling 260 mm. Results from 2 of the 4 planes are discussed here, namely plane 'B' and plane 'C', which are located vertically below and above the wheel centerline respectively. Flow features are mentioned in the order of their streamwise appearance.

At the front end of the vehicle, looking at velocity contours for plane 'B' (figure 2.17a), besides the stagnation at the front of the tractor, a recirculation region can be seen past the rounded front edge of the tractor, approximately between $x/b = 0$ and $x/b = 0.5$. Beyond $x/b = 0.5$, a region of separated flow is seen, originating from the front wheels of the tractor, and reaching about half the vehicle width. On plane 'C' (figure 2.18a), the stagnation is more pronounced and the separation at the corners is not seen, perhaps because the influence of the bottom edge is lesser. The separation near the front wheel is also less noticeable.

Moving to the region between the rear tractor wheels and the front trailer wheels ($x/b = 2$ to $x/b = 4$), it is seen that the tractor rear wheels, as well as the components such as the landing gear and fuel tank, are sources of large-scale separation. This area is of particular importance as it forms the upstream region for the trailer wheels. Velocity contours on plane 'B' (figure 2.17a) show the wake behind the tractor rear wheels as well the relatively higher momentum flow between the wheels. From the streamlines (figure 2.17b), it seems this higher momentum flow gets entrained by the wake behind the tractor wheels and moves laterally outwards, impinging on the front trailer wheel. The fuel tank has little effect at this height. On plane 'C' (figure 2.18a), the wake behind the fuel tank and the landing gear is clearly visible. Moreover, looking at the streamlines on plane 'C' (figure 2.18b), there is an inflow from the outside into the underbody, as the high-speed flow moving down the side of the vehicle gets entrained into the lower momentum flow in the underbody. This high momentum flow then impinges upon the axle and wheels and represents a source of drag.

The above discussion shows that at a yaw angle of $0°$, there is already a tendency for the flow beside

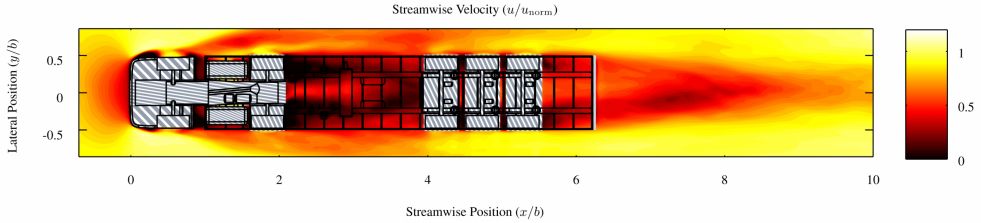

(a) Contours of normalised velocity

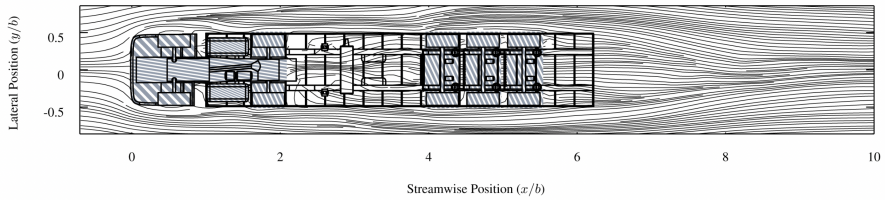

(b) Streamlines

Figure 2.17: Plane 'B', $z/b = 0.158$ (Credit: R. G. Stephens, Stevens, and Babinsky 2016)

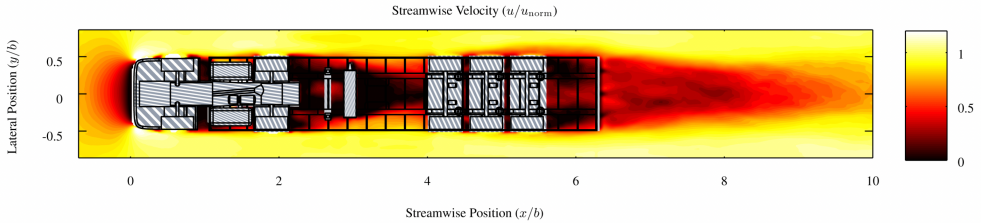

(a) Contours of normalised velocity

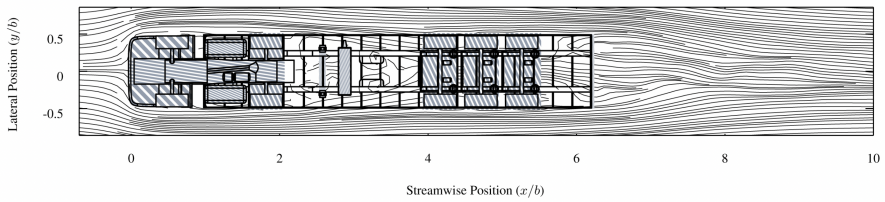

(b) Streamlines

Figure 2.18: Plane 'C', $z/b = 0.235$ (Credit: R. G. Stephens, Stevens, and Babinsky 2016)

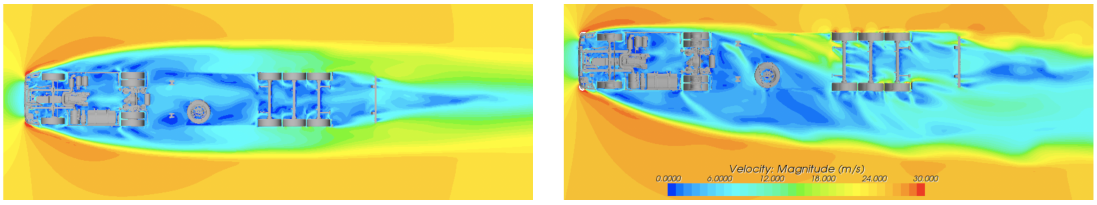

(a) $Yaw = 0°$ (b) $Yaw = 5°$

Figure 2.19: Velocity contour in the underbody (Credit: Hakansson and Lenngren 2010)

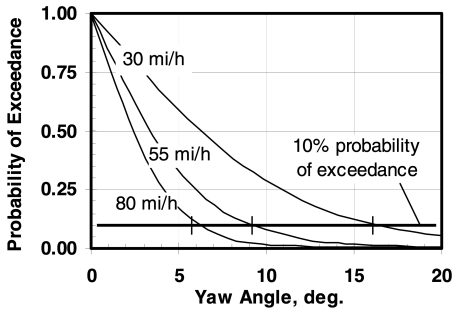

Figure 2.20: Probability of exceeding a given yaw angle (Credit: K. R. Cooper 2003)

the trailer to move inward and impinge upon the trailer wheels. This effect increases manyfold for larger values of yaw. In a comparison between the underbody flow at $0°$ and $5°$ of yaw, (Hakansson and Lenngren 2010) show the significant increase of inflow into the undercarriage of the trailer and corresponding extended wake structure on the leeward side (figure 2.19).

2.4 Trailer Side-Skirts: Impact on Drag and Flowfield

Trailer side skirts are essentially just vertical plates, mounted longitudinally along the side of a trailer to extend the sidewalls closer to the ground. The idea behind this to prevent the high momentum flow from entering the underbody and interacting with the various disturbances present underneath. Because the inflow is significantly greater at larger yaw angles, trailer side skirts become very effective drag reduction devices at these angles. This characteristic is important because trucks often function in nonzero yaw angles due to natural wind. Figure 2.20 shows the probability of exceeding a given yaw angle as a result of natural wind, for several road speeds, based on hourly-mean wind statistics. Following the $55\ mi/hr$ curve $(88.5\ km/hr)$, it can be seen that yaw angles up to $5°$ are quite likely, with the probability of exceeding $5°$ being nearly 35%.

2.4.1 Impact of Side Skirts on Drag

Many studies have been conducted to investigate the effect of trailer skirts on the drag of a tractor and semi-trailer combination. One of the earliest was an experimental study conducted at the University of Maryland on a cab over engine (COE) tractor with a box trailer (Sherwood 1974a). The model used

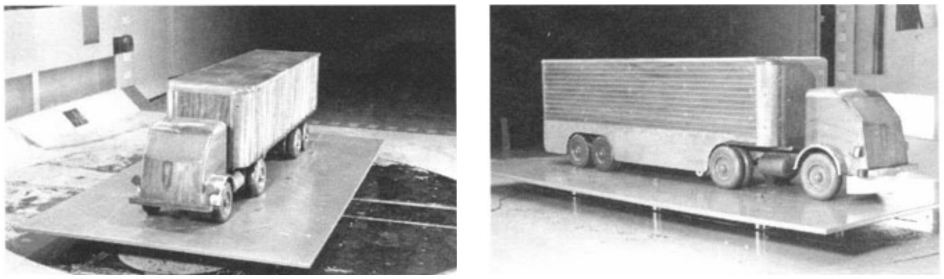

(a) Reference model (b) Model with trailer side-skirt

Figure 2.21: Wind tunnel models. (Credit: K. R. Cooper 2004)

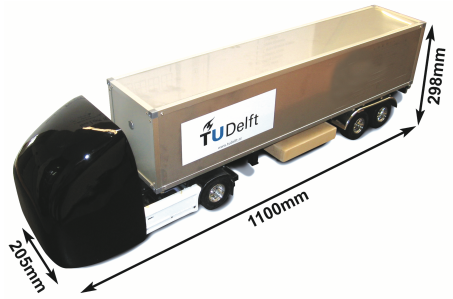

Figure 2.22: Wind tunnel model (Credit: Van Raemdonck 2012)

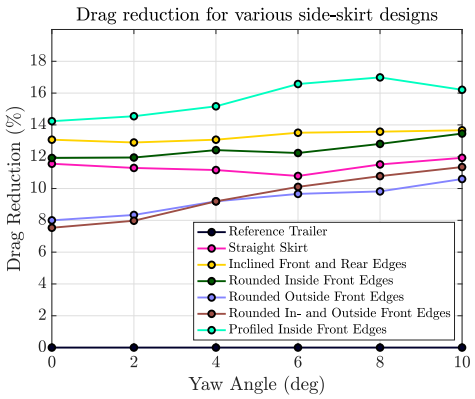

Figure 2.23: Drag reduction for various skirt designs (Plotted with data from Van Raemdonck 2012)

(figure 2.21) was built at $1:6$ scale and tested at $241\ km/hr$. From the results summarised in (K. R. Cooper 2004), it is seen that the skirts caused a reduction in drag by 3.03% at $0°$ yaw and 5.90% at $10°$ yaw. The overall reduction in wind averaged drag (at $104\ km/hr$) over the reference was 5.03%. The results of such early studies, even with the unrepresentative shape of the tractor, showed differences due to the modifications which were comparable to studies that followed much later (K. R. Cooper 2004).

In a detailed study conducted by (Van Raemdonck 2012), among other aerodynamic devices, a series of designs and configurations for side skirts were tested. The experiments used a 1:14 scale model of a truck (TAMIYA Mercedes Benz 1838LS), modified to obtain a turbulent attached boundary layer to the back of the trailer (figure 2.22). The tests were conducted at $60\ m/s$ $(216\ km/hr)$ giving a Reynolds number of 0.8×10^6 based on the square root of the frontal area. Figure 2.23 summarizes the reduction in drag compared to the reference, for few standout designs (figure 2.24), over a range of yaw angles. Here the reference is as shown in figure 2.22, except that the front edges of the trailer were rounded off.

For the most basic straight side skirt, a wind-averaged drag reduction of 11.35% was seen, showing that a basic panel is already quite effective in reducing drag. However, the effectiveness of this skirt reduced with increasing angles of yaw, contrary to the expectation, due to separation from the sharp leading edge at the higher angles. Inclining the otherwise vertical front and rear edges increased the wind averaged

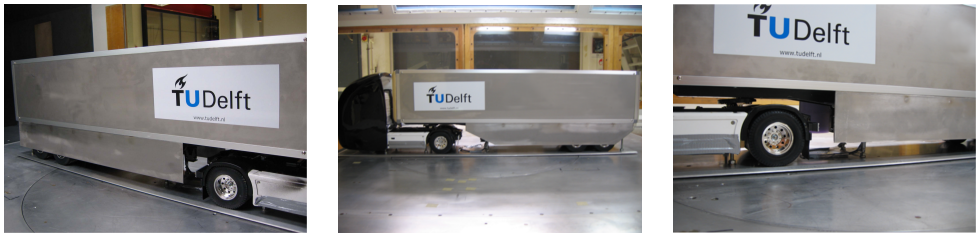

(a) Straight Skirt

(b) Inclined Front and Rear Edges

(c) Rounded Inside Front Edges

(d) Rounded Outside Front Edges

(e) Rounded In- and Outside Front Edges

(f) Profiled Inside Front Edges

Figure 2.24: Side-skirt variants (Credit: Van Raemdonck 2012)

reduction to nearly 14%.

Moving to the skirts with a rounded leading edge (design (c), (d), (e), and (f) in figure 2.24), the results show that the most prominent change is that the effectiveness of the skirts improves with yaw angles for all the cases, although the absolute performance is worse off for 3 of the 4 designs when compared to the skirt with 'Inclined Front and Rear Edges'. The maximum wind averaged drag reduction of 16% was seen for the case labeled 'Profiled Inside Front Edges' which had an airfoil profile on its inside forming the leading edge.

Besides the leading edge, another relevant aspect of skirt design is the geometry with respect to the trailer wheels. The most basic aspect of design here is whether the skirt covers the wheels or not. From (Van Raemdonck 2012) , results of 2 specific cases (figure 2.25) are shown in figure 2.26. It can be seen that for both cases, covering the wheels shows an improvement across all yaw angles. In terms of wind-averaged drag reduction, the case with storage boxes showed a 3% improvement when the wheels were covered (from 12% to 15% over the reference), and the case with the skirt also showed a 3% improvement (from 11% to 14% over the reference).

The investigation by (Landman et al. 2009) also compared similar configurations in terms of placement of the skirt with respect to the wheels (figure 2.28). This experiment was performed at the NASA Langley Full Scale Tunnel on the SOLUS and ODU Representative Heavy Truck (SORHT) model (figure 2.27), a 1:4 scale, class 8, heavy truck model derived from the DOE Generalized Conventional Model (GCM). The Reynolds number based on trailer width was 1.26×10^6. Figure 2.29 shows the results as percent improvement in drag compared to the baseline. An improvement can be seen across the yaw angle range for each subsequent design and, on average, increases with an increase in yaw angle. In terms of wind-averaged drag, the 'Practical Skirt' showed an improvement of 15.82% over the baseline, the 'Extended

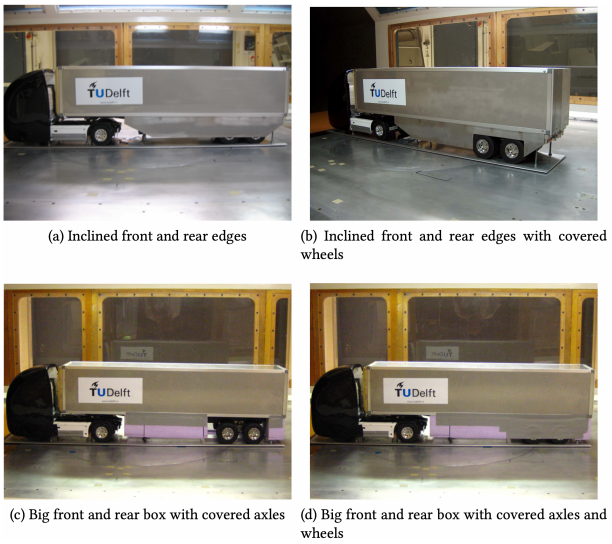

Figure 2.25: Side-skirts with covered and uncovered wheels (Credit: Van Raemdonck 2012)

Figure 2.27: SOLUS and ODU Representative Heavy Truck (SORHT) Model (Credit: Landman et al. 2009)

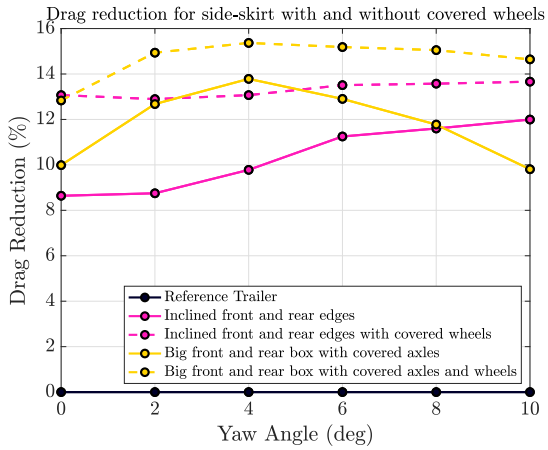

Figure 2.26: Drag reduction for skirts with and without covered wheels (Plotted with data from Van Raemdonck 2012)

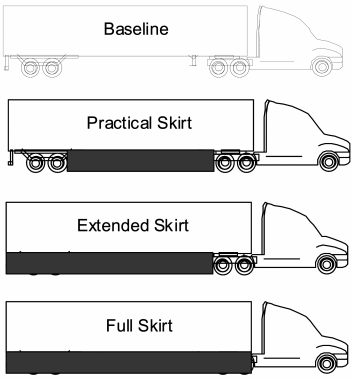

Figure 2.28: Test Configurations for side-skirts (Credit: Landman et al. 2009)

Skirt' showed 17.80%, and the 'Full Skirt' 19.96%.

Another aspect of skirt design with respect to the trailer wheels is the offset of the skirt trailing edge to the leading edge of the trailer wheels. (Eagles and Cragun 2013) looked at this parameter, among others, as part of a Design of Experiments approach to determining the aerodynamic drag response of a truck and trailer across a range of yaw angles. The study used a surrogate modelling method wherein drag data was generated for a large number of skirt designs based on certain fixed parameters (offset mentioned above being one of the seven) and then used to build a model based on the sensitivity of drag to each of the parameters at a given yaw angle.

Figure 2.30a shows the various parameter studies, namely the skirt length, height, leading offset, leading angle, and trailing angle in that numerical order. Besides these, marked Ⓐ in figure 2.30b is the inset angle, and marked Ⓑ is the offset to the trailer wheels, the parameter in focus here. Figure 2.31 shows the change in the drag as a function of this offset for 3 angles of yaw. As can be seen, a reduction in this

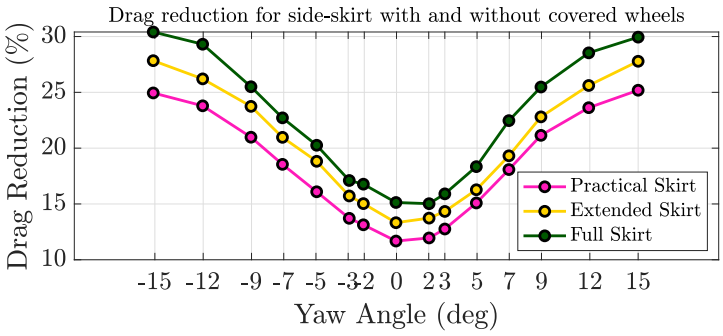

Figure 2.29: Drag reduction for skirts with and without covered wheels (Plotted with data from Landman et al. 2009)

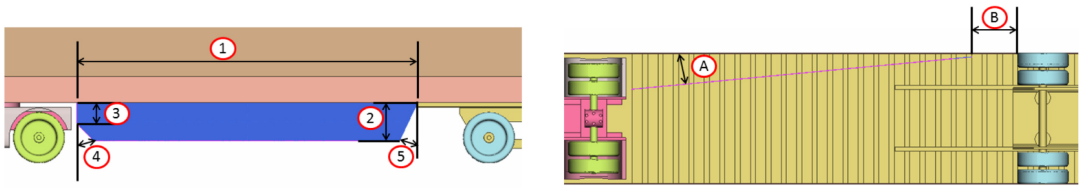

(a) Geometric Parameters (b) Installation Parameters

Figure 2.30: Skirts Parameters (after Eagles and Cragun 2013)

offset benefits drag regardless of the yaw angle, although it is the most for the yaw angle of 3°, giving the impression that the effect of this parameter is higher at moderate angles of yaw, making it particularly significant in real-world scenarios. In the overall ranking of sensitivities across parameters, this offset distance was third, after only the skirt length and height, further pointing to its importance.

2.4.2 Impact of Side Skirts on Flowfield

To gain insight into the effect of skirts on the flowfield in the undercarriage, the results from experiments of (R. Stephens and Babinsky 2016) are used. The details of the experiment are as described earlier in section 2.3. The two configurations compared are shown in figure 2.32. Streamwise velocity contours

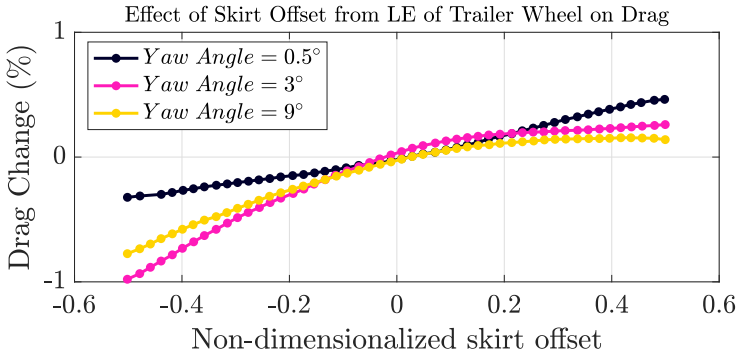

Figure 2.31: Effect of Skirt Offset from LE of Trailer Wheel on Drag (plotted based on data from Eagles and Cragun 2013)

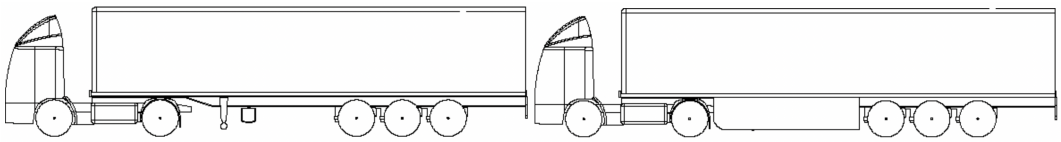

(a) Reference (b) With side-skirt

Figure 2.32: Test Configuration, with and without skirt (Credit: R. Stephens and Babinsky 2016)

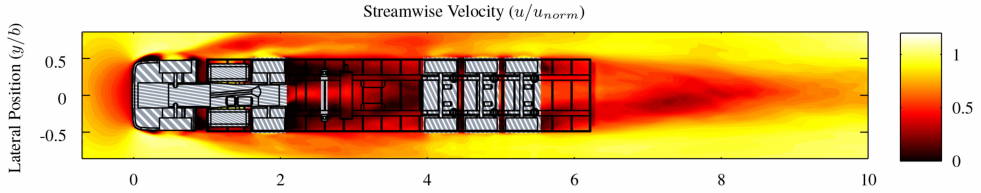

(a) Configuration without skirt

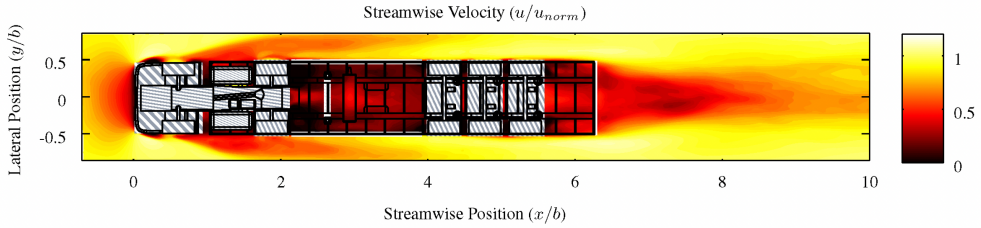

(b) Configuration with skirt

Figure 2.33: Streamwise velocity on plane 'B' (figure 2.16) (Credit: R. Stephens and Babinsky 2016)

on 2 planes, namely 'B' and 'C' (figure 2.16), are discussed.

Figure 2.33 shows the velocity on plane 'B' for both configurations. The region between $x/b = 2$ and $x/b = 2.5$ is very similar, dominated by the wake of the tractor rear wheels in both configurations. For streamwise location between $x/b = 2$ and $x/b = 4$, the configuration without skirt shows relatively higher momentum flow in the laterally outward region, especially in the region upstream of the trailer front wheels, although the differences are in general small.

Plane 'C' (figure 2.34), by contrast, shows much greater differences between the two configurations, primarily because this plane sits sufficiently higher than the bottom horizontal edge of the skirt. The momentum of flow in the region between $x/b = 2$ and $x/b = 4$ is much lower for the skirted trailer. This is because the skirts prevent the inward entrainment of the high momentum flow beside the trailer into the underbody. As a consequence, the bluff components in the underbody obstruct only low momentum flow, thus producing less drag.

For both planes, 'B' and 'C', a clear difference is seen in the region beside the trailer wheels (laterally outside), where the momentum of flow is much higher for the skirted case.

A similar effect of adding skirts is seen in the results from (Hakansson and Lenngren 2010). Figure 2.35 compares the mass flow into the underbody and mass flow into the trailer wheel assembly, for skirted and non-skirted trailers. The mass flow into the underbody region between the rear tractor wheels and the front trailer wheels reduces significantly (22.8 kg/s to 6.9 kg/s). The flow into the trailer axles and

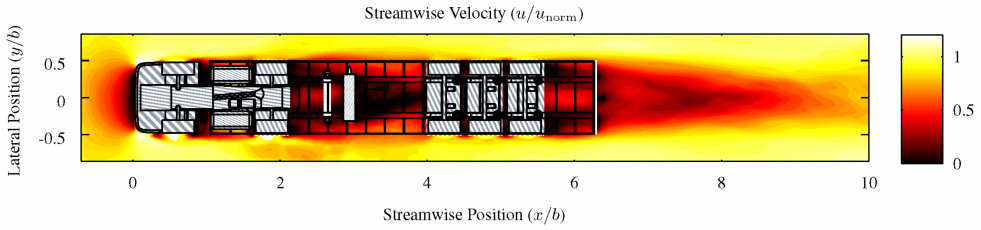

(a) Configuration without skirt

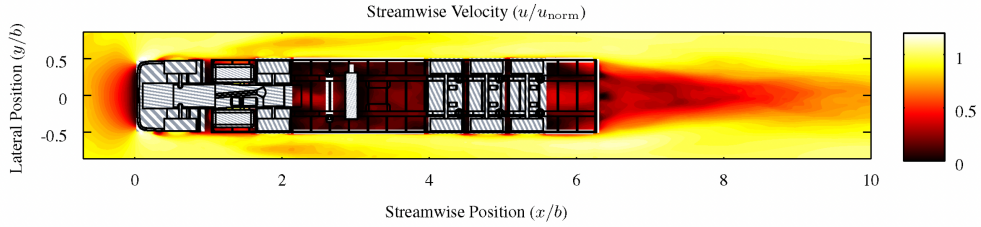

(b) Configuration with skirt

Figure 2.34: Streamwise velocity on plane 'C' (Credit: R. Stephens and Babinsky 2016)

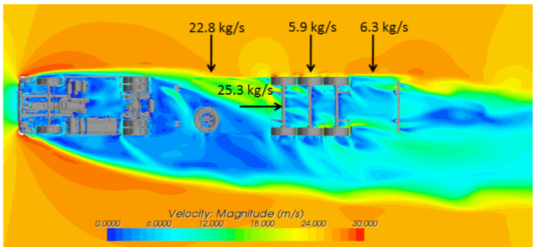

(a) Reference

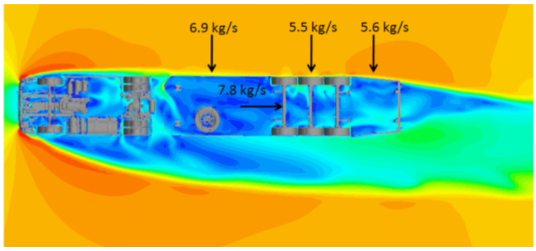

(b) Skirted trailer with uncovered wheels

Figure 2.35: Underbody flow, with and without skirt at 5° yaw (Credit: Hakansson and Lenngren 2010)

wheels also reduces from 25.3 kg/s to 7.8 kg/s.

2.5 Wheel Covers

2.5.1 Isolated Wheel

(Dimitriou and Klussmann 2006) conducted an experimental investigation on, among other setups, an isolated wheel with an open rim and a rim flush covered on both sides (figure 2.36). A generic 1:2 scale open-wheel race car wheel was used, constructed out of aluminium, having a conical shape to reproduce wheel camber. Surface pressure measurements were made on the tread surface, sidewalls, and inside the rim in order to calculate the lift and drag and study the local flow. For this purpose, a 32 channel pressure measurement system was used, mounted inside the tire.

From the integration of surface pressure, it was seen that the wheel with a flush hub cover exhibited lower drag and lift compared to the wheel with an open rim. Overall the drag reduced by 9% and lift by

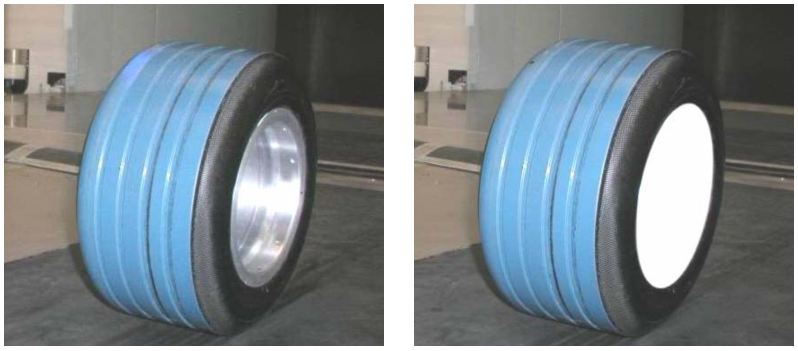

(a) Open Rim (b) Closed Rim

Figure 2.36: Wheel Configuration after Dimitriou and Klussmann 2006

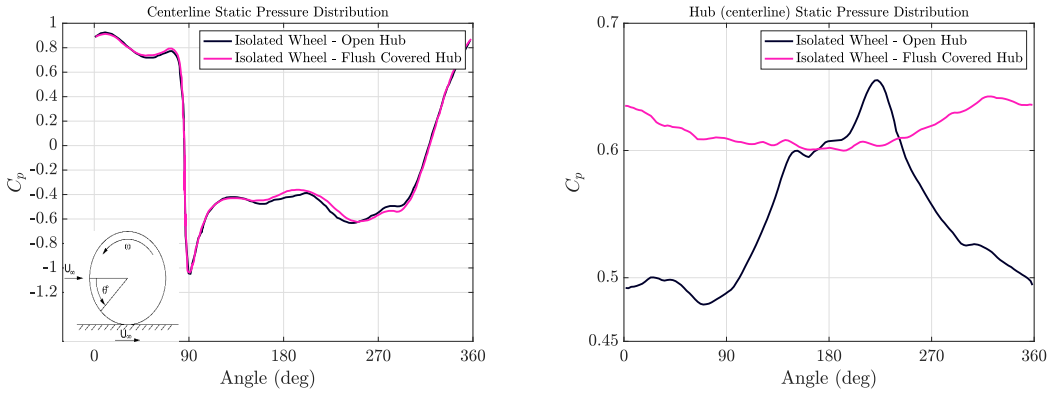

(a) Tread Centerline (b) Rim Centerline

Figure 2.37: Surface Pressure Distribution

16%. A breakdown of the drag over the tread, sidewalls, and rim showed that the drag from the tread reduced by $1\ N$, from the rim by $0.8\ N$, and from the sidewalls by $0.6\ N$.

Figure 2.37a compares the centerline pressure distribution on the tread between the open rim and the closed rim wheel. As can be seen, the pressure distribution is quite similar, except for the base pressure being higher for the covered rim, resulting in the lower drag.

Figure 2.37b compares the pressure at the centerline of the rim. It is seen that on the whole, the pressure does not vary much, remaining in the range of about $C_p = 0.45$ to $C_p = 0.65$ even for the open rim. From this, the authors inferred that the flow inside the rim was separated from the freestream. Moreover, they concluded that the positive and relatively high pressures indicated that the flow inside tended to rotate with the wheel. Finally, the increased pressure from $90°$ to $270°$ for the open rim showed the effect of the freestream, with the air getting trapped in the rear half of the open rim.

2.5.2 Passenger Cars

(Berg and Brandt 2018) conducted both, experimental and numerical, investigations into the aerodynamic effects of different wheel designs in passenger cars. 14 different parameters were evaluated on

the wheel rims of a Volvo estate and sedan vehicle. The authors concluded that the coverage area of the wheel opening was by far the most important design parameter in terms of drag. For design variants with significant openings, it was seen that an outflow existed in the lower part of the wheel. It was reasoned that this outflow feeds the ground vortex of the wheel, thus increasing the drag. Therefore, covering this outer portion of the wheel was considered key to reducing wheel drag.

(Bolzon, Sebben, and Broniewicz 2019) performed a similar study, comparing different wheel configurations, including threaded and slick tires with various coverage areas, achieved by changing the number of spokes. All comparisons were made using a one-fifth scale model of a representative hatchback vehicle, the Volvo Aero 2020. The fully covered slick wheel gave the lowest drag, with the thread pattern adding almost nothing to this baseline. The 10 spoke wheel, designed to work as a fan (pumping action), performed the worst. On the whole, higher coverage areas showed lower drag. Moreover, placing this coverage as far out radially as possible seemed to reduce drag the most.

(Cavusoglu 2017) performed a CFD study of the DrivAer vehicle model, particularly concentrating on the effect of the wheel rim and wheelhouse geometry on the drag. Among other configurations, a comparison between the standard 5-spoked wheel and a completely covered wheel showed a 4.2% decrease in overall drag. The majority of this came from the front wheels (7 counts of drag) followed by the rear (4 counts). The body of the vehicle showed a 2 counts worth of increase in drag.

(Duncan et al. 2010) studied 4 configurations of wheel rims and covers on a hatchback-style vehicle using numerical simulations, coast-down testing, and fixed floor wind tunnel tests. Among these configurations, one involved the complete coverage of the rim using a convex-shaped cover. This resulted in a 2-2.5 % reduction in drag over the baseline case of a 5-spoke wheel, depending on the investigation method. The authors observed that in the lower portion of the wheel, below the vertical level of the front bumper, the presence of a wheel cover allowed the separated flow from the front-facing shoulders of the tire to reattach, thus reducing the drag in the region.

2.5.3 Tractor-trailers

(Leuschen and K. R. Cooper 2006) conducted full-scale wind tunnel tests of various second-generation drag-reducing devices for tractor-trailers, using a Volvo VN 660 tractor. The tests were conducted at the 9m tunnel of the National Research Council of Canada (NRC) , utilizing a fixed floor with fixed wheels. The test velocity was $28.6\ m/s$, resulting in a Reynolds number of 6.7×10^6 based on the square root of the frontal area. Amongst the devices tested were hub caps consisting of solid metal disks, fitted to the outside wheels of the trailer and tractor (figure 2.38a). The results reported as the delta of wind-averaged drag at 100 km/hr, showed an improvement of 0.0020 over the baseline. It was noted that these tests were conducted with fixed wheels and therefore the effects of rotation were unknown. Furthermore, the authors pointed towards the possibility of the covers having a harmful effect on brake cooling.

(Wood 2012) performed on-road fuel consumption tests in accordance with the Society of Automotive Engineers (SAE) J1321 Test Procedure to obtain Environmental Protection Agency (EPA) SmartWay (SW)

(a) Hub Caps after (Leuschen and K. R. Cooper 2006)

(b) Wheel Covers after (Wood 2012)

Figure 2.38: Wheel Cover Installations

Figure 2.39: Model with hub caps fitted

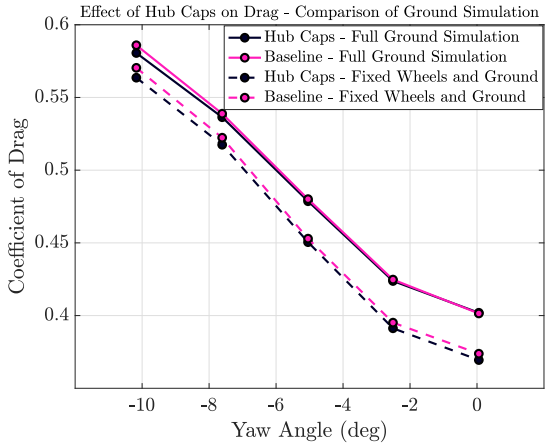

Figure 2.40: Effect of Hub Caps on Drag - Comparison of Ground Simulation

verification for a certain design of wheel cavity cover, among other devices (see figure 2.38b). The cover sat flush panel with the wheel outer rim and included a 203.2 mm circular opening in the middle. In this sense, the design of this cover was in line with the conclusions of (Bolzon, Sebben, and Broniewicz 2019) and (Brandt et al. 2019), which state that the preferred design includes covered surfaces that sit level with the tire bead and include as much outer rim coverage as possible. The results showed a 1.3% decrease in fuel consumption for the wheel cavity covers alone and a 2.4% saving when used in combination with a short skirt sitting aft of the leading trailer wheel.

(Leuschen 2013) performed wind tunnel tests to study the effect of ground simulation on the drag of a tractor with a semi-trailer (experimental details in section 2.2). Figure 2.40 shows the effect of hab caps on the drag, for both fixed floor and wheels as well as a moving belt with rotating wheels. The applicability of these results in the context of trailer wheel covers is limited as the hub caps were fitted only to the tractor rear wheels. Moreover, the trailer wheels were not subject to rotation. Overall, the effect of hub caps on drag was seen to be small, although it did increase with an increase in yaw angle. Furthermore, for the case of fixed wheels and floor, the gain seems to be more than for rotating wheels

and a moving belt, at least at lower yaw angles.

2.6 Literature Study Outcome

From the literature study, it was seen that while much research has been conducted on the aerodynamics of wheel in isolation as well in passenger vehicles, there is, in general, a dearth of literature which specifically deals with the aerodynamics of trailer wheels. This was particularly felt in regards to the quantification of the flowfield in this region. Starting with the simulation of rotating wheels, and ground vehicles in general, in the wind tunnel, a clear discrepancy was seen in the fidelity of tests for isolated wheels and passenger vehicles as compared to commercial vehicles like semi-trucks. Expectedly, the wind tunnel tests of isolated wheels and race cars have long shifted to either using moving ground planes or highly tuned and validated boundary layer removal systems with fixed floors. A similar situation is witnessed for passenger cars, where the use of a 5 belt system (a central belt under the body along with 4 wheel rotation units) has become increasingly common. Moreover, a significant body of published literature is present, comparing various ground simulation techniques, in terms of not only drag values, but also the associated flowfield.

In comparison, wind tunnel tests of commercial vehicles are largely conducted with stationary wheels and a fixed ground plane. Furthermore, comparative experimental studies on ground simulation are largely limited to reporting only the drag values. Keeping in consideration that it is often difficult to accommodate a tractor-trailer in a rolling road setup designed for passenger cars (due to the limited length of the central belt and spacing of the wheel drive units), allowing for wheel rotation by suspending the model off the ground becomes a viable solution. Therefore, studying the effects of wheel rotation in this configuration presents a prudent goal.

Moving on, it was seen that trailer side skirts change the flow in the underbody considerably, especially upstream of the trailer wheels. Therefore, the inclusion of skirts into the geometry is critical for studying the flowfield around trailer wheels. Moreover, it was seen that the coverage of the wheels by the skirts as well as the offset between the trailing edge of the skirt and the leading edge of the wheel can have a significant effect on drag, further incentivizing their inclusion.

Finally, the literature on wheel cavity covers presented various knowledge gaps worth investigating. First is the impact of wheel rotation on the performance of wheel covers, motivated by the predominant use of stationary wheels in the experimental studies reported thus far. Secondly, as mentioned earlier, a key requirement in the design of wheel covers for trailers is access to the wheels for inspection, for which a possible solution is to provide openings in the cover. Despite this, no studies were found that look into the geometric parametrization of these openings and their effect on the drag and flowfield. Lastly, despite various studies advising on the evaluation of the effect of wheel covers on brake cooling, none provided a measurement of the flow in the region.

Chapter 3

Experimental Techniques

The current chapter gives an overview of the basic components of particle image velocimetry, including stereoscopic PIV . Also included is a discussion on the calculation of drag and pressure from PIV.

Section 3.1 gives an introduction to the working principle of PIV. Following this, the individual components that make up a typical PIV setup are discussed, including the choice of tracer particles (section 3.2), illumination (section 3.3), and imaging and optical configuration (section 3.4). Section 3.5 presents, in brief, a discussion on the evaluation of particle motion, followed by the working principle of stereoscopic PIV in section 3.6. Finally, the basics of drag from PIV using a control volume approach are covered in section 3.7, and the basics of pressure from PIV are in section 3.8.

3.1 Operational Principle of Particle Image Velocimetry

Particle image velocimetry involves the determination of fluid velocity by means of measuring the displacement, within a short time interval, of small particles immersed in and traveling with the fluid. These particles, called tracer particles, are illuminated twice, usually with a laser light source, within the small window of time and the scattered light in each case is captured by a camera system onto two subsequent image frames. In principle, from the particle displacement between these image pairs, separated by a known time delta, the tracer particle velocity can be determined. Assuming the local fluid velocity and the tracer particle velocity to be equal (denoted as $\mathbf{u}(\mathbf{x}, t)$) and the time separation between the two illuminations (called pulse separation, denoted by Δt) to be sufficiently small so as to neglect the effect of velocity gradients, the fluid velocity can be determined as in equation 3.1.

$$\mathbf{u}(\mathbf{x}, t) = \frac{\mathbf{x}(t + \Delta t) - \mathbf{x}(t)}{\Delta t} \tag{3.1}$$

In practice, with a high density of tracer particles, as present in PIV, the tracking is not performed on a per-particle basis, but rather on an ensemble of particles present within a subdivision of the image (the interrogation window). For each interrogation window, an average displacement is determined as the

value that maximizes the matching between the pixel intensities at time t and $t+\Delta t$. Figure 3.1 illustrates the typical setup of the most basic PIV, a two-component planar PIV, also called 2D 2C PIV, utilizing a single camera to capture a two-dimensional measurement volume resulting in the determination of the two in-plane velocity components. The individual components of such a setup are discussed in the sections that follow.

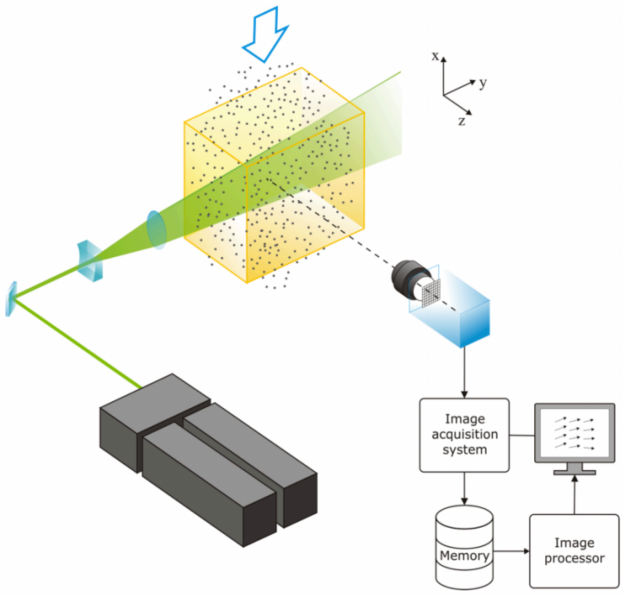

Figure 3.1: Schematic of a typical planar PIV measurement system (Credit: Scarano 2013)

3.2 Tracer Particles

Particle image velocimetry is an indirect technique so far as the velocity of the tracer particles, and not the fluid itself, is measured. Therefore the tracer particles for PIV measurement need to be chosen to track the fluid flow as accurately as possible.

For small tracer particles, where Stokes drag dominates, the difference between the particle velocity $(\mathbf{U}_p)$ and fluid velocity $(\mathbf{U})$ is given as in equation 3.2 (Raffel et al. 2018). As can be seen, this difference (referred to as the slip velocity) is minimized by the use of buoyancy-neutral particles $(\frac{\rho_p - \rho}{\rho} \ll 1)$. In practice, however, for gas flows, this cannot be achieved, requiring, as a result, the use of particles with smaller diameters $(0.5\ \mu m < d_p < 5\ \mu m)$ (Scarano 2013).

$$\mathbf{U}_s = \mathbf{U} - \mathbf{U}_p = d_p^2 \frac{(\rho_p - \rho)}{18\mu} \frac{d\mathbf{U}_p}{dt} \tag{3.2}$$

A convenient measure of the ability of the tracer particles to follow the flow, given that the fluid acceleration is constant and that Stokes drag applies, is the relaxation time (τ_s), which gives the response time of a particle to a sudden change in the fluid velocity (Raffel et al. 2018).

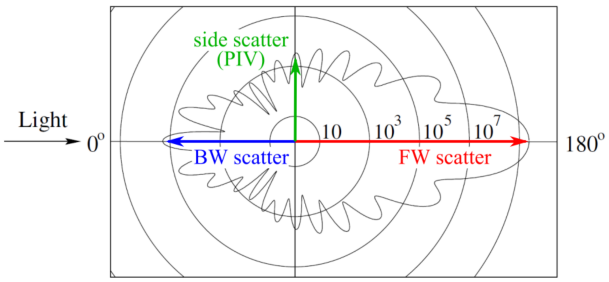

Figure 3.2: Polar distribution of scattered light intensity for an oil particle in air with $d_p = 1$ and light source $\lambda = 532\ nm$ (Credit: Sciacchitano 2014)

$$\tau_s = d_p^2 \frac{\rho_p - \rho}{18\mu} \tag{3.3}$$

This can be utilized to calculate the particle Stokes number (S_k) which is defined as the ratio of the particle response time to the flow characteristic time and indicates the fidelity of the flow tracers in turbulent flows. For practical purposes a particle Stokes number below 0.1 results in acceptable flow tracing with errors below 1% (Scarano 2013).

Along with tracking accuracy, which forces tracer particles towards smaller diameters, the light scattering properties of particles also need to be accounted for. In essence, the particles need to be large enough to scatter enough light to allow for sufficient particle image intensity and therefore contrast in the PIV recordings. For particles with diameters greater than the wavelength of the incident light, typically $532\ nm$, Mie's scattering theory can be applied, which characterizes a particle's scattering by the normalized diameter q, defined by:

$$q = \frac{\pi d_p}{\lambda} \tag{3.4}$$

According to Mie's theory, the ratio of forward to backward scattering increases rapidly with increasing values of the normalized diameter, making it favorable to record images in forward scatter (figure 3.2). In practice, however, due to limited depth of field and optical access, recording is most often performed in side scatter.

3.3 Illumination

The most common source of light for PIV recordings is a laser. This is because they can produce a pulsed, collimated, and monochromatic light beam that can be easily shaped into a thin light sheet by means of spherical and cylindrical lenses. The most commonly used laser is a solid-state frequency-doubled neodymium-doped yttrium aluminium garnet laser (Nd: YAG), which emits light at a wavelength of $532\ nm$, produces pulse energy ranging between $10\ mJ$ and $1\ J$, and has a very short pulse duration (δt), between $5\ ns$ and $10\ ns$ (Scarano 2013).

The pulse duration (or pulse width), is one of the 3 important time-based parameters for image acquisition, others being the pulse separation (Δt) and the time interval between image pairs (ΔT). Figure 3.3 illustrates the meaning of these quantities.

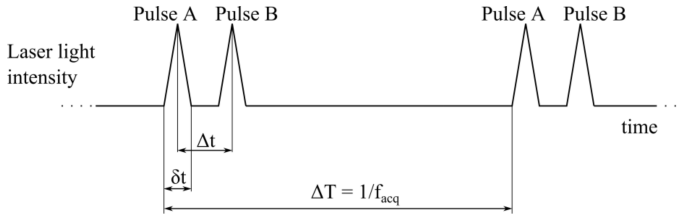

Figure 3.3: Illustration of laser pulse duration (width), pulse separation, and acquisition frequency (Credit: Sciacchitano 2014)

The laser pulse duration needs to small enough such that imaged particle displacement within the pulse duration is significantly smaller than the size of the particle image itself. This is captured in equation 3.5, where d_τ is the particle image diameter, M is the optical magnification of the system, and $\mathbf{U}_p$ is the particle velocity.

$$\delta t \ll \frac{d_\tau}{M\,|\mathbf{U}_p|} \tag{3.5}$$

The next criterion is the pulse separation Δt, which is the time delay between the two light pulses (and therefore images in a pair). Its value needs to be chosen such that the majority of particles are imaged in the same window for both the images in an image pair. This ensures that the number of particle pairs is large, which in turn increases the probability of the highest correlation peak corresponding with the actual particle motion. The one-quarter rule for the in-plane particle image displacement, i.e. the maximum in-plane displacement should be smaller than the interrogation window size, and the one-quarter rule for the out-of-plane particle displacement, i.e. the maximum out-of-plane displacement should be less than the light sheet thickness, are usually used to find an upper bound on Δt.

Finally, the time interval between image pairs (ΔT) is usually shown instead as a measurement rate or acquisition frequency and determines if subsequent velocity fields are correlated or uncorrelated in time.

3.4 Imaging of tracer particles

Figure 3.4 shows a schematic of the optical configuration used in planar PIV imaging which includes a light sheet of finite thickness (object plane), camera sensor (image plane), and an imaging lens (objective), located at a certain distance from each other. The light sheet illuminates the tracer particles within it, an image of which is formed by means of a lens on the surface of the image sensor (usually a CCD, CMOS, or sCMOS sensor). For successful imaging of the tracer particles, various optical parameters

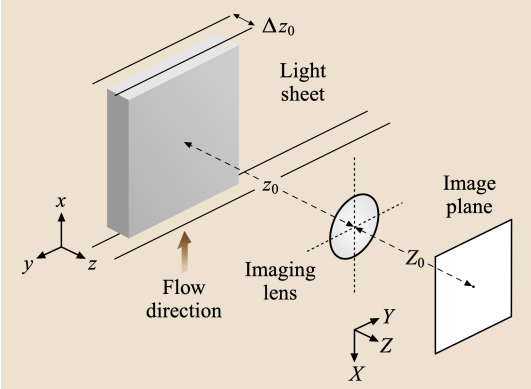

Figure 3.4: Schematic of the optical configuration for PIV imaging (Credit: Westerweel 1997)

that characterize the imaging system need to be considered and chosen carefully. Primary among these are the image magnification (M), the focal length of the lens (f), and the f-stop or aperture number of the lens $(f_\#)$.

Image magnification is defined as the ratio of the image distance (Z_o) and object distance (z_o) (equation 3.6). It can also be interpreted as the ratio between the image size (sensor size) and the imaged object size and is therefore a consequence of the field of view of interest for the measurement. Moreover, the thin lens formula (equation 3.7), ie. for a lens with thickness much smaller than the focal length, relates the focal length of the lens with the optical system distances and therefore, for a certain object distance (based on physical considerations) and image magnification, gives an indication of the required focal length.

$$M = \frac{Z_o}{z_o} = \frac{sensor\ size}{imaged\ object\ size} = \frac{pixel\ size \times no.\ of\ pixels}{Field\ of\ view} \tag{3.6}$$

$$\frac{1}{f} = \frac{1}{z_o} + \frac{1}{Z_o} \tag{3.7}$$

Another parameter that characterizes the imaging lens is the f-stop or aperture number, defined as the focal length divided by the aperture diameter, the choice of which affects the particle image diameter and the depth-of-field.

For an aberration-free lens with a circular aperture, the particle image diameter (d_τ) is obtained as the Euclidean sum of the diffraction-limited spot diameter (d_s) and the particle image geometric diameter $(Md_p$, where d_p is the particle diameter) (equation 3.8).

$$d_\tau = \sqrt{d_s^2 + (Md_p)^2} \tag{3.8}$$

For a tracer particle illuminated by the light sheet, the diffracted light behaves as a point source $(d_p \to 0)$. For such a source, due to diffraction effects, the image does not show as a point, but rather as a small spot, known as the Airy disc, surrounded by diffraction rings of decreasing brightness. The extent of the

Airy disc, defined by the first dark ring of the Airy pattern, can be evaluated from the first zero of the first-order Bessel function. This results in a diffraction-limited spot diameter as expressed by equation 3.9 (Raffel et al. 2018), which essentially puts a lower limit on the particle image diameter. In practice, for the typical values of the various optical parameters in PIV, the diffraction-limited spot diameter is much greater than the particle image geometric diameter and therefore the diffraction limit generally dominates the particle image formation.

$$d_s = 2.44 f_{\#}(1 + M)\lambda \tag{3.9}$$

For imaging with digital cameras, the particle image diameter should be kept around 2 to 3 pixels. Particle image diameter smaller than 1 pixel leads to optical undersampling wherein the particle position cannot be detected with subpixel accuracy leading to systematic errors in the calculated particle displacement. The condition is known as *pixel locking* or *peak locking* due to the particle displacements getting locked into integer values. On the other hand, a particle image diameter much greater than 3 can lead to the overlapping of the individual particle images resulting in a decreased image contrast and spatial resolution of the measurement. Finally, the focal depth, given by equation 3.10 (Raffel et al. 2018), represents the range in which the particles are in focus and imaged with sharpness. The focal depth should be kept greater than the thickness of the light sheet.

$$\delta z = 4.88 \left(\frac{1 + M}{M} \right)^2 f_{\#}^2 \lambda \tag{3.10}$$

3.5 Evaluation of tracer particle motion field

As noted earlier, in particle image velocimetry, the tracking of particle motion is not performed on a per-particle basis, but rather on an ensemble of particles present within a subdivision of the image called the interrogation window. Therefore the first step in evaluating particle image motion includes dividing the image into small windows (typically between 16×16 pixels and 128×128 pixels), each having a statistically significant number of tracers (at least 10) (Scarano 2013).

Next, in each of the interrogation windows, an average displacement is determined as the value that maximizes the matching between the pixel intensities between the images of an image pair. For this purpose, in the case of digital image recording systems, a discrete cross-correlation function is computed as in equation 3.11, where I_a and I_b are image intensities for the two images, discretized at the pixel locations (i, j). $\overline{I_a}$ and $\overline{I_b}$ represent the mean value (spatially) of the intensity within the interrogation window, subtracted from I_a and I_b respectively to remove the DC component of the signal. Moreover, the cross-correlation function is normalized, in range $[-1, 1]$, to reduce sensitivity to changes in intensities between the two images. The position of the peak, relative to the origin, of the resultant discrete cross-correlation map $C(m, n)$ gives the average particle image displacement.

$$C(m,n) = \frac{\sum_{i=1}^{M}\sum_{j=1}^{N}\left[I_a(i,j) - \overline{I_a}\right]\cdot\left[I_b(i+m,j+n) - \overline{I_b}\right]}{\sqrt{\sum_{i=1}^{M}\sum_{j=1}^{N}\left[I_a(i,j) - \overline{I_a}\right]^2 \cdot \sum_{i=1}^{M}\sum_{j=1}^{N}\left[I_b(i,j) - \overline{I_b}\right]^2}} \tag{3.11}$$

In practice, the discrete cross-correlation function is not implemented numerically according to its definition due to the computational intensiveness ($(2n \times 2m)^2$ operations for an interrogation window of $n \times m$ pixels). Instead, increased efficiency is gained through the use of Fourier Transform based on the Wiener-Khintchine theorem, and the use of Fast Fourier Transform (FFT) algorithm to calculate the Discrete Fourier Transform (Scarano 2013).

Due to the discrete nature of the cross-correlation function defined above, the resulting particle image displacement is limited to an integer value in pixel units. For a correlation peak that covers more than one pixel, a more accurate peak position, with sub-pixel accuracy, can be calculated using interpolation. Among other methods, a Gaussian peak fit algorithm shows the best performance, with the rationale that the correlation of Gaussian functions, which are shown to accurately describe the particle image (Airy function), results in a cross-correlation function peak with a Gaussian shape.

Finally, the particle motion in terms of pixel shift is divided by the pulse separation, multiplied by the pixel size, and divided by the optical magnification to yield the velocity in the object reference frame. This is represented as:

$$\mathrm{u}_{\text{object reference}} = \text{pixel shift} \times \text{pixel size} \times \frac{1}{\Delta\mathrm{t} \times \mathrm{M}} \tag{3.12}$$

3.6 Operational Principle of Stereoscopic PIV

Stereoscopic PIV, by the use of two cameras at different observation angles, allows the reconstruction of a three-component displacement vector in the plane of the light sheet, enabling the measurement of the out-of-plane velocity component in addition to decreasing the error in the in-plane velocities caused by the contamination of the in-plane displacements, when measured by a single camera setup, by the unaccounted for out-of-plane displacement, especially towards the edges of the field of view. Figure 3.5 shows the basic schematic of a stereoscopic PIV setup.

In such a setup, called the angular method, the image plane is placed at an angle to the optical axis of the lens, called the Scheimpflug configuration, in order to keep all particle images in focus (figure 3.6). As a result, due to the non-parallel object and image planes, the image magnification varies over the field of view, leading to perspective deformation of the image (figure 3.7). A general method to correct for this is to form polynomial mapping functions between the image coordinates and the object coordinates using a calibration target (Prasad 2000).

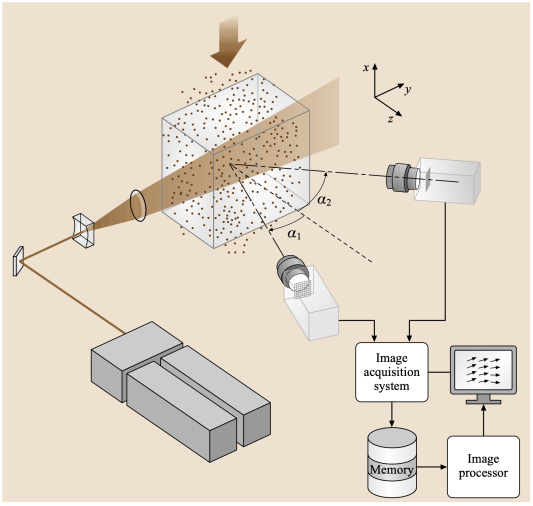

Figure 3.5: Schematic of a stereoscopic PIV measurement system (Credit: J. Westerweel et al. 2007)

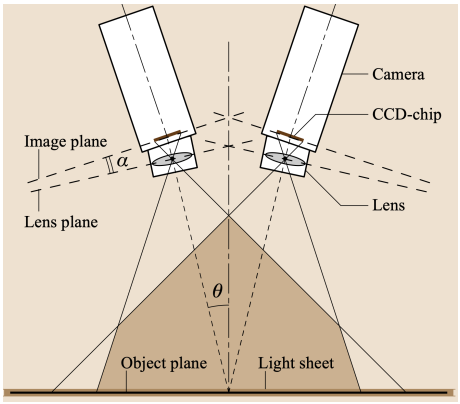

Figure 3.6: Optical configuration for stereoscopic imaging with angular method (Credit: J. Westerweel et al. 2007)

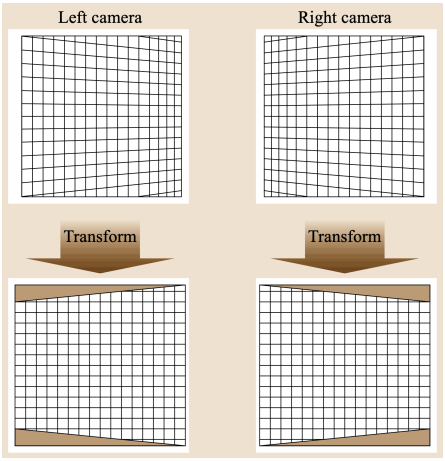

Figure 3.7: Perspective deformation due to the angular method in stereoscopic viewing (Credit: J. Westerweel et al. 2007)

In order to obtain the out-of-plane component, a three-dimensional calibration procedure (for example the Soloff method, Soloff, Adrian, and Liu 1997, amongst others) needs to be performed. Such a procedure images the calibration target at 2 or more positions in the normal direction to the object plane, in order to fit a polynomial relating a three-dimensional position in the object space with a two-dimensional position in each of the two image planes.

When using such a calibration method for stereoscopic reconstruction, it is crucial that the calibration plate coincides with the light sheet. Failure to do so results in registration errors and artifacts in the results (J. Westerweel et al. 2007). As this is difficult to produce in practice, errors due to small misalignments are corrected by a self-calibration procedure (disparity map) (Wieneke 2005), wherein cross-correlation is performed on simultaneous particle images recorded from the two cameras.

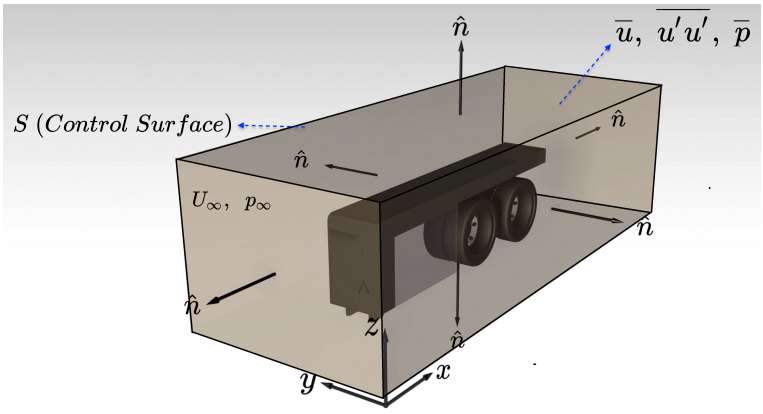

Figure 3.8: Schematic of the control volume, indicating the axis system, quantities on the upstream / downstream planes, and the positive orientation of the control surface S

3.7 Drag Estimation from PIV

Drag estimation from PIV is possible by applying a momentum balance to a control volume V, delimited by a control surface S, which includes the surface of the aerodynamic object of interest. For such a setup, Newton's second law prescribes that the net force acting on the object is equal to the time rate of change of momentum within the control volume. For a control volume that is shrunk to the model, i.e. the control surface coincides with the surface of the model, the net force on the model is only a consequence of the normal (pressure) and viscous (shear) stresses that act on the control surface. These are the third and fourth terms in equation 3.13. However, when the momentum balance needs to be evaluated away from the model surface (as in the case of PIV), additional accounting is needed for the time rate of change of momentum within the control volume and convection of momentum across the control surface (first and second term respectively in equation 3.13).

$$\mathbf{F}(t) = \underbrace{-\rho \iiint_V \frac{\partial \mathbf{V}}{\partial t} d}_{Unsteady\ term} \underbrace{- \rho \iint_S (\mathbf{V}\cdot\mathbf{n})\mathbf{V} dS}_{Convective\ term} \underbrace{- \iint_S p\mathbf{n} dS}_{Normal\ stresses} \underbrace{+ \iint_S \tau \mathbf{n} dS}_{Viscous\ stresses} \tag{3.13}$$

Using an axis system such that the x direction is aligned with the freestream, z direction points upwards and y points sideways (figure 3.8), taking $\mathbf{n}dS = [dydz \quad -dxdz \quad -dxdy]^T$ along with the consideration that the control surface S has a positive orientation, and writing equation 3.13 in cartesian coordinates (neglecting the viscous stresses), the following is obtained:

$$\begin{bmatrix} F_x \\ F_y \\ F_z \end{bmatrix} = -\rho \iiint_V \begin{bmatrix} \frac{\partial u}{\partial t}\, dxdydz \\ \frac{\partial v}{\partial t}\, dxdydz \\ \frac{\partial w}{\partial t}\, dxdydz \end{bmatrix} + \rho \iint_S \begin{bmatrix} -u^2\, dydz + uv\, dxdz + uw\, dxdy \\ -uv\, dydz + v^2\, dxdz + vw\, dxdy \\ -uw\, dydz + vw\, dxdz + w^2\, dxdy \end{bmatrix} + \iint_S \begin{bmatrix} -p\, dydz \\ p\, dxdz \\ p\, dxdy \end{bmatrix} \tag{3.14}$$

Taking only the drag force from the above equation (F_x), it can be seen that for a large enough control volume, such that the v velocity component on the xz control surfaces and w velocity component on the xy control surfaces can be assumed to be zero, simplifications occur (equation 3.15) which allow for the estimation of drag only from control surfaces upstream and downstream of the model.

$$F_x(t) = -\rho \iiint_V \frac{\partial u}{\partial t}\, dxdydz + \rho \iint_S -u^2\, dydz + \cancelto{0}{uv\, dxdz} + \cancelto{0}{uw\, dxdy} - \iint_S p\, dydz \tag{3.15}$$

Moreover, if upstream conditions are those of the freestream, PIV measurement in only the wake is needed. Implementing this in equation 3.15, the following is obtained:

$$F_x(t) = -\rho \iiint_V \frac{\partial u}{\partial t}\, dxdydz + \rho \left(\iint_{upstream} U_\infty^2\, dydz - \iint_{downstream} u^2\, dydz \right) + \iint_{upstream} p_\infty\, dydz - \iint_{downstream} p\, dydz \tag{3.16}$$

Applying conservation of mass to the control volume (equation 3.17), and substituting in equation 3.16, gives the final form of the instantaneous drag force (equation 3.18).

$$\iint_{upstream} \rho U_\infty\, dydz = \iint_{downstream} \rho u\, dydz \tag{3.17}$$

$$F_x(t) = -\rho \iiint_V \frac{\partial u}{\partial t}\, dxdydz + \rho \left(\iint_{downstream} (U_\infty - u)u\, dydz \right) + \iint_{downstream} (p_\infty - p)\, dydz \tag{3.18}$$

To obtain the time-averaged drag force, the velocity and pressure terms in equation 3.18 are decomposed into mean and fluctuating parts: $u = \overline{u} + u'$ and $p = \overline{p} + p'$, where the overbar represents the mean quantities $(\overline{u},\ \overline{p})$ and the prime represents the fluctuating terms $(u',\ p')$, after which Reynolds averaging

is applied to each of the terms, resulting in equation 3.19. Rearranging the central term and neglecting the time rate of change of the mean streamwise velocity in the control volume (steady-state approximation), the final form of the time-averaged drag force is obtained as in equation 3.20.

$$\overline{F_x(t)} = -\rho \iiint_V \frac{\partial \overline{u}}{\partial t}^{0} dxdydz + \rho \left(\iint_{downstream} (U_\infty \overline{u} - \overline{u}^2 - \overline{u'u'})\, dydz \right) + \iint_{downstream} (p_\infty - \overline{p})\, dydz \tag{3.19}$$

$$\overline{F_x} = \rho \iint_{downstream} (U_\infty - \overline{u})\overline{u}\, dydz - \rho \iint_{downstream} \overline{u'u'}\, dydz + \iint_{downstream} (p_\infty - \overline{p})\, dydz \tag{3.20}$$

3.8 Pressure from PIV

As suggested by equation 3.20, to estimate the aerodynamic drag of a model, the pressure field in a downstream plane is needed in addition to the velocity field. Because particle image velocimetry does not directly measure the pressure, this information needs to be derived from the PIV velocity data, as detailed in (Van Oudheusden 2013).

Under incompressible flow conditions, ignoring body forces, the conservation of momentum equation reads as follows:

$$\nabla p = -\rho \frac{D\mathbf{u}}{Dt} + \mu \nabla^2 \mathbf{u} \tag{3.21}$$

Here $\frac{D\mathbf{u}}{Dt}$ is the substantial derivative (total derivative w.r.t time) of the velocity field which, in an Eulerian perspective, can be seen as a combination of the local time rate of change of velocity and the convective acceleration contribution. (equation 3.22)

$$\frac{D\mathbf{u}}{Dt} = \frac{\partial \mathbf{u}}{\partial t} + (\mathbf{u} \cdot \nabla)\mathbf{u} \tag{3.22}$$

Equation 3.21 can be combined with the continuity equation for incompressible flows ($\nabla \cdot \mathbf{u} = 0$), to obtain an equation for pressure. Since the continuity equation has a divergence form, this is done by taking the divergence of the momentum equation, which for constant density and viscosity results in equation 3.23, an elliptic equation (Poisson equation for the pressure if velocity field is known).

$$\nabla^2 p = \nabla \cdot (-\rho \frac{D\mathbf{u}}{Dt} + \mu \nabla^2 \mathbf{u}) = -\rho \nabla \cdot (\mathbf{u} \cdot \nabla)\mathbf{u} \tag{3.23}$$

For extracting the time-averaged pressure field, the momentum equation is subject to Reynolds-averaging, which results in the mean pressure gradient as in equation 3.24 and the corresponding Poisson equation, eq. 3.25.

$$\nabla \overline{p} = -\rho(\overline{\mathbf{u}} \cdot \nabla)\overline{\mathbf{u}} - \rho \nabla \cdot (\overline{\mathbf{u}'\mathbf{u}'}) + \mu \nabla^2 \overline{\mathbf{u}} \tag{3.24}$$

$$\nabla^2 \overline{p} = -\rho \nabla \cdot (\overline{\mathbf{u}} \cdot \nabla)\overline{\mathbf{u}} - \rho \nabla \cdot \nabla \cdot (\overline{\mathbf{u}'\mathbf{u}'}) \tag{3.25}$$

In the cartesian coordinate system, with z being normal to the measurement plane (see figure 3.8), equation3.24 can be written a follows:

$$\begin{aligned}
\frac{\partial \overline{p}}{\partial z} &= -\rho \left\{ \overline{w}\frac{\partial \overline{w}}{\partial z} + \overline{v}\frac{\partial \overline{w}}{\partial y} + \frac{\partial \overline{w'w'}}{\partial z} + \frac{\partial \overline{v'w'}}{\partial y} \right\} + \mu \left\{ \frac{\partial^2 \overline{w}}{\partial z^2} + \frac{\partial^2 \overline{w}}{\partial y^2} \right\} + \left\{ \overline{u}\frac{\partial \overline{w}}{\partial x} + \frac{\partial \overline{u'w'}}{\partial x} + \frac{\partial^2 \overline{w}}{\partial x^2} \right\} \\
\frac{\partial \overline{p}}{\partial y} &= -\rho \left\{ \overline{w}\frac{\partial \overline{v}}{\partial z} + \overline{v}\frac{\partial \overline{v}}{\partial y} + \frac{\partial \overline{v'w'}}{\partial z} + \frac{\partial \overline{v'v'}}{\partial y} \right\} + \mu \left\{ \frac{\partial^2 \overline{v}}{\partial z^2} + \frac{\partial^2 \overline{v}}{\partial y^2} \right\} + \left\{ \overline{u}\frac{\partial \overline{v}}{\partial x} + \frac{\partial \overline{v'u'}}{\partial x} + \frac{\partial^2 \overline{v}}{\partial x^2} \right\}
\end{aligned} \tag{3.26}$$

As can be seen, the planar pressure field has contributions from out-of-plane motion which are not measured in a stereoscopic setup. These contributions, noted separately in the third term on the RHS in equation 3.26, are therefore neglected.

The Poisson equation for pressure (with the form $\bar{p}_{xx} + \bar{p}_{yy} = F(x, y)$, where F is known from the velocity data) can be solved using the finite difference method on a uniformly spaced rectangular grid. The finite difference approximation of the LHS of the above equation, applied to the inner points of the domain, using a second-order centered-difference approximation for both $\bar{p}_{xx}$ and $\bar{p}_{yy}$, results in the so-called five-point approximation, wherein the solution at every grid point depends on the solutions at the four neighboring grid points (equation 3.27).

$$\frac{1}{h^2}\left(\bar{p}_{i+1,j} + \bar{p}_{i-1,j} - 4\bar{p}_{i,j} + \bar{p}_{i,j+1} + \bar{p}_{i,j-1}\right) = F_{i,j} \tag{3.27}$$

Here h is the grid spacing, uniform and equal in both directions. For the boundary points, the Dirichlet boundary conditions can be applied directly whereas the Neumann conditions can be incorporated using fictitious points (ghost points) outside the domain, the field value at which can be calculated from the field value at the internal point and the Neumann condition at the boundary. Figure 3.9 shows this, wherein the lattice has been extended so as to allow the use of central difference scheme on the boundary as well. Therefore,

$$\frac{\partial \overline{p}}{\partial n}(x_1, y_j) = \frac{\overline{p}_{2,j} - \overline{p}_{0,j}}{2h} + \mathcal{O}(h^2)$$

Here the value of $\overline{p}_{0,j}$ is not defined. Therefore it needs to be eliminated from the equation of the five-point approximation, which can be done using the Neumann boundary condition. Therefore,

$$\overline{p}_{0,j} = \overline{p}_{2,j} - 2hg_{1,j} \quad \text{where} \quad g = \frac{\partial \overline{p}}{\partial n} \text{ on the boundary}$$

At the corner points 2 ghost points are defined as can be seen in the figure. A similar procedure can be applied to both of them to define the five-point approximation of the corner point.

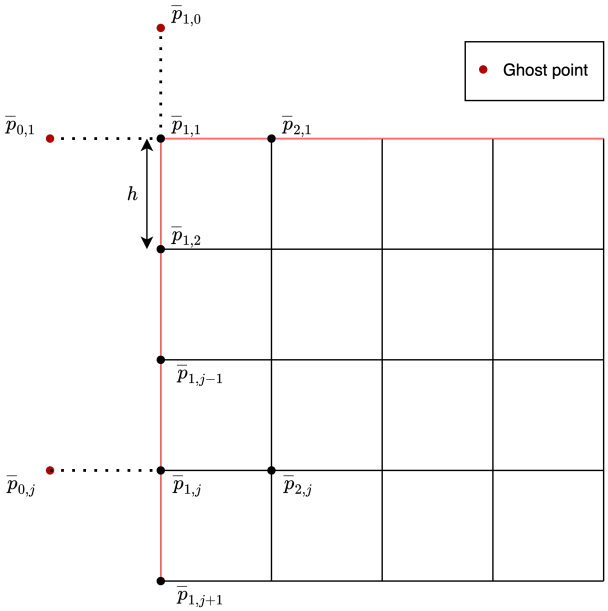

Figure 3.9: Ghost points for Neumann boundary conditions

The resulting set of implicit finite difference equations can be solved using various methods, e.g. Gaussian elimination or LU factorization. In matrix-vector form, the set can be written as $A\mathbf{p} = \mathbf{F}$, where A is a discrete representation of the Laplace operator, $\mathbf{p}$ is the vector of unknown pressure terms, and $\mathbf{F}$ is the source term that can be calculated from the pressure gradients as defined by equation 3.26. (detailed in sub-section 4.4.3)

Chapter 4

Experimental Setup and Data Reduction

The following chapter describes the details of the experimental setup and data reduction. Section 4.1 includes the wind tunnel setup and the model details. The various configurations tested are detailed in section 4.2. The experimental setup, including the PIV hardware and processing parameters, is presented in section 4.3. Section 4.4 describes the steps taken to calculate drag from the PIV data, including corrections to the freestream velocity (sub-section 4.4.1), calculation of the Reynolds stress terms (sub-section 4.4.2) and reconstructing pressure from PIV (sub-section 4.4.3). Finally, section 4.5 includes the expressions used for calculating the uncertainty of the measured drag, obtained using the linear uncertainty propagation formula.

4.1 Wind tunnel setup and model details

The experiments were conducted at the W-tunnel of the Aerodynamic Laboratories of TU Delft. This tunnel can be run with an open or closed test section; in this study, the open jet configuration was preferred to reduce the effects of a large solid blockage. The tunnel can also be fitted with nozzles of different areas; in this study a square nozzle with an exit area of $0.6m \times 0.6m$ was used, resulting in a blockage of 5.16%. The freestream was set to $13\ m/s$ resulting in a wheel diameter based Reynolds number of 1.17×10^5.

The tests were conducted on a simplified model of a trailer wheel, placed in tandem with another, and shrouded by a body with a radiused front edge (figure 4.1). The body allowed for adding and removing configurations of trailer skirts as required (description of configurations tested is given later).

The wheel geometry and dimensions are shown in figure 4.2. As can be seen, the wheel is the so-called dual wheel, with two tires on rims that are joined together near the hub of the wheel. The model representation of the tire was machined out of plastic while the hub was machined from aluminium. An $8\ mm$ shaft connected the hubs, through a system of pulleys, to a DC motor, which was directly controlled using a DC power supply. The rotation speed was measured with an optical tachometer and set

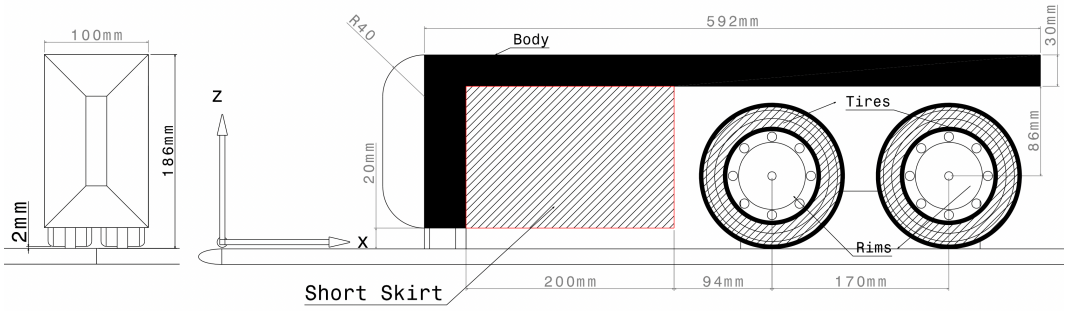

Figure 4.1: Wind tunnel model: geometry and dimensions

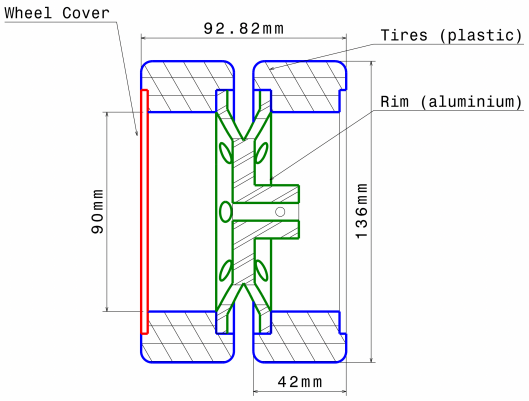

Figure 4.2: Wheel geometry and dimensions

such that the tangential speed of the wheels matched the freestream $(1895 \pm 10\ rpm)$. The entire assembly was placed on a stationary ground board such that the wheels sat $2\ mm$ off the surface to allow for rotation. The ground board itself was elevated $20\ mm$ above the lower surface of the nozzle exit and its front edge was radiused to prevent separation.

4.2 Test configurations

Five configurations of the model were tested, including a short and a long trailer skirt, and solid wheel covers, both with rotating and stationary wheels. Furthermore, wheel covers with openings varying in the percentage of coverage and their radial position were tested with only rotating wheels. Figure 4.3 shows the various configurations. The presence or absence of the short skirt can be seen to reflect the difference between a small and a large gap, respectively, between the trailing edge of a skirt and the leading edge of a wheel in case of an actual trailer assembly. The long skirt covers the wheels completely. The covers shown in figure 4.3 are solid disks sitting flush the sidewall of the wheel. These were tested both with and without the short trailer skirt.

The wheel covers with openings are shown in figure 4.4. Three radial positions were tested, inner, middle, and outer as seen from the hub going radially outwards. Figure 4.5 shows the bands that defined each of these positions. Marked in red is the inner band, in green the middle, and in blue the outer; dimensions are also color-coded. For each of these positions 3 coverage percentages were tested, 50%,

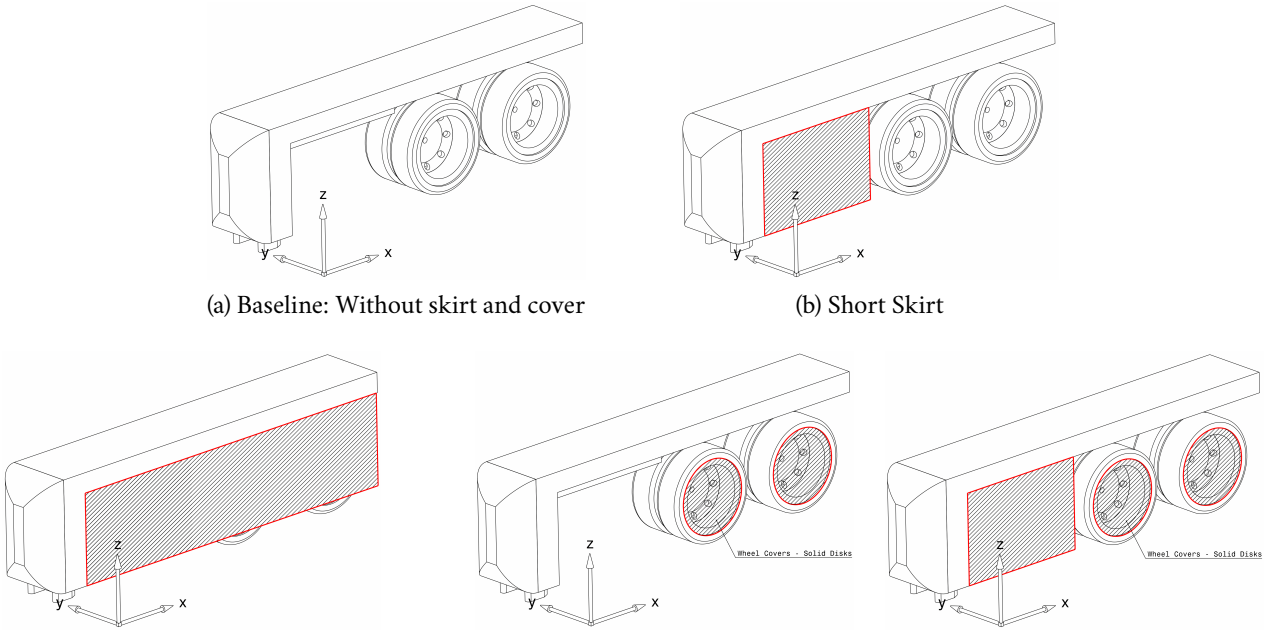

(a) Baseline: Without skirt and cover

(b) Short Skirt

(c) Long Skirt

(d) Solid Covers

(e) Short Skirt and Solid Covers

Figure 4.3: Test configurations: Skirts and Solid Covers

70% and 90%. In each of the cases, regardless of the radial position of the holes, the percentage coverage is a percentage of the annular area marked using hatching in figure 4.5.

4.3 Experimental setup and PIV parameters

A stereoscopic PIV setup was used to make velocity measurements at 5 planes, 4 beside the model and 1 in its wake. Figure 4.6 shows the model and measurements planes, plane A is beside the first wheel and placed at the axis of rotation. Each of the other planes is offset by $85\ mm$ as in the figure, resulting in plane C being on the axis of the second wheel. The wake was measured on a plane approximately $190\ mm$ downstream of the model.

The experimental setup is shown in figure 4.7. Measurements were obtained using two LaVision *Imager sCMOS* cameras ($2560 \times 2160\ pixels^2$, 16 bits, and $6.5\ \mu m$ pixel pitch). Illumination was provided by a *Quantel Evergreen* 200 laser (Nd:YAG, $2 \times 200\ mJ$, $15\ Hz$). The flow was seeded using a SAFEX fog generator, producing water-glycol based particles, with a $1\ \mu m$ diameter. Calibration was performed using a LaVision Type 30 plate, with the pin-hole model. The acquired images were preprocessed by subtracting the minimum intensity using a time series filter for each pixel position to lower the background noise and masking the regions containing reflections off the wheel surface. Further details of the hardware settings and processing parameters are in table 4.1.

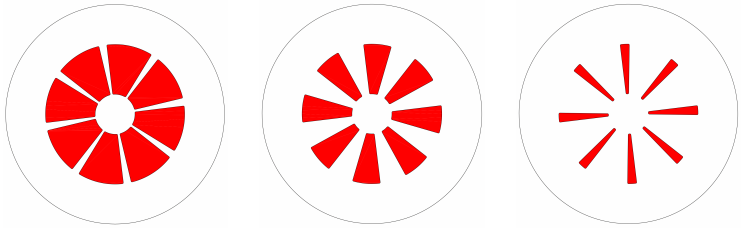

(a) 50% Coverage - Inner opening

(b) 70% Coverage - Inner opening

(c) 90% Coverage - Inner opening

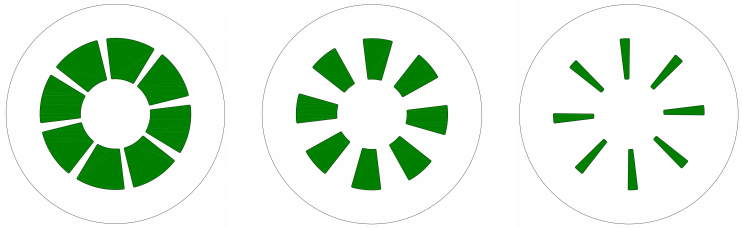

(d) 50% Coverage - Middle opening

(e) 70% Coverage - Middle opening

(f) 90% Coverage - Middle opening

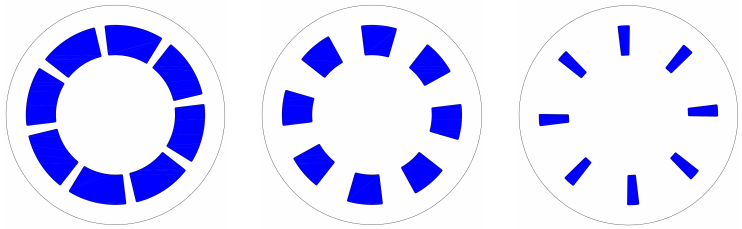

(g) 50% Coverage - Outer opening

(h) 70% Coverage - Outer opening

(i) 90% Coverage - Outer opening

Figure 4.4: Wheel cover configurations: coverage area and radial placement of openings

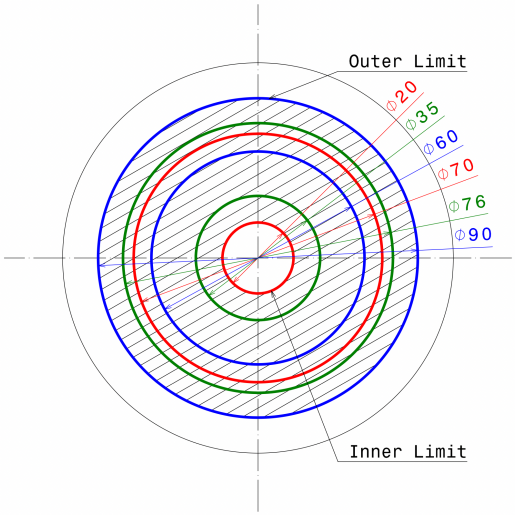

Figure 4.5: Wheel cover geometrical parameters, upper and lower radial limits - *in Red*: inner radial placement, *in Green*: middle radial placement, *in Blue*: outer radial placement

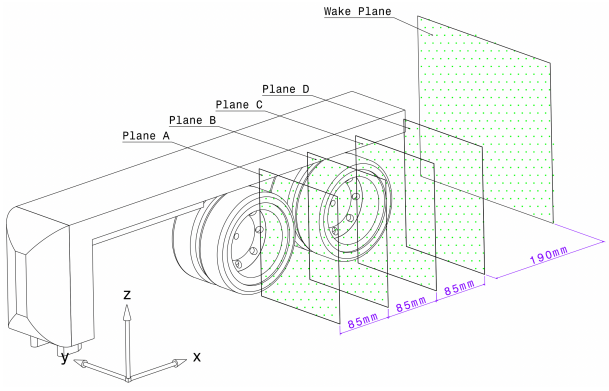

Figure 4.6: Measurement Planes

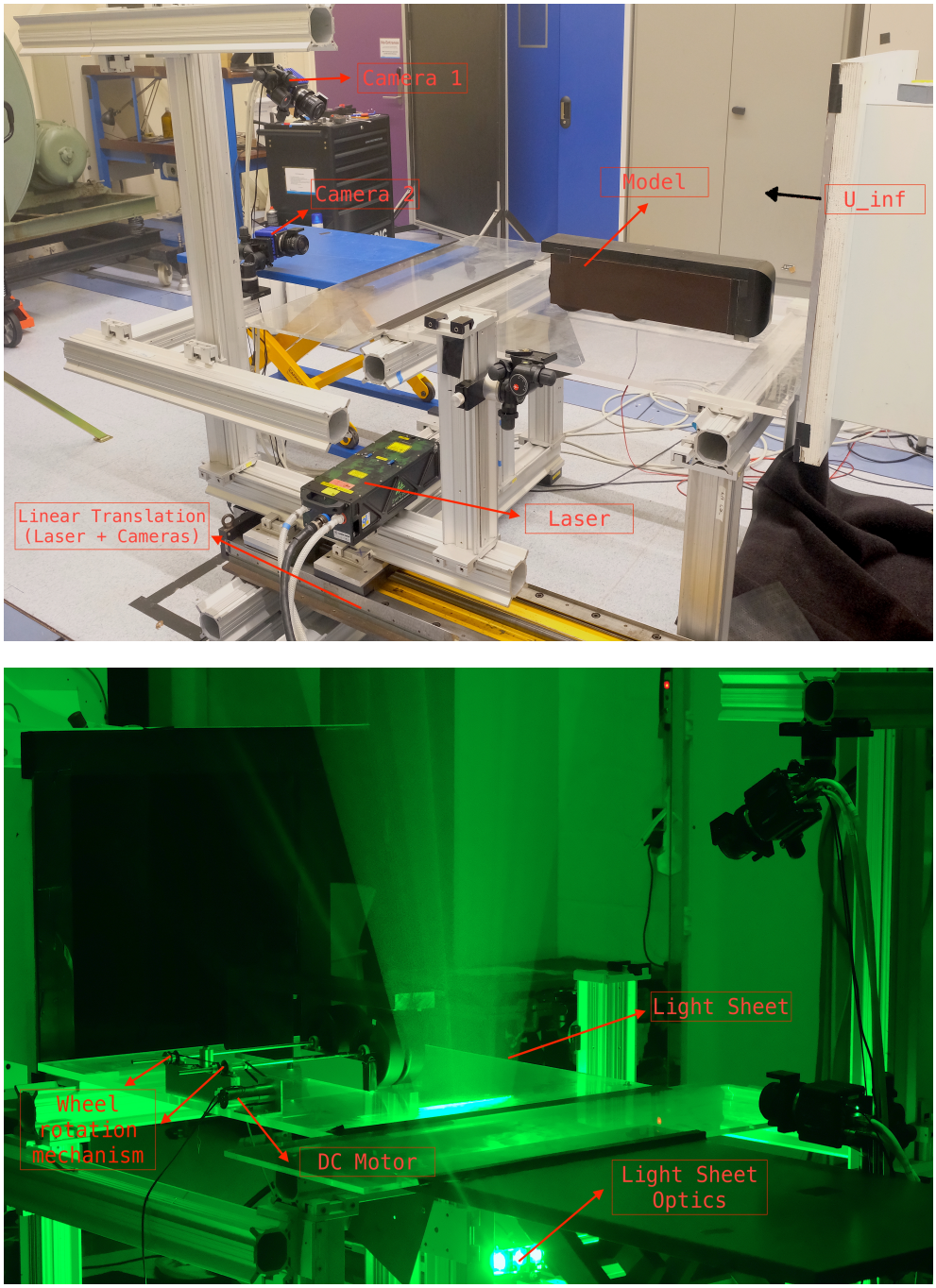

Figure 4.7: Experimental Setup

Hardware/Parameter	Plane A, B, C and D	Wake Plane
Seeding particles	Fog droplets ($d_p = 1\ \mu m$)	
Illumination	Nd:YAG, $2 \times 200\ mJ$, $15\ Hz$	
Recording device	*sCMOS* ($2560 \times 2160\ pixels^2$, 16 bits, $6.5\ \mu m$ pixel pitch)	
Recording frequency	$15\ Hz$	
Field of view	$225 \times 190\ mm^2$	$278 \times 235\ mm^2$
Recording lens and aperture	$50\ mm,\ f_\# = 11$	$35\ mm,\ f_\# = 11$
Optical magnification	0.073	0.059
Observation distance	$0.7\ m$	$0.6\ m$
Pulse delay	$33\ \mu s$	
No. of recordings	350	
Interrogation window	$4.2 \times 4.2\ mm^2$ ($48 \times 48\ px$) (75% overlap)	$5.2 \times 5.2\ mm^2$ ($48 \times 48\ px$) (75% overlap)
Vector pitch	$1.05\ mm$	$1.30\ mm$

Table 4.1: Description of parameters for the PIV measurements and processing

4.4 Drag Estimation

4.4.1 Freestream velocity corrections

In section 3.7 the equation for estimating the drag of a body using the control volume approach was derived. The equation reads as follows:

$$\overline{F_x} = \rho \iint_{downstream} (U_\infty - \overline{u})\overline{u}\ dydz - \rho \iint_{downstream} \overline{u'u'}\ dydz + \iint_{downstream} (p_\infty - \overline{p})\ dydz \tag{4.1}$$

The calculation of the first term in the above equation requires the velocity at two planes, one upstream (freestream conditions) and another downstream (in the wake) of the body. The value for the freestream velocity can be taken from the tunnel measurement system (using the pressure drop between the settling chamber and the nozzle) or a PIV measurement in the absence of the model. However, in an open-jet wind tunnel, the presence of a bluff object in the test section can create substantial distortions of the jet, leading to variations in the dynamic pressure and in turn the measured forces. Therefore, the freestream velocity measured without the bluff body needs to be corrected to a value seen by the model being tested. Mercker and Wiedemann were the first to account for the effects of solid wall boundaries at the nozzle and the collector on the dynamic pressure and derived corrections for the same (Mercker and Wiedemann 1996). They classified the effects into four categories: *Nozzle Blockage, Solid Blockage and Jet Expansion, Empty-Tunnel Pressure Gradients, and Collector Blockage Effects*. Out of these, nozzle blockage, and solid blockage and jet expansion are considered in this study to correct for the effect of the

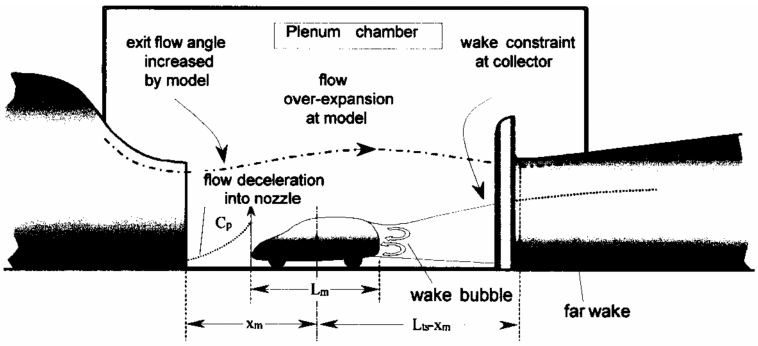

Figure 4.8: Schematic View of the Open-Jet Wind Tunnel (Credit: K. Cooper 1998)

bluff body on the freestream velocity. The correction for a pressure gradient in an empty wind tunnel (horizontal buoyancy) requires streamwise pressure gradients over the front and the rear halves of the model, which were not measured. Furthermore, the collector blockage effects can be neglected due to the configuration of the wind tunnel.

The correction factor for solid blockage and jet expansion accounts for the over-expansion of the free jet flow at the model, reducing the velocity at the model to a value below that measured for an empty tunnel. This correction is as given by equation 4.2. Here τ is the tunnel shape factor, with a value of -0.211 for a square tunnel cross section (Garner et al. 1996), V, L, and S are the model volume, model length and duplex model area respectively, and C_e is the effective nozzle area, given by equation 4.3, which includes the additional jet expansion effect due to proximity of the model to the nozzle.

$$\varepsilon_s = \tau \sqrt{\frac{V}{L}} \left(\frac{S}{C_e^{3/2}} \right) \tag{4.2}$$

$$C_e = \frac{C}{(1 + \varepsilon_{qn})} \tag{4.3}$$

Here ε_{qn} is the nozzle blockage factor given by equation 4.4 and C is the duplex nozzle exit area.

$$\varepsilon_{qn} = \frac{\frac{S}{2C}\left(1 + \frac{x_s}{\sqrt{x_s^2 + R_n^2}}\right)}{\left[1 - \frac{S}{2C}\left(1 + \frac{x_s}{\sqrt{x_s^2 + R_n^2}}\right)\right]} \tag{4.4}$$

$$where \quad x_s = -x_m + \left(\frac{L_m}{2}\right) - \left(\frac{S}{2\pi}\right)^{1/2} \quad and \; R_n = \sqrt{\frac{C}{\pi}}$$

In the equation for x_s (the distance from the point source to the nozzle), x_m (the distance from the centre of the model to the nozzle) is indicated in figure 4.8.

Nozzle blockage occurs due to the flow deceleration upstream of a bluff body getting extended into the nozzle, thereby producing a non-uniform velocity distribution at the nozzle exit, with the velocities

Parameter	Value	Parameter	Value
Model length L	$0.592\ m$	Tunnel shape factor τ	-0.211
Duplex model area S	$0.037\ m^2$	Nozzle blockage factor ε_{qn}	0.014
Model volume V	$0.011\ m^3$	Nozzle to source distance x_s	$-0.237\ m$
Duplex nozzle exit area C	$0.72\ m^2$	Effective nozzle area C_e	$0.709\ m^2$
Nozzle to model distance x_m	$0.456\ m$	Hydraulic diameter of duplex nozzle R_n	$0.479\ m$
Jet expansion correction factor ε_s	-0.0018	Nozzle blockage correction factor ε_n	0.0055

Table 4.2: Freestream velocity correction parameters

near the lower and central parts of the jet getting retarded while the velocities around the periphery get accelerated. The correction factor for nozzle blockage (ε_n) is as follows:

$$\varepsilon_n = \varepsilon_{qn}\left[\frac{R_n^3}{(x_m^2 + R_n^2)^{3/2}}\right]$$

The above corrections are combined as in equation 4.5 to calculate the corrected freestream velocity, as seen by the model, from the value measured on the measurement plane in the absence of the model. For the values of the various dimensional parameters in this study, the combined correction factor is 1.0037 (summarised in table 4.2).

$$\frac{U_{\infty,\,corrected}}{U_{\infty,\,measured}} = 1 + \varepsilon_n + \varepsilon_s \tag{4.5}$$

4.4.2 Reynolds stress term

The second term in equation 4.1 is the streamwise Reynolds normal stress term (R_{xx}), a result of time-averaging the non-linear instantaneous momentum equation. The term is calculated according to equation 4.6, where N is the number of uncorrelated samples.

$$R_{xx} = \frac{1}{N}\sum_{i=1}^{N} u_i' u_i' \tag{4.6}$$

4.4.3 Pressure reconstruction from PIV data

Finally, the third term in equation 4.1 requires the reconstruction of the pressure field in the measurement plane using the measured velocity data. This is done by solving the Poisson equation for pressure (detailed in section 3.8), with the appropriate boundary conditions. In a vector-matrix form, the Poisson equation can be written as $A\mathbf{p} = \mathbf{F}$, where A is a discrete representation of the Laplace operator, $\mathbf{p}$ is the vector of unknown pressure terms, and $\mathbf{F}$ is the source term. The value of the source term can be calculated from the divergence of the pressure gradients in equation 4.7. The RHS of equation 4.7 holds the time-averaged velocity fields, velocity gradients, and the gradients of the in-plane normal and shear

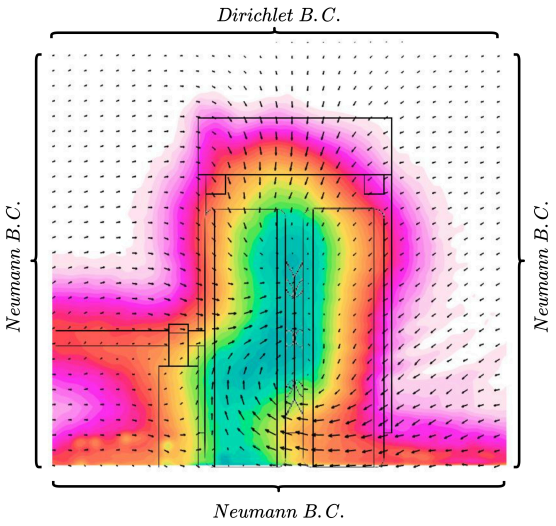

Figure 4.9: Boundary conditions imposed on the wake plane

Reynolds stresses, all of which are available from the PIV data. The gradients are calculated using a finite central difference scheme on the internal points and forward/backward differences at the boundary.

$$\frac{\partial \overline{p}}{\partial z} = -\rho\left\{\overline{w}\frac{\partial \overline{w}}{\partial z} + \overline{v}\frac{\partial \overline{w}}{\partial y} + \frac{\partial R_{zz}}{\partial z} + \frac{\partial R_{yz}}{\partial y}\right\} + \mu\left\{\frac{\partial^2 \overline{w}}{\partial z^2} + \frac{\partial^2 \overline{w}}{\partial y^2}\right\} \tag{4.7}$$
$$\frac{\partial \overline{p}}{\partial y} = -\rho\left\{\overline{w}\frac{\partial \overline{v}}{\partial z} + \overline{v}\frac{\partial \overline{v}}{\partial y} + \frac{\partial R_{yz}}{\partial z} + \frac{\partial R_{yy}}{\partial y}\right\} + \mu\left\{\frac{\partial^2 \overline{v}}{\partial z^2} + \frac{\partial^2 \overline{v}}{\partial y^2}\right\}$$

Regarding the boundary conditions (figure 4.9), for the top boundary, a Dirichlet boundary condition with $\overline{p} = p_\infty + 0.5\rho(U_\infty^2 - \overline{u}^2)$ is imposed and included directly in the source term. The other three boundaries are subject to Neumann boundary conditions, for which the pressure gradients are calculated as per equation 4.7. At the bottom boundary, which is bounded by a wall (ground plane), a further simplification is made (as a reasonable approximation) in the form of equation 4.8.

$$\left(\frac{\partial \overline{p}}{\partial z}\right)_{wall} = -\rho\left\{\overline{w}\frac{\partial \overline{w}}{\partial z} + \overline{v}\frac{\partial \overline{w}}{\partial y} + \frac{\partial R_{zz}}{\partial z} + \frac{\partial R_{yz}}{\partial y}\right\} + \mu\left\{\frac{\partial^2 \overline{w}}{\partial z^2} + \frac{\partial^2 \overline{w}}{\partial y^2}\right\} \approx 0 \tag{4.8}$$

4.5 Uncertainty in calculated drag

Uncertainty quantification is necessary to determine the interval that contains the measurement error. In this section, the expressions for the uncertainties of various derived quantities, including the quantities used in drag estimation as well as the drag itself, are formulated using linear uncertainty propagation as described in (Sciacchitano and Wieneke 2016).

For a derived quantity y, a function (F) of measured variables $x_{i=1\ to\ N}$, the uncertainty in y (U_y) can be expressed as:

$$U_y^2 = \sum_{i=1}^{N} \left(\frac{\partial F}{\partial x_i} \right)^2 U_{x_i}^2 + 2 \sum_{i=1}^{N-1} \sum_{j=i+1}^{N} \frac{\partial F}{\partial x_i} \frac{\partial F}{\partial x_j} \rho \left(\delta x_i, \delta x_j \right) U_{x_i} U_{x_j} \tag{4.9}$$

where $\rho \left(\delta x_i, \delta x_j \right)$ is the cross-correlation coefficient between the errors of x_i and x_j.

From the equation for estimating the drag of a body using the control volume approach (equation 4.1), it can be seen that the drag is a function of the mean streamwise velocity, the Reynolds normal stress in the streamwise direction and the mean pressure, i.e. $\overline{F_x} = F(\overline{u},\ \overline{u'u'},\ \overline{p})$.

Using the uncertainty propagation formula for the uncertainty in drag, assuming the correlation between the mean streamwise velocity, the Reynolds normal stress in the streamwise direction and the mean pressure to be zero, the following is obtained:

$$U_{\overline{F_x}}^2 = \left(\frac{\partial F}{\partial \overline{u}} \right)^2 U_{\overline{u}}^2 + \left(\frac{\partial F}{\partial \overline{u'u'}} \right)^2 \left(U_{\overline{u'u'}} \right)^2 + \left(\frac{\partial F}{\partial \overline{p}} \right)^2 U_{\overline{p}}^2 \tag{4.10}$$

which after substitution of the appropriate partial derivatives results in:

$$U_{\overline{F_x}}^2 = \left(\rho \iint\limits_{downstream} \left(U_\infty - 2\overline{u} \right) dydz \right)^2 U_{\overline{u}}^2 + \left(-\rho \iint\limits_{downstream} 1\ dydz \right)^2 \left(U_{\overline{u'u'}} \right)^2 \tag{4.11}$$

$$+ \left(\iint\limits_{downstream} -1\ dydz \right)^2 U_{\overline{p}}^2 \tag{4.12}$$

Equation 4.11 gives the expression for the uncertainty in the calculated drag based on the uncertainties of the mean streamwise velocity, the Reynolds normal stress in the streamwise direction, and the mean pressure, which are discussed next.

The uncertainty of the mean streamwise velocity, with N uncorrelated PIV samples, is given as:

$$U_{\bar{u}} = \frac{\sigma_u}{\sqrt{N}} \tag{4.13}$$

where σ_u is the standard deviation of the streamwise velocity, calculated directly from the PIV results as:

$$\sigma_u = \sqrt{\frac{1}{N-1} \sum_{i=1}^{N} \left(u_i - \bar{u} \right)^2} \tag{4.14}$$

The Reynolds normal stress in the streamwise direction is defined as the variance of the streamwise velocity (σ_u^2), therefore:

$$R_{xx} = \overline{u'u'} = \frac{1}{N-1}\sum_{i=1}^{N}(u_i - \bar{u})^2 \tag{4.15}$$

Using the definition for the uncertainty of variance, the uncertainty of the Reynolds normal stress in the streamwise direction ($U_{\overline{u'u'}}$) can be ascertained as:

$$U_{\overline{u'u'}} = \sigma_u^2\sqrt{\frac{2}{N-1}} \tag{4.16}$$

Finally, the uncertainty of the mean pressure ($U_{\bar{p}}$) is calculated by applying the linear uncertainty propagation formula to the Poisson's equation for pressure (equation 4.17) while neglecting any correlations between the terms.

$$\frac{\partial^2\bar{p}}{\partial y^2} + \frac{\partial^2\bar{p}}{\partial w^2} = -\rho\left\{\left(\frac{\partial\bar{v}}{\partial y}\right)^2 + \left(\frac{\partial\bar{w}}{\partial z}\right)^2 + 2\frac{\partial\bar{v}}{\partial z}\frac{\partial\bar{w}}{\partial y} + \frac{\partial^2\overline{v'^2}}{\partial y^2} + \frac{\partial^2\overline{w'^2}}{\partial z^2} + 2\frac{\partial^2\overline{v'w'}}{\partial y\partial z}\right\} \tag{4.17}$$

The result is:

$$\left(U_{\frac{\partial^2\bar{p}}{\partial y^2}}\right)^2 + \left(U_{\frac{\partial^2\bar{p}}{\partial w^2}}\right)^2 = \rho^2\left[\left(U_{\left(\frac{\partial\bar{v}}{\partial y}\right)^2}\right)^2 + \left(U_{\left(\frac{\partial\bar{w}}{\partial z}\right)^2}\right)^2 + \left(U_{2\frac{\partial\bar{v}}{\partial z}\frac{\partial\bar{w}}{\partial y}}\right)^2 + \left(U_{\frac{\partial^2\overline{v'^2}}{\partial y^2}}\right)^2 + \left(U_{\frac{\partial^2\overline{w'^2}}{\partial z^2}}\right)^2 + \left(U_{2\frac{\partial^2\overline{v'w'}}{\partial y\partial z}}\right)^2\right]$$

To calculate the uncertainties of the various terms in the above equation, the uncertainty propogation formula is applied to the central finite difference approximation of each of the terms individually, with the following assumptions:

1. The uncertainty for mean velocity, Reynolds normal stress, and Reynolds shear stress components is uniform throughout the grid.
2. Errors of $\overline{v}$ and $\overline{w}$ at the same or neighbouring spatial locations are uncorrelated.
3. Errors of the same velocity component at different spatial points are uncorrelated

The resulting uncertainty for the mean pressure ($U_{\overline{p}}$) can be expressed as:

$$
\begin{aligned}
U_{\overline{p}} = \rho \left[\frac{1}{(\Delta y)^4} + \frac{1}{(\Delta z)^4} \right]^{\frac{-1}{2}} \Bigg\{ & \frac{1}{3(\Delta y)^2} \left[\left(\frac{\partial \bar{v}}{\partial y} \right)^2 U_{\overline{v}}^2 + \left(\frac{\partial \bar{v}}{\partial z} \right)^2 U_{\overline{w}}^2 \right] \\
& + \frac{1}{3(\Delta w)^2} \left[\left(\frac{\partial \bar{w}}{\partial z} \right)^2 U_{\overline{w}}^2 + \left(\frac{\partial \bar{w}}{\partial y} \right)^2 U_{\overline{v}}^2 \right] \\
& + \frac{1}{(\Delta y)^4} U_{\overline{v'v'}}^2 + \frac{1}{(\Delta w)^4} U_{\overline{w'w'}}^2 + \frac{1}{6(\Delta y \Delta z)^2} U_{\overline{v'w'}}^2 \Bigg\}^{\frac{1}{2}}
\end{aligned}
\tag{4.18}
$$

Chapter 5

Results and Discussion

The current chapter discusses the results obtained during the experimental campaign. Section 5.1 includes a discussion and analysis of the flowfield on the wake plane, within which the discussion is segregated into the effect of wheel rotation (sub-section 5.1.1), effect of the side skirt (sub-section 5.1.2), and the effect of wheel covers (sub-section 5.1.3). Following this, section 5.2 presents the drag values as determined from the velocity data on the wake plane. Section 5.3 addresses the effect of wheel rotation, side-skirt, and wheel covers on the velocity field results obtained on the planes beside the wheels (plane A and C as per figure 4.6). Finally, section 5.4 discusses the results for the wheel covers with openings varying in coverage area and radial position.

5.1 Near wake flow topology

This section discusses the results in the wake plane, highlighting the effects of wheel rotation, skirts (long and short), and wheel covers on the mean streamwise velocity and turbulent kinetic energy.

To begin with, the streamwise velocity contours are presented for the baseline case of the model without a skirt or wheel covers. Following this, line plots are presented showing either the vertical or the horizontal variation of a velocity component or the turbulent kinetic energy, averaged over certain regions of the wake plane, such that some of the basic features of the flow, for all of the tested configurations, can be established. Finally, contours plots are presented for particular configurations, other than the baseline, that are of interest.

Figure 5.1 shows the streamwise mean velocity contours and the in-plane velocity vectors for the baseline configuration (*No Skirt-No Cover*), with both stationary and rotating wheels. The streamwise velocity is non-dimensionalized by the freestream velocity, the vertical distance by the wheel diameter (D), and the horizontal distance by the wheel width (W).

Apparent is the asymmetry in the wake, resulting in part from the rotating mechanism on the left when looking from behind (bearing block and shaft) and partly due to the asymmetric change in the configurations (skirts and wheel covers are fitted only to the right side of the model when looking from behind).

Moving on, the horizontal and vertical extension of the central region of the wake, with normalized velocity of approximately $\frac{u}{U_\infty} \leq 0.4$, is seen to be a strongly dependent on rotation (and configuration changes in general, discussed in detail later). The region surrounding this $\left(0.4 \leq \frac{u}{U_\infty} \leq 0.95\right)$, maintains a very similar vertical extension (approximately to the top of the body) regardless of the configuration but varies greatly in the horizontal extension across configurations.

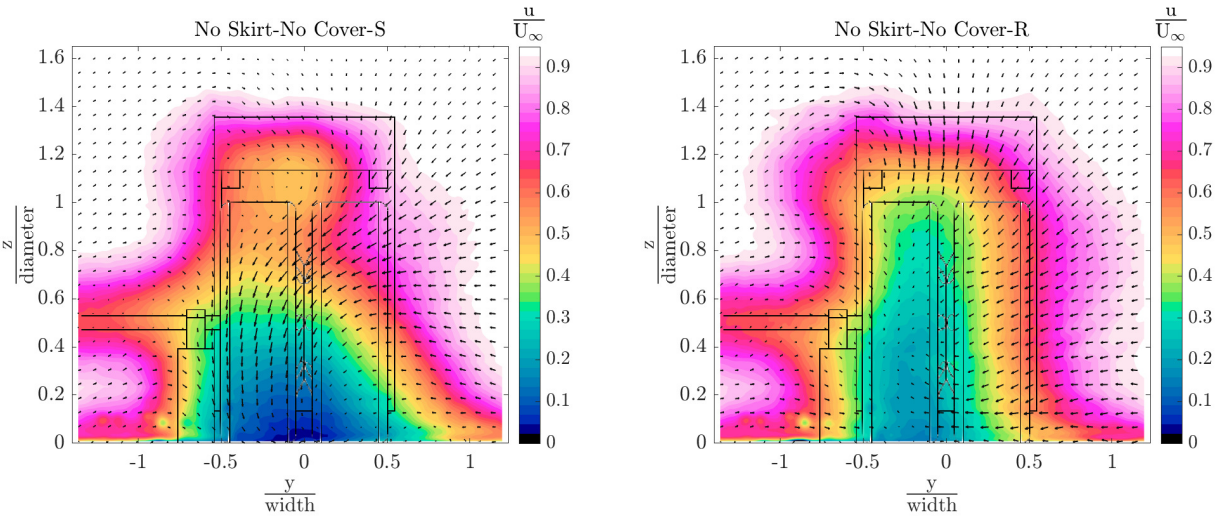

(a) Stationary wheel

(b) Rotating wheel

Figure 5.1: Streamwise mean velocity contours and in-plane velocity vectors for the baseline configuration (*No Skirt-No Cover*), stationary (left) and rotating (right)

Looking at the in-plane velocity vectors, the stationary case shows a strong asymmetric downwash in the region below the top of the projected wheel profile $\left(\frac{z}{D} \leq 1\right)$, which is missing in the rotating wheel. On the other hand, the rotating case shows a distinct downwash behind the projected body $\left(1.15 \leq \frac{z}{D} \leq 1.35\right)$, which is not seen in the stationary case.

Figure 5.2 shows the contours of the turbulent kinetic energy (TKE) for the baseline case of *No Skirt-No Cover* with both stationary and rotating wheels. As can be seen, the TKE is significantly higher for the rotating wheel, especially in the region of the projected wheel. This trend is seen with the other configurations as well (discussed further in sub-section 5.1.1). Furthermore, within the wheel projection, the majority of the difference in TKE due to rotation is in the region comprising the top half of the wheel. This is expected considering the earlier separation for rotating wheels and the subsequent higher fluctuations in the shear layer and recirculating region. Besides rotation, the presence or absence of wheel covers also has a significant effect on the TKE in the wake plane, with configurations including covers showing overall lower values for the turbulent kinetic energy, which then also has an impact on the contribution to drag for the Reynolds stress term. Short skirts (that do not cover the wheels) have a relatively smaller impact on the TKE, suggesting that it is really the rotation of the wheels themselves and devices that close or cover them (like wheel covers or long skirts) that have a major effect on the magnitude of velocity fluctuations.

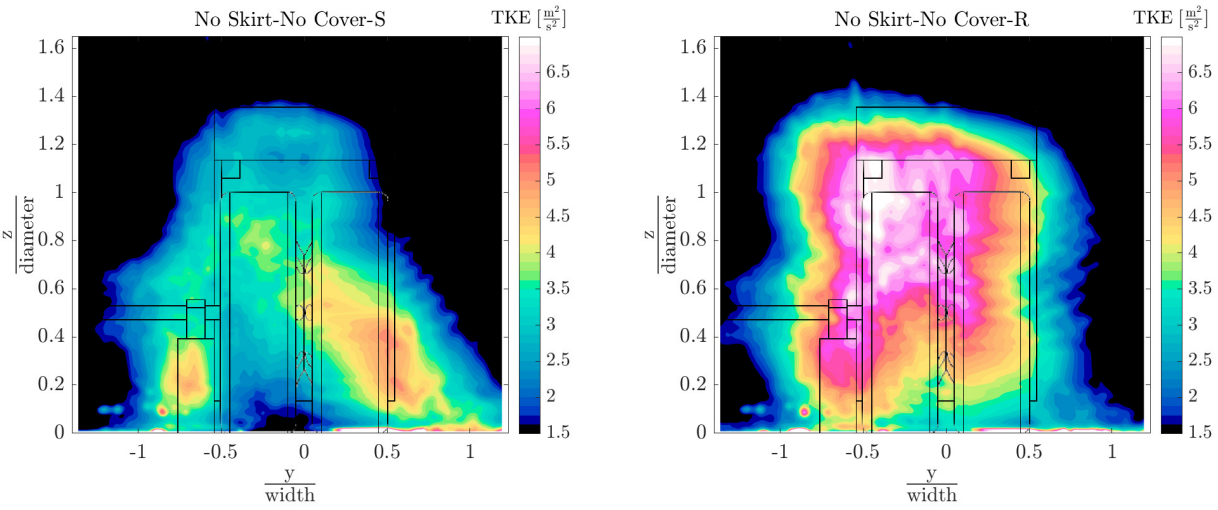

(a) Stationary wheel

(b) Rotating wheel

Figure 5.2: Turbulent kinetic energy contours for the baseline configuration (*No Skirt-No Cover*), stationary (left) and rotating (right)

5.1.1 Effect of wheel rotation

Figure 5.3 shows the vertical variation of the normalized streamwise velocity averaged over the width of the wheel ($-0.5 \leq \frac{y}{W} \leq 0.5$). Most notable here is the distinct difference between the rotating and stationary wheel. The effect of wheel rotation on the velocity starts to be seen in the gap between the wheel and the body and continues downwards till the ground plane $\left(0 \leq \frac{z}{D} \leq 1.2\right)$. In the upper region of the projected wheel $\left(0.5 \leq \frac{z}{D} \leq 1\right)$, the rotating configurations show a significantly higher velocity deficit compared to their stationary counterparts. This is expected considering that for a rotating wheel the flow separates near the top of the wheel, whereas for a stationary wheel the separation point is more aft in the angular sense (see for example figure 2.3, adapted from the results of Fackrell (1974)). In the lower region $\left(0 \leq \frac{z}{D} \leq 0.5\right)$, the streamwise velocity deficit is greater for the stationary wheel as compared to the rotating wheel regardless of the configuration. The peak velocity deficit overall is also greater for the stationary wheel for any given configuration.

The difference in the separation point also has a large effect on the downwash in the wake plane, elaborated upon using the results in figure 5.4, wherein the variation of the normalized vertical velocity component along the z axis, averaged over the wheel width, is shown. Two distinct vertical regions can be distinguished, the first above the projected top surface of the wheel $\left(\frac{z}{D} \geq 1\right)$ where the downwash is greater for the rotating wheel, and the second below the top surface of the wheel where the downwash is greater for the stationary wheel. In the upper region, the greater downwash for the rotating wheel can be understood to be an effect of the taller wake and the resulting entrainment of the higher momentum flow above the body into the wake. On the other hand, the greater downwash for the stationary wheel in the lower region is a result of the flow remaining attached for longer over the top surface of the wheel.

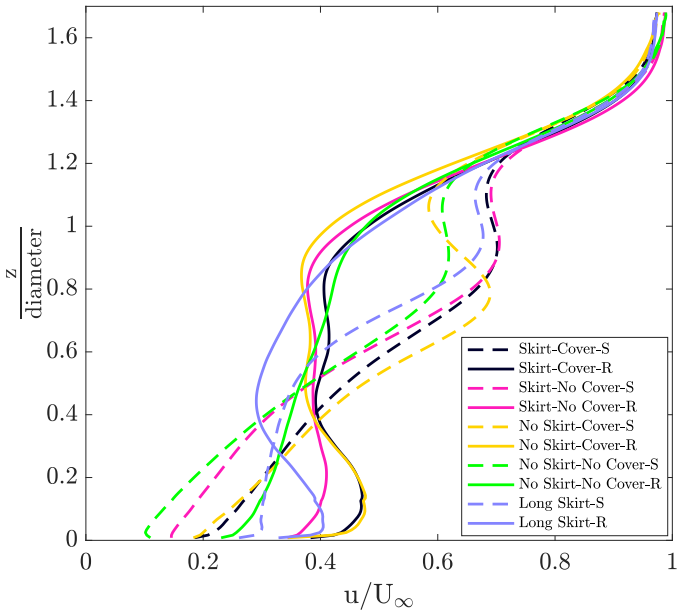

Figure 5.3: Vertical variation (along z axis) of $\frac{u}{U_\infty}$ in the wake plane, averaged over the width of the wheel $\left(-0.5 \leq \frac{y}{\text{width}} \leq 0.5\right)$

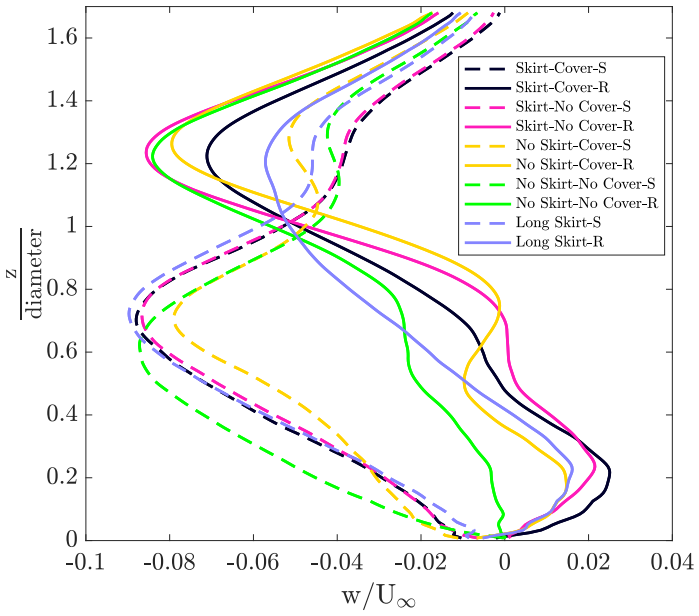

Figure 5.4: Vertical variation (along z axis) of $\frac{w}{U_\infty}$ in the wake plane, averaged over the width of the wheel $\left(-0.5 \leq \frac{y}{\text{width}} \leq 0.5\right)$

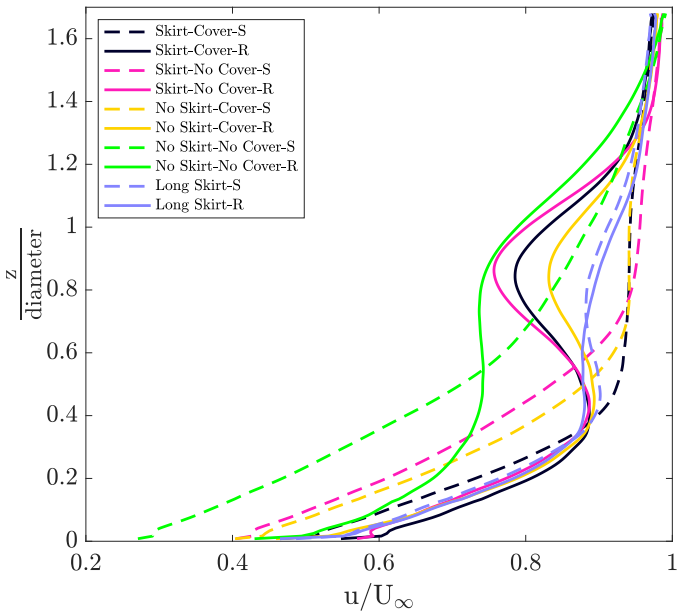

Figure 5.5: Vertical variation (along z axis) of $\frac{u}{U_\infty}$ in the wake plane, averaged over the region spanning $\left(0.5 \leq \frac{y}{\text{width}} \leq 0.75\right)$

Figure 5.5 shows the variation of the normalized streamwise velocity along the z axis, averaged over a horizontal region beside the wheel, spanning $0.5 \leq \frac{y}{W} \leq 0.75$. In the lower half of the wheel $\left(\frac{z}{D} \leq 0.5\right)$, the velocity deficit for the stationary wheel is higher for any given configuration. Also, for the stationary case, the increase in velocity deficit with decreasing z coordinate is more or less monotonic. In contrast to this, the rotating configurations (with the exception of the configuration *No Skirt-No Cover-R*), show a localized peak in the velocity deficit around $\frac{z}{D} = 0.9$. This corresponds with the upper lobe of reduced velocities observed near the top edge of the wheel $\left(\frac{z}{D} = 1\right)$ in the case of rotating wheels, as can be seen for example in figure 5.6, which shows the streamwise velocity contours for the case *Skirt-Cover-S* and *Skirt-Cover-R*. The resulting profile is 'S' shaped, showing an increase in velocity in the lower half of the wheel, although the point of inflection varies (only slightly) in its z coordinate based on the configuration. An exception to this difference between rotating and stationary wheels is the configuration with the long skirt, which has a very similar velocity profile for both the rotating and stationary wheels, as could be expected considering it covers the entire length of the model, and therefore, both the wheels completely.

Next, looking at figure 5.7, showing the horizontal variation of the normalized streamwise velocity averaged over the region spanning the ground to the top of the model $\left(0 \leq \frac{z}{D} \leq 1.35\right)$, the effect of rotation is seen to be limited to resulting in a greater streamwise velocity deficit for a given configuration. Also of note is that while rotation resulted in a taller wake, it does not, on average, affect the width of the wake.

Finally, the effect of wheel rotation on the velocity fluctuations is seen in figure 5.8, which plots the horizontal variation of the turbulent kinetic energy (TKE), averaged over the height of the model $\left(0 \leq \frac{z}{D} \leq 1.35\right)$, for both rotating and stationary wheels. The rotating wheels result in a significantly higher TKE in the

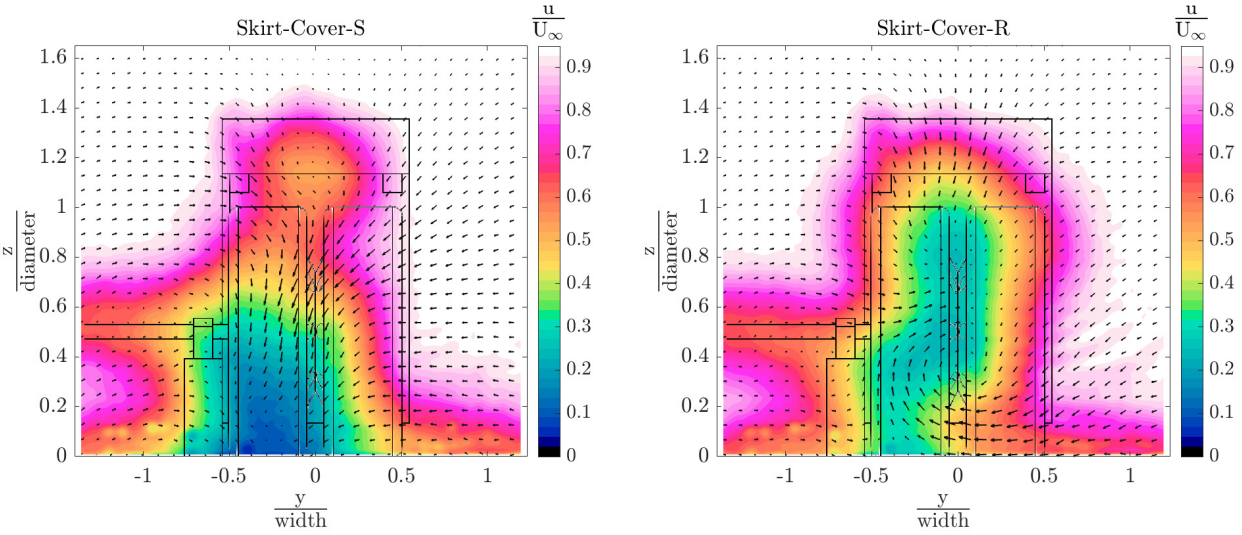

(a) Stationary (b) Rotating

Figure 5.6: Streamwise mean velocity contours for the configuration with skirt and wheel cover, both stationary (left) and rotating (right)

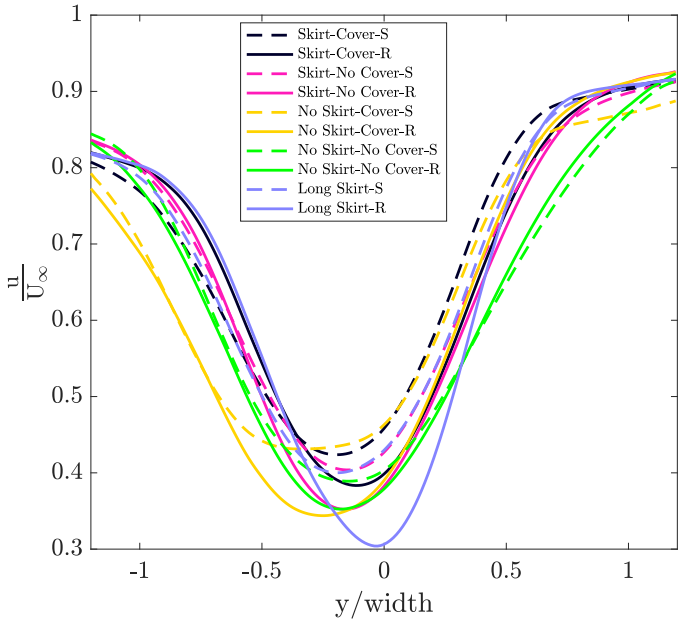

Figure 5.7: Horizontal variation (along y axis) of $\frac{u}{U_\infty}$ in the wake plane, averaged over the region spanning $\left(0 \leq \frac{z}{\text{diameter}} \leq 1.35\right)$

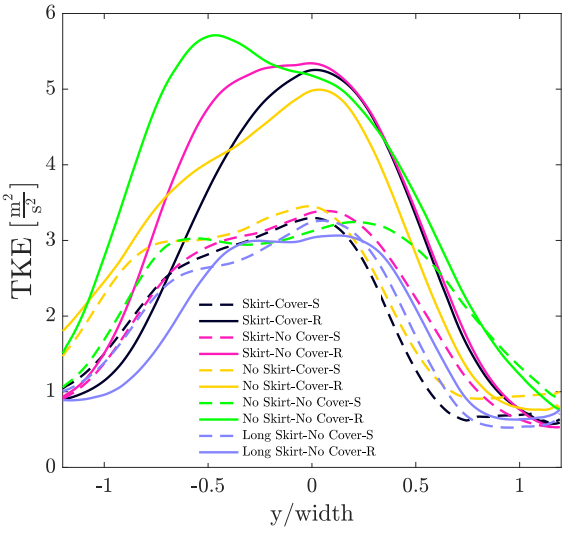

Figure 5.8: Horizontal variation of turbulent kinetic energy, averaged over the height of the model $\left(0 \leq \frac{z}{\text{diameter}} \leq 1.35\right)$, for both rotating and stationary wheels

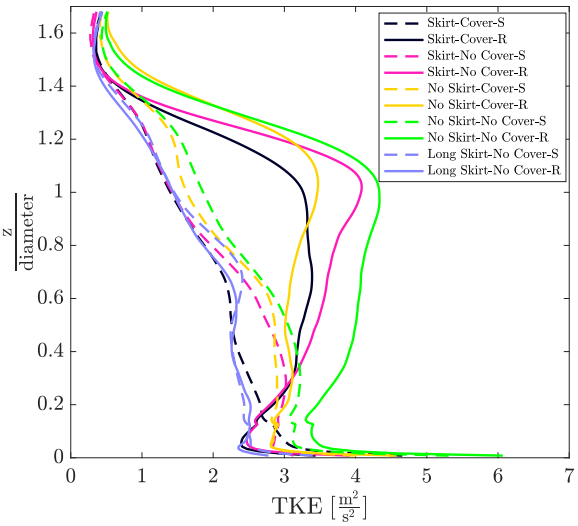

Figure 5.9: Vertical variation of turbulent kinetic energy, averaged over the width of the wake plane $\left(-1.2 \leq \frac{y}{\text{width}} \leq 1.2\right)$, for both rotating and stationary wheels

wake, especially in the region spanning the width of the projected wheel. An exception here is the configuration with the long skirt, which shows very identical levels between the rotating and stationary case, indicating again to the isolating nature of the long skirt with respect to wheel rotation. The higher levels of turbulent kinetic energy for the rotating wheel correspond with the earlier separation of the flow over the wheel and the resulting recirculation region and mixing layer. Figure 5.9, which plots the vertical variation of the TKE, shows the difference to exist primarily in the upper half of the projected wheel, which is in line with the expectation.

5.1.2 Effect of skirt

The effect of skirts on the flow in the wake plane is evident in the magnitude of the streamwise velocity deficit, the width of the wake, and the degree of asymmetry of the wake.

Referring figure 5.10 which plots the vertical variation of the normalized streamwise velocity, averaged over the width of the wake plane for the rotating wheel, and comparing configuration *Skirt-Cover-R* with *No Skirt-Cover-R* , it can be seen that the velocity deficit for the case without the skirt is higher in the upper region of the projected wheel up to about $\frac{z}{D} = 0.4$, after which the velocity profiles nearly overlap. A similar comparison can be made between the configurations *Skirt-No Cover-R* and *No Skirt-No Cover-R*, though in this case the configuration without the skirt shows a greater velocity deficit for nearly the entire height of the wake plane. Finally, comparing the configuration *Long Skirt-R* with the baseline case of *No Skirt-No Cover-R* again shows the significantly lower velocity deficit for the former. The quantification of these differences is seen in detail in the next section when comparing the drag

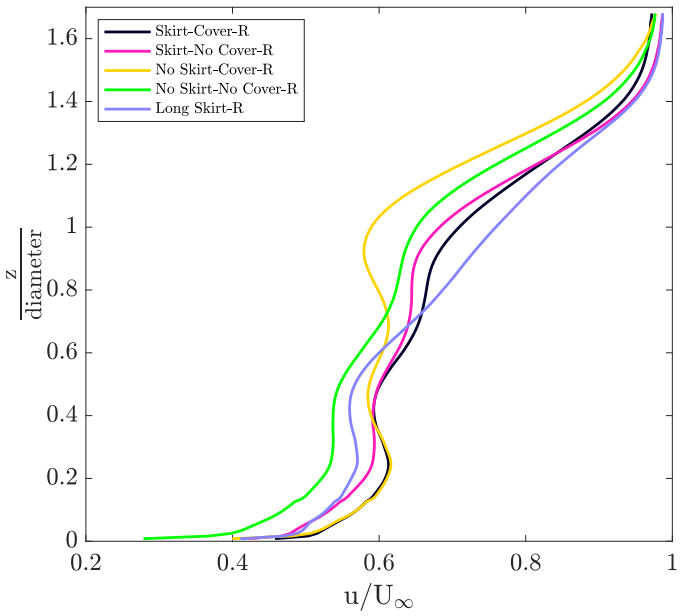

Figure 5.10: Vertical variation (along z axis) of $\frac{u}{U_\infty}$ in the wake plane, averaged over the width of the wake plane $\left(-1.2 \leq \frac{y}{\text{width}} \leq 1.2\right)$

values calculated with the velocity data in the wake plane.

Moving on, figure 5.11 shows the horizontal variation of the normalized streamwise velocity, averaged over the height of the model, for the rotating wheel. Here the difference in the wake width and the asymmetry are highlighted. Once again, comparing either configurations *Skirt-Cover-R* and *No Skirt-Cover-R* or configurations *Skirt-No Cover-R* and *No Skirt-No Cover-R*, in each case, the wake for the configuration without the skirt is wider to the left and therefore more asymmetric, indicating a level of crossflow (referring to the flow in the horizontal direction into the model) through the model, especially for the configuration *No Skirt-Cover-R*, which shows the most asymmetric wake. The streamwise velocity contours for this configuration, along with the corresponding configuration with the skirt fitted, are shown in figure 5.12 to further illustrate the difference. As can be seen, the difference is primarily in the upper region of the model, $0.8 \leq \frac{z}{D} \leq 1.35$, as can be expected based on the geometry of the skirt. The higher degree of crossflow is seen more clearly in the velocity data on planes A and C, discussed later in section 5.3.

Figure 5.13, which shows the horizontal variation of the vertical velocity component (downwash) for the stationary wheel, averaged over the upper half of the projected wheel $\left(0.5 \leq \frac{z}{D} \leq 1\right)$, further highlights the asymmetry caused by removing the skirt. Of interest here is the horizontal region $-0.5 \leq \frac{y}{W} \leq 0.5$, which is the width of the projected wheel. The downwash for the configuration *Long Skirt-S* is nearly symmetrical. For the configurations with the short skirt, the peak of the downwash shifts slightly to the left. Finally, for the configurations without skirts, the shift is even more. Also of note here is the decreasing negative peak of the downwash with the subsequent move from a long skirt to a short skirt and finally no skirt. This reduction, at least in part, could be hypothesized as a result of an earlier

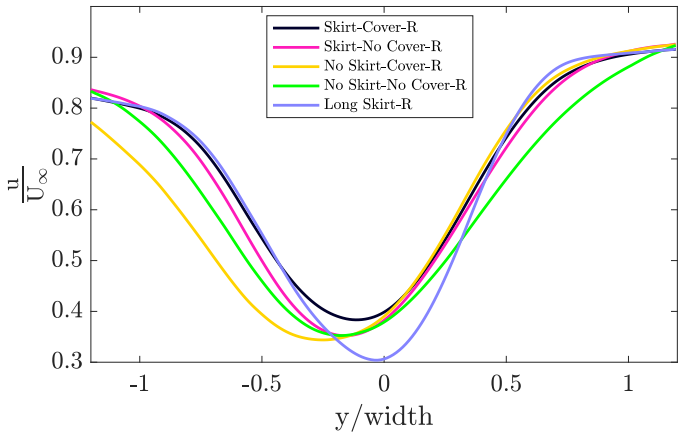

Figure 5.11: Horizontal variation of the normalized streamwise velocity, averaged over the height of the model $\left(0 \leq \frac{z}{\text{diameter}} \leq 1.35\right)$

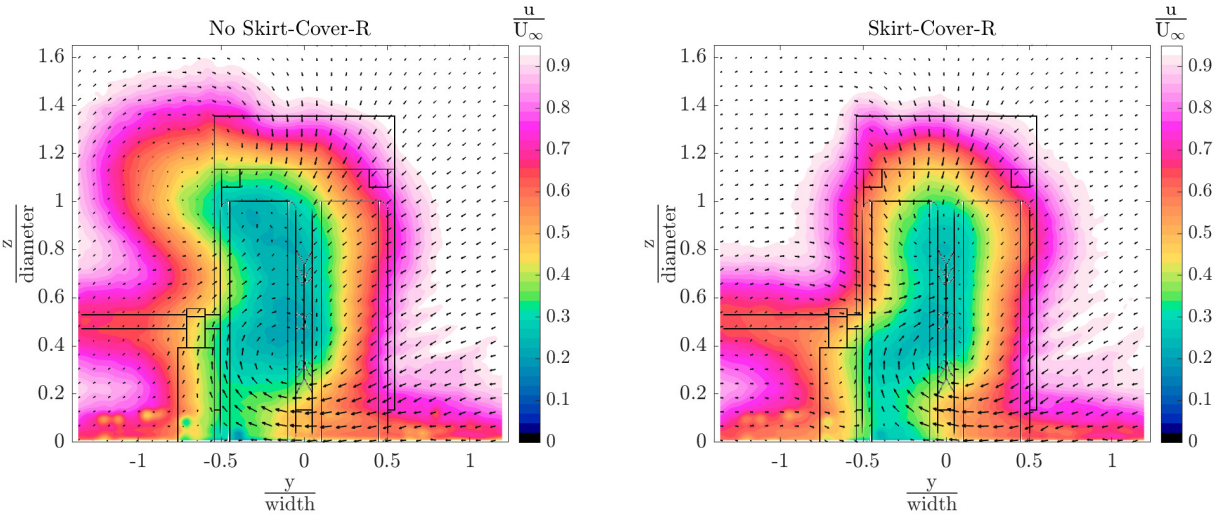

(a) *No Skirt-Cover-R* (b) *Skirt-Cover-R*

Figure 5.12: Comparison of the normalized streamwise velocity contours for configurations *No Skirt-Cover-R* and *Skirt-Cover-R*

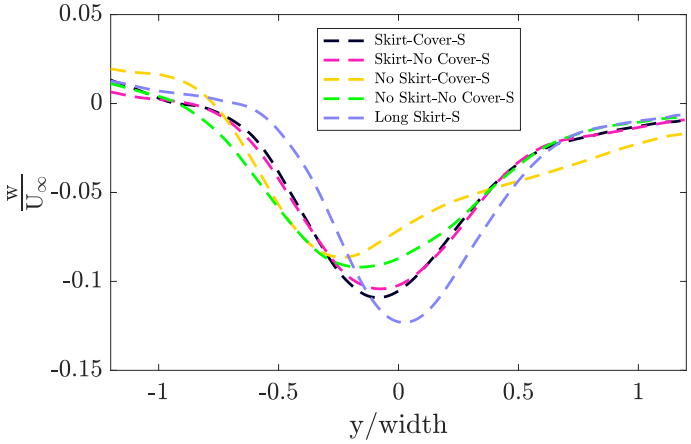

Figure 5.13: Horizontal variation of the normalized vertical velocity component (w/U_∞), averaged over the upper half of projected the wheel $\left(0.5 \leq \frac{\text{z}}{\text{diameter}} \leq 1\right)$

separation of the flow on top of the wheel, although the current data is insufficient to conclude this.

5.1.3 Effect of wheel covers

Figure 5.14 compares the streamwise velocity contours for the configurations *Skirt-Cover-R* and *Skirt-No Cover-R*. The wake in the upper half of the projected wheel is wider for the configuration without the wheel cover. Besides the overall width, without the wheel cover, the central region of the wake, roughly demarcated by $u/U_\infty \leq 0.4$, is both wider and has a greater velocity deficit, especially in the lower half (can also be seen in the line plot of figure 5.3). A difference is also seen in the downwash in the region behind the projected body $\left(1 \leq \frac{\text{z}}{\text{D}} \leq 1.35\right)$, a characteristic of cases with rotating wheels, being higher for the case without the wheel cover. This is visible as longer vector arrows in figure 5.14 or as line a line plot in figure 5.4.

In the region beside the wheel, while the general variation of velocity with height is a stronger function of rotation, the presence or absence of a wheel cover does affect the extent of the velocity deficit. In figure 5.15a the vertical variation of the normalized streamwise velocity in the region beside the skirt is plotted for the stationary wheel. For a given pair of configurations, all else being equal, the configuration without the wheel cover shows a higher velocity deficit. Looking at the same region but for rotating wheels, a higher velocity deficit without wheel covers is seen in the upper region, with the deficit peak at around $\frac{\text{z}}{\text{D}} = 0.9$ being greater without covers. The significant difference between configurations *No Skirt-Cover-R* and *No Skirt-No Cover-R* is a result of the greater leftward shift of the wake for the former configuration. This is more clear in the contour plots for the velocity, shown in figure 5.16.

Looking at the turbulent kinetic energy in the wake plane, referring to figure 5.9 from sub-section 5.1.1, the configurations without the wheel covers have significantly greater velocity fluctuations, especially for the rotating wheel. Figure 5.17 shows this difference for the configurations *Skirt-Cover-R* and *Skirt-No Cover-R*. This corresponds with the higher downwash seen earlier, pointing to the entrainment of

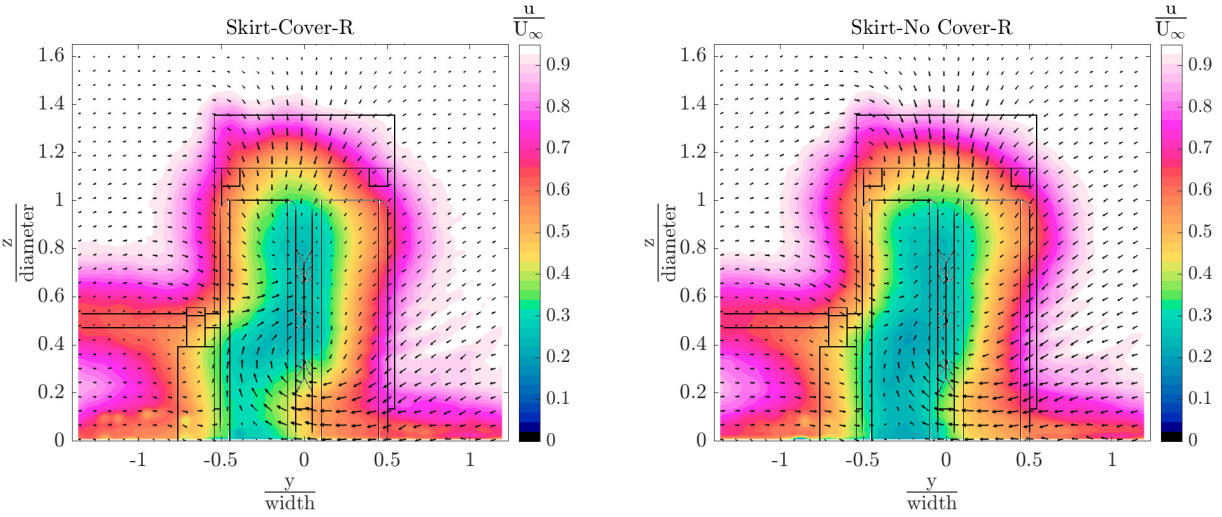

(a) *Skirt-Cover-R* (b) *Skirt-No Cover-R*

Figure 5.14: Comparison of the normalized streamwise velocity contours for configurations *Skirt-Cover-R* and *Skirt-No Cover-R*

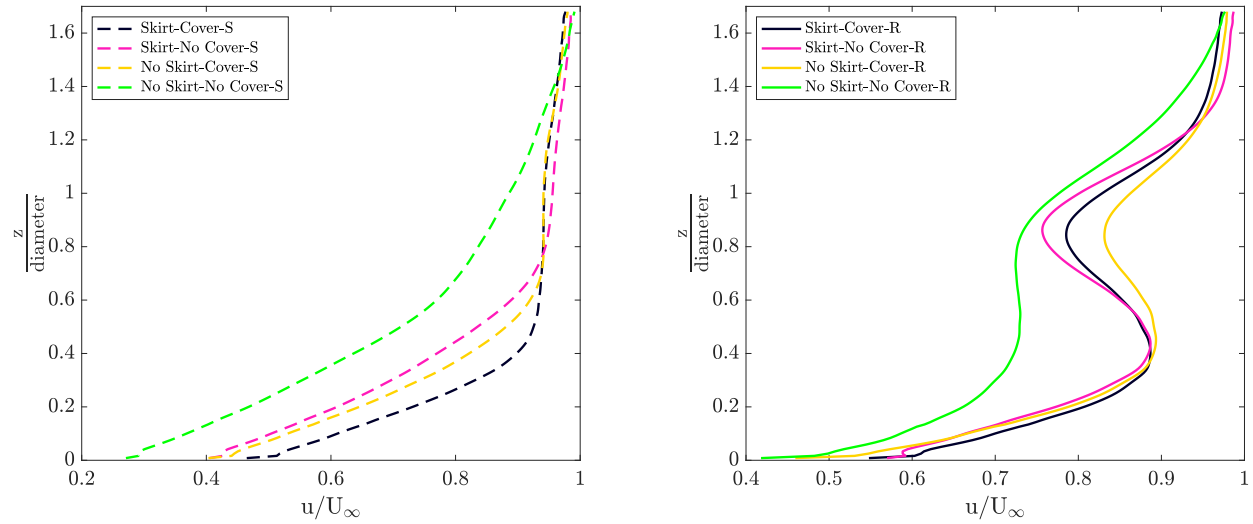

(a) Stationary wheel (b) Rotating wheel

Figure 5.15: Vertical variation (along z axis) of $\frac{u}{U_\infty}$ in the wake plane, averaged over the region spanning $\left(0.5 \leq \frac{y}{width} \leq 0.75\right)$

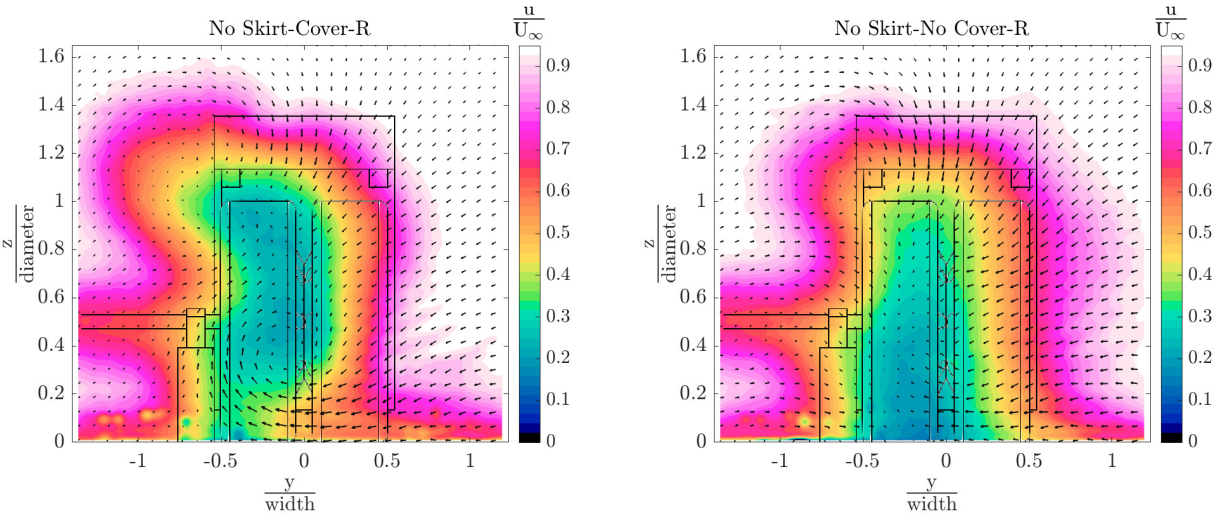

(a) *No Skirt-Cover-R* (b) *No Skirt-No Cover-R*

Figure 5.16: Comparison of the normalized streamwise velocity contours for configurations *No Skirt-Cover-R* and *No Skirt-No Cover-R*

the higher momentum flow above the body into the wake on account of the greater mixing. In essence, the effects of rotation seem to be amplified in the absence of wheel covers, which also reflects in the calculated drag values (discussed in section 5.2), which show a greater difference between the rotating and stationary cases in the absence of wheel covers.

5.2 Drag

5.2.1 Summary of the results

The following section summarizes the drag values derived from the velocity field measured in the wake, using the control volume approach, for each of the tested configurations.

Figure 5.18 shows these values along with the 95% confidence intervals (calculated using the uncertainty derived based on the formulation in section 4.5). As can be seen, for all of the configurations, there is a systematic trend of the rotating wheel producing the higher drag, except for the configuration with the long skirt where the drag is nearly the same. This is opposed to the results for an isolated wheel in contact with a moving ground plane, wherein the rotating wheel has been shown to produce lower drag than a stationary wheel. However, for the case where the wheel is located at a certain gap to a stationary ground plane to allow for rotation, specifically referring to a gap to diameter ratio of about 0.015, as is the case in this study, the results from (Stapleford and G. W. Carr 1970) show the drag of the stationary and rotating wheels to be very similar, with the rotating wheels perhaps showing a slightly higher drag (see figure 2.12; exact comparison is not possible due to the limited number of gap to diameter values reported in the study).

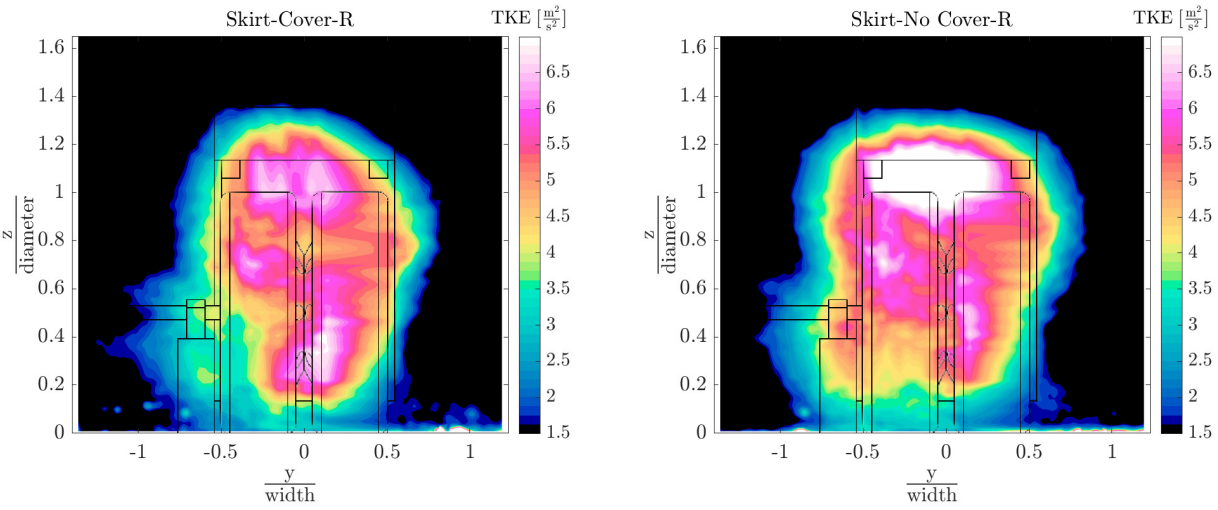

(a) *Skirt-Cover-R* (b) *Skirt-No Cover-R*

Figure 5.17: Comparison of the turbulent kinetic energy contours for configurations *Skirt-Cover-R* and *Skirt-No Cover-R*

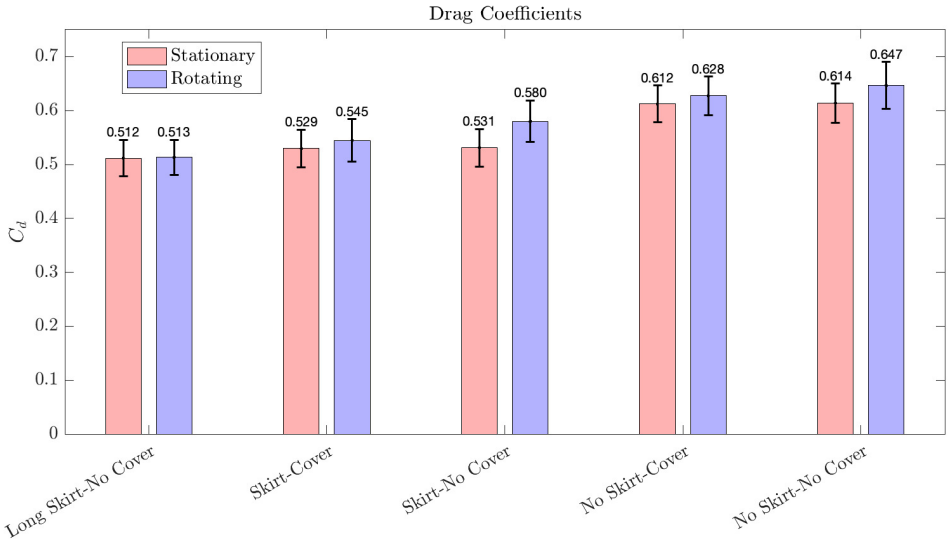

Figure 5.18: Coefficient of drag for the various configurations, calculated from the velocity data in the wake plane, shown along with 95% confidence intervals

Configuration	ΔCd (%) - Rotating Wheel	ΔCd (%) - Stationary Wheel
Baseline (*No Skirt-No Cover*)	0	0
Baseline + short skirt	-10.3	-13.4
Baseline + wheel cover	-3	-0.2
Baseline + short skirt + wheel cover	-15.8	-13.7
Baseline + long skirt	-20.6	-16.6

Table 5.1: ΔCd (%) with respect to the baseline case (*No Skirt-No Cover*) for both the rotating and stationary wheels. Marked in red are the changes with respect to baseline which do not show a statistically significant difference

Moving on to the individual configurations, the baseline case (*No Skirt-No Cover*) produces the highest drag among all the configurations, for both the stationary wheel ($C_d = 0.614$) and the rotating wheel ($C_d = 0.647$). Table 5.1 summarizes the percentage change in the drag values for the rest of the configurations compared to the baseline. The long skirt is the most effective amongst the tested devices, more so for the rotating wheel ($\Delta C_d = -20.6\%$) than the stationary one ($\Delta C_d = -16.6\%$). The short skirt by comparison, as expected, is less effective in general. More interestingly, as opposed to the long skirt, the short skirt is more effective for the stationary wheel as compared to the rotating wheel.

For the case of the baseline with the wheel covers, the opposite trend is seen, wherein the covers are more effective in reducing the drag of rotating wheels ($\Delta C_d = -3\%$) as compared to stationary ones ($\Delta C_d = -0.2\%$). This trend continues when both the short skirt and the wheel covers are fitted onto the baseline, where the drag delta for the rotating wheel is higher at $\Delta C_d = -15.8\%$, compared to the delta for the stationary wheel ($\Delta C_d = -13.7\%$). In fact, for the stationary wheel, the gain due to both the short skirt and the wheel covers is nearly the same as the algebraic sum of the drag benefit due to the individual devices in isolation, whereas, for the rotating wheels, the drag benefit of the combination is greater than the sum of the individual devices. Overall, the results suggest that for a device that covers the wheels (wheel covers or long skirt), wheel rotation has a substantial effect on the measured benefit in drag.

5.2.2 Momentum term, Pressure term, and Reynolds Stress term: Contribution to C_d and uncertainty in measurement

From equation 3.20 it is seen that when using a control volume approach, the calculated drag of a body is the combination of 3 terms on the right-hand side. Table 5.2 gives the contribution of these individual terms, as well as the uncertainty of each, for the reference case of the model without a skirt and wheel covers.

As can be seen, the pressure and Reynolds stress terms contribute in the range of 9% to 13% of the total drag and cancel each other out almost entirely, leaving the momentum term as the (almost) sole con-

	Rotating Wheel			
	Contribution to C_d	% of drag	Uncertainty	$\frac{\text{Uncertainty}}{\text{Contribution to C}_\text{d}} \times 100$
Momentum term	0.6619	102.35	0.0198	2.99
Pressure term	0.0695	10.74	0.0047	6.76
Reynolds stress term	-0.0848	-13.11	0.0080	9.43
Total drag coefficient	0.6467	100	0.0221	3.41

	Stationary Wheel			
	Contribution to C_d	% of drag	Uncertainty	$\frac{\text{Uncertainty}}{\text{Contribution to C}_\text{d}} \times 100$
Momentum term	0.6090	99.21	0.0173	2.84
Pressure term	0.0609	9.92	0.0032	5.25
Reynolds stress term	-0.0562	-9.15	0.0052	9.25
Total drag coefficient	0.6138	100	0.0185	3.01

Table 5.2: Contribution of the individuals terms to the total drag coefficient along with their respective uncertainties for the baseline case of *No Skirt-No Cover,* both stationary and rotating

tributor to the total drag. Based on existing literature on the estimation of drag using a control volume approach (Terra, Sciacchitano, and Scarano 2016), at the streamwise distance behind the model where this particular measurement was made $\left(\frac{\text{x}}{\text{Model width}} = 1.9\right)$ this is the expected behavior, wherein the pressure term provides a small positive contribution, the Reynolds stress term a small negative contribution and most of the net total drag comes from the momentum term.

Moving to the uncertainties of the individual terms and looking at the ratio of the uncertainty to the mean value as a percentage, the momentum term has the lowest ratio (about 3%), whereas the pressure term and the Reynolds stress terms have higher uncertainties at around 6% and 9% respectively. The higher uncertainty in the pressure term is expected as the measurement errors in the velocity field get amplified in the velocity gradients and propagate into the pressure reconstruction. For the Reynolds stress term, considering that the Reynolds normal stress for the streamwise velocity component is equal to the variance of the streamwise velocity, the ratio $\frac{U_{R_{xx}}}{R_{xx}}$ (equation 4.16), for a sample size of $N = 350$, comes out to be 7.55%. The higher value in table 5.2 is because not all of the samples are statistically independent and therefore the effective number of samples is lower than 350. For reference, figure 5.19 shows the contribution from the individual terms, along with the respective expanded uncertainties (95% confidence level), for all of the tested configurations. The results for all the configurations are in line with the discussion made previously for the baseline.

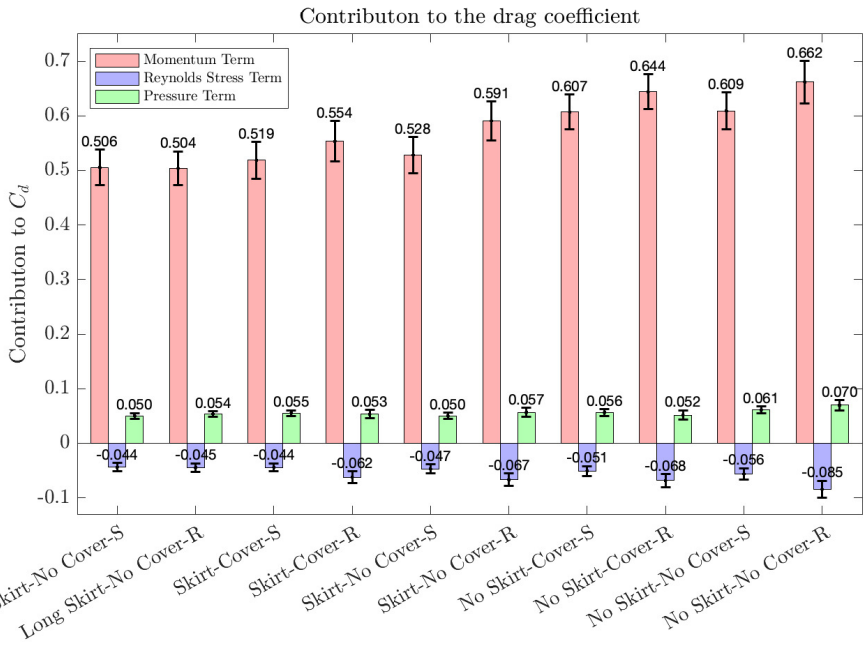

Figure 5.19: Contribution of the momentum, pressure, and Reynolds stress term to the total drag, along with the expanded uncertainty $(k = 1.96)$, for all the configurations tested

5.2.3 Discussion on the statistical significance of the drag results

As indicated earlier in table 5.2, the percentage uncertainty in the mean drag of the various configurations was in the range of 3 to 3.5%. Keeping in mind the relatively small deltas in drag between configurations comparing the effectiveness of wheel covers, as well as cases comparing wheel rotation, a t-test (Boslaugh 2012) was performed to determine which changes in mean drag were statistically significant.

Figure 5.20 shows the mean drag for the baseline configuration (*No Skirt-No Cover*) along with the calculated reduction in mean drag for the other four configurations tested. The error bars indicate the 95% confidence upper and lower limits for the reduction (or increase) in drag when compared to the baseline. Therefore, for each of the configurations, we can be 95% certain that the difference in drag compared to the baseline lies in the range indicated by the error bars. This is done for both the stationary and rotating wheels. For reference, the values (in percentage terms) are also stated in table 5.3. The configuration change of adding wheel covers over the baseline is marked with red as this is the only change over the baseline that did not result in a statistically significant reduction. However, when comparing the configurations within themselves, there are other changes that do not result in a statistically significant difference. This can be interpreted from the provided values for any given pair.

A similar exercise was performed for comparing rotating and stationary wheels. Figure 5.21 shows the results of this t-test, where the intervals are based on a 95% confidence level. As can be seen, while there is a systematic trend of the rotating configuration producing the higher mean drag, only the configuration *Skirt-No Cover* shows a statistically significant increase for the rotating case. Also, the overlap for the configuration *No Skirt-No Cover* is minimal and does indeed show a statistically higher drag for the rotating wheel if the confidence level is reduced to 80%.

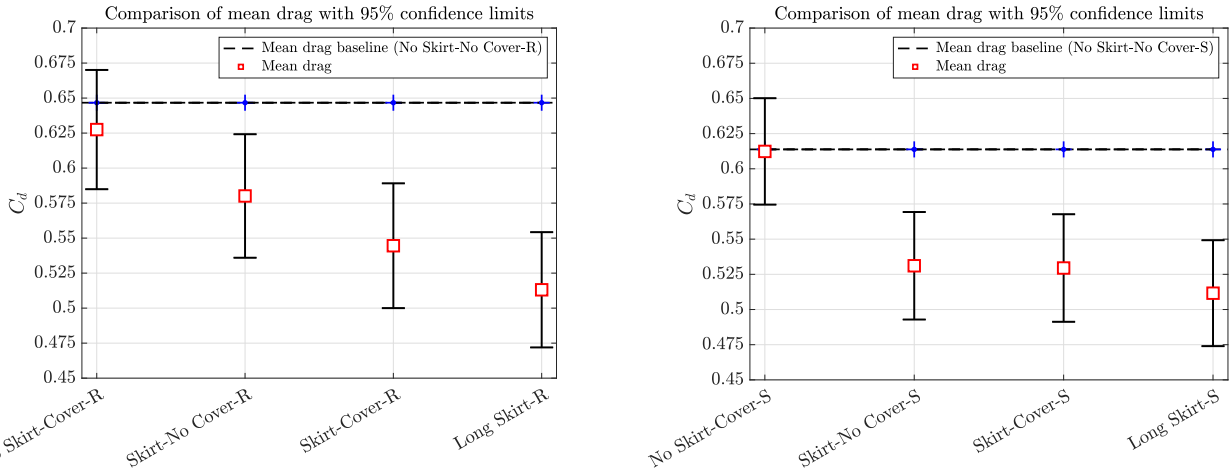

(a) Rotating wheel

(b) Stationary wheel

Figure 5.20: Reduction in mean drag compared to the baseline configuration (*No Skirt-No Cover*), along with 95% confidence limits

Configuration	Mean ΔCd (%)	Lower limit ΔCd (%)	Upper limit ΔCd (%)
Rotating Wheel			
Baseline (*No Skirt-No Cover-R*)	0	0	0
Baseline + short skirt	-10.30	-3.48	-17.12
Baseline + wheel cover	-2.97	+3.62	-9.55
Baseline + short skirt + wheel cover	-15.79	-8.90	-22.68
Baseline + long skirt	-20.66	-14.30	-27.02
Stationary Wheel			
Baseline (*No Skirt-No Cover-S*)	0	0	0
Baseline + short skirt	-13.47	-7.25	-19.70
Baseline + wheel cover	-0.23	+5.92	-6.39
Baseline + short skirt + wheel cover	-13.73	-7.51	-19.96
Baseline + long skirt	-16.65	-10.52	-22.78

Table 5.3: ΔCd (%) with respect to the baseline case (*No Skirt-No Cover*) for both the rotating and stationary wheels, along with the upper and lower 95% confidence limits. Marked in red are the changes with respect to baseline which do not show a statistically significant difference (null hypothesis cannot be rejected)

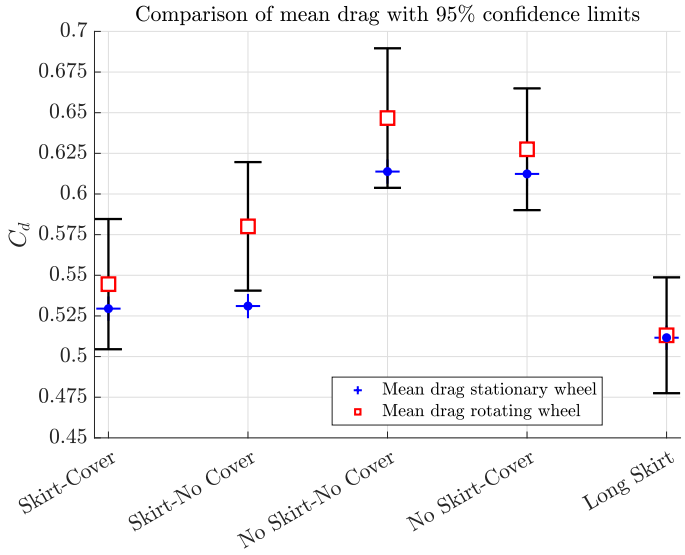

Figure 5.21: Increase in mean drag for the rotating configuration along with 95% confidence limits

5.3 Flow besides the wheel - Plane A and Plane C

In this section the results on the planes beside the wheel are presented, i.e. plane A and C, which are aligned with the axis of rotation of the front and rear wheel respectively (see figure 4.6). To give an overview of the flow characteristics in these planes, to begin with, streamwise velocity contours and in-plane horizontal velocity contours on plane A are presented for the baseline configuration (*No Skirt-No Cover*) with the wheels rotating (figure 5.22). The plot title shows the configuration along with the state of the wheels as *S/R* (stationary or rotating), and the measurement plane as *A/B/C/D*.

Looking at the streamwise velocity for the configuration *No Skirt-No Cover-R*, an area of reduced velocity can be seen in the upper region, starting at about midway through the body, spanning the gap between the wheel and body and extending along the sidewall of the wheel till about the top of the wheel cavity. The horizontal velocity plot in this region shows a weak inflow into the gap between the wheel and body. Following this a recovery to near freestream is seen in the streamwise velocity, corresponding with the inflow in the upper half of the wheel cavity. In the lower half of the wheel cavity, an outflow can be seen in the in-plane velocity plot, which corresponds with the region of flow reversal in the streamwise velocity plot. Finally close to the contact patch of the wheel (the term here is used only as nomenclature as the current test method has a gap between the wheel and ground), an outward horizontal velocity can be seen as the oncoming air in front of the wheel moves through a contracting region between the wheel and the ground.

The effect of the individual configuration changes on the flow field is discussed next.

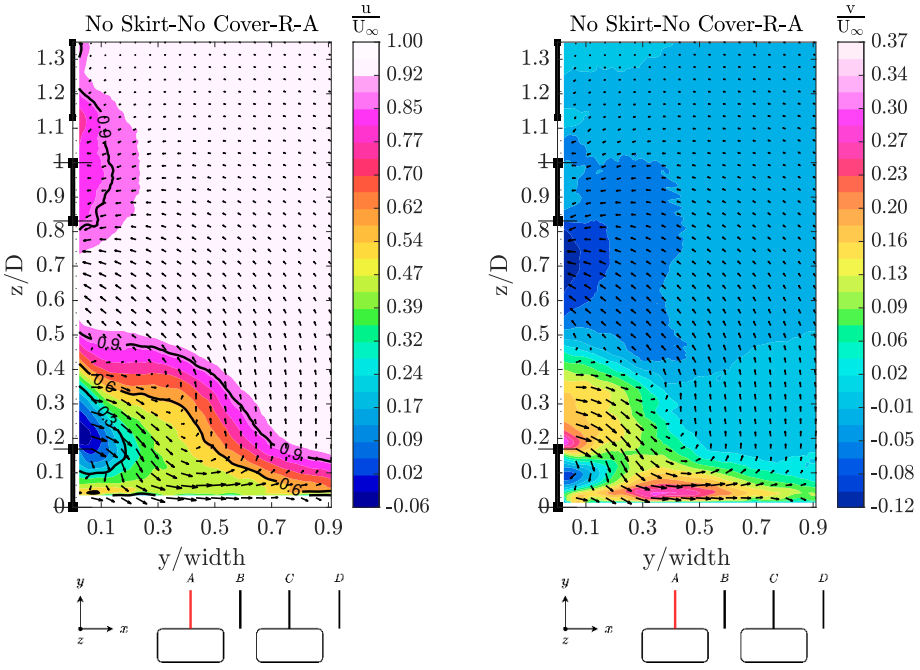

(a) Normalized streamwise velocity (u/U_∞) (b) Normalized horizontal velocity (v/U_∞)

Figure 5.22: $\frac{u}{U_\infty}$ and $\frac{v}{U_\infty}$ contours on plane A along with vectors of in-plane velocity for configuration *No Skirt-No Cover-R-A*. Marked in black along the z axis is the side wall region of the wheel and the body.

5.3.1 Effect of wheel rotation

Figure 5.23 shows the contour plots of the normalized streamwise velocity, comparing the effect of rotation for the configuration *Skirt-Cover,* on plane A. Looking at the third subplot showing the delta values (stationary subtracted from the rotating), it can be seen that the rotating case has a slightly higher velocity deficit near the top of the wheel. Apart from this, the overall profile of the $u/U_\infty = 1$ contour is nearly identical.

Looking next at the effect of rotation on a configuration without a wheel cover, figure 5.24 shows the streamwise velocity contours for *Skirt-No Cover.* Here again the contours for $u/U_\infty = 1$ are nearly identical other than the slight difference near the top of the wheel. Of note is the larger area of lower streamwise velocity near the lower edge of the wheel cavity for the rotating wheel, corresponding to the higher outflow for this case. Overall, the effect of rotation on the streamwise velocity is small in the plane beside the front wheel.

Worth considering is the similarity amongst the velocity fields in the lower region of the wheel, for the various configurations with the skirt fitted. This is attributed to the vortex centered around $(y = 0.36, z = 0.12)$ for the stationary wheel and around $(y = 0.38, z = 0.12)$ for the rotating wheel. Figure 5.25 shows the Line Integral Convolution (LIC) plots of the flowfield on plane A for the configuration *Skirt-Cover,* wherein these vortices can be seen. Line integral convolution, originally presented

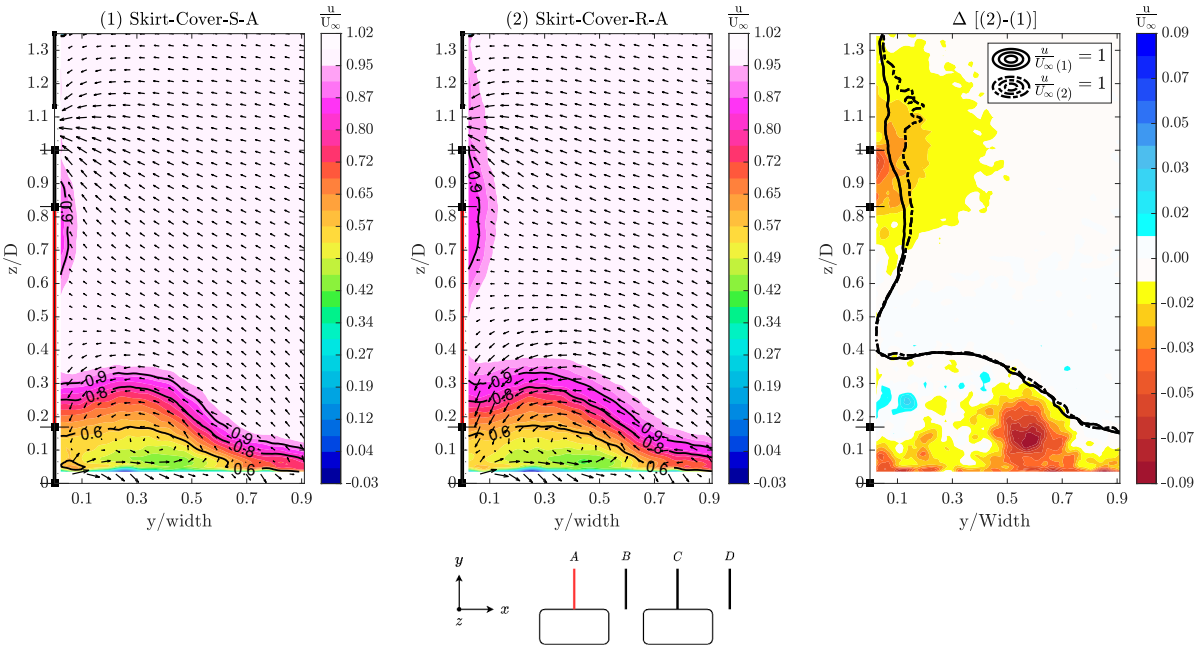

Figure 5.23: $\frac{u}{U_\infty}$ contours on plane A along with vectors of in-plane velocity for configuration *Skirt-Cover*. Marked in black along the z axis is the side wall region of the wheel and the body. Marked in red is the region occupied by the wheel cover.

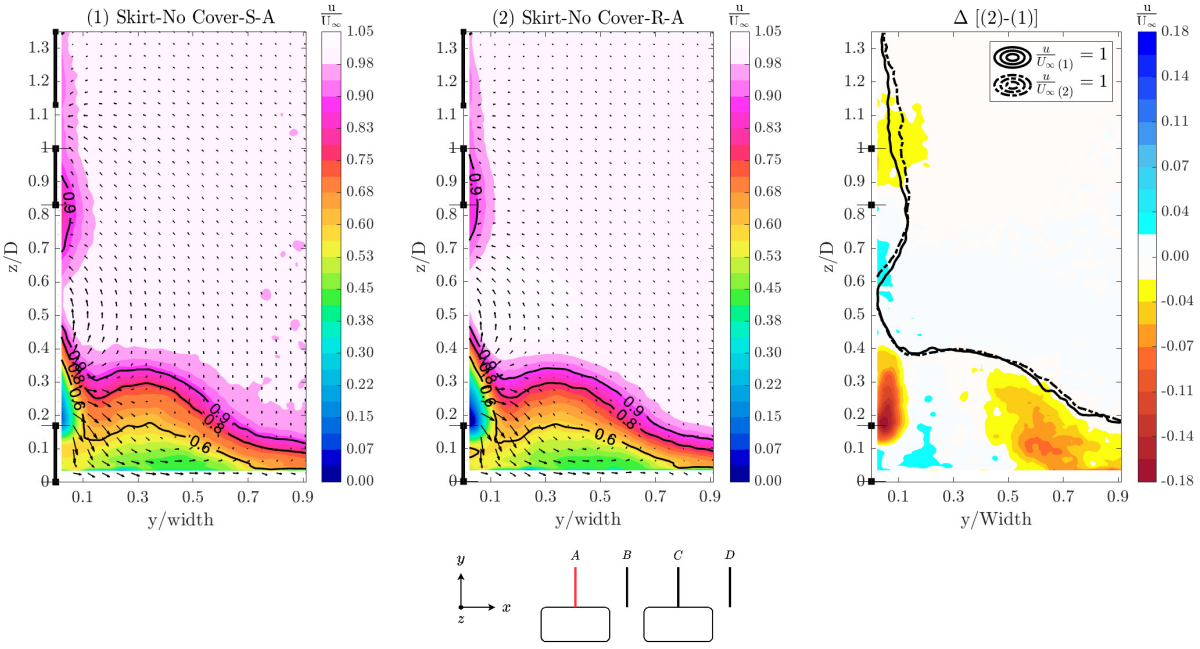

Figure 5.24: $\frac{u}{U_\infty}$ contours on plane A along with vectors of in-plane velocity for configuration *Skirt-No Cover*. Marked in black along the z axis is the side wall region of the wheel and the body.

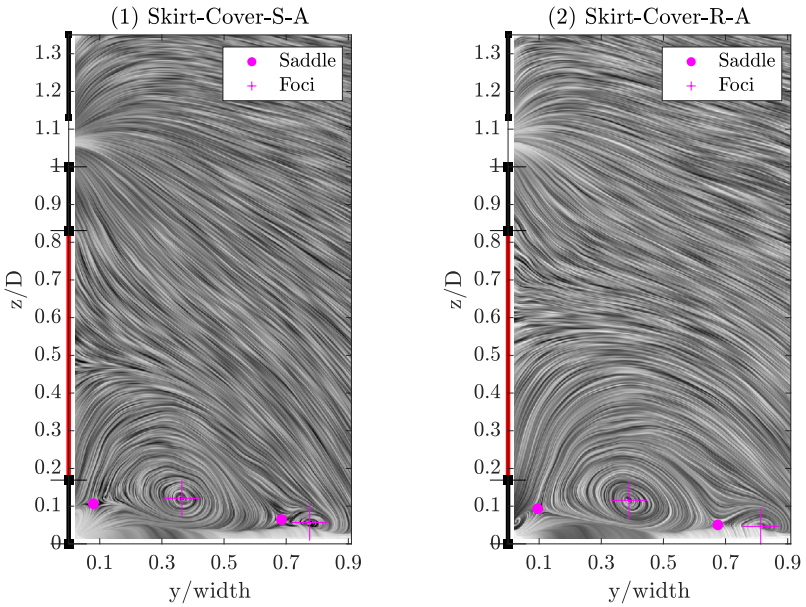

Figure 5.25: Line Integral Convolution images showing the flow structure on plane A for the configuration *Skirt-Cover.*

by (Cabral and Leedom 1993), is a visualization technique which, for fluids, results in images comparable to long-exposure photographs of tracer particles. Therefore the issue of streamline placement is mitigated, and the flow features can be visualized more clearly. Also shown are the critical points associated with the flow structures on plane A, identified as the intersection of the zero-contour lines of the in-plane velocity components. For the current discrete grid, each point with a change of sign for the in-plane velocity is identified and linear interpolation is used to determine the presence of a critical point. The points are further classified as foci or saddle points based on the method detailed in (Peikert 2007), wherein properties of the point's Jacobian are used to identify foci and saddle points, among other critical points.

This vortex dominates the velocity field in the lower region for all the skirted configurations and as a consequence the differences caused due to rotation (and to a certain degree the wheel covers, as detailed in sub-section 5.3.3), are overshadowed on the planes beside the wheels. As the vortex dissipates before the wake plane, the similarities in the streamwise velocity field on plane A do not translate to the wake plane, where significant differences between the rotating and stationary cases are seen in the region beside the wheel as discussed earlier.

A similar scenario to plane A is seen when comparing the effect of rotation on plane C. Figure 5.26 shows the normalized streamwise velocity, for the configuration *Skirt-Cover*, on plane C. The rotating case shows a higher deficit near the wheel top, more so than the difference seen on plane A, with the rest of the velocity contours being very similar. A significant difference can be seen in the in-plane velocity components near the wheel-body gap. This is discussed next.

With regards to the in-plane velocities, three regions, in particular, are seen which are affected by the change in configuration. The first is the inflow between the top of the wheel and the body, which is an

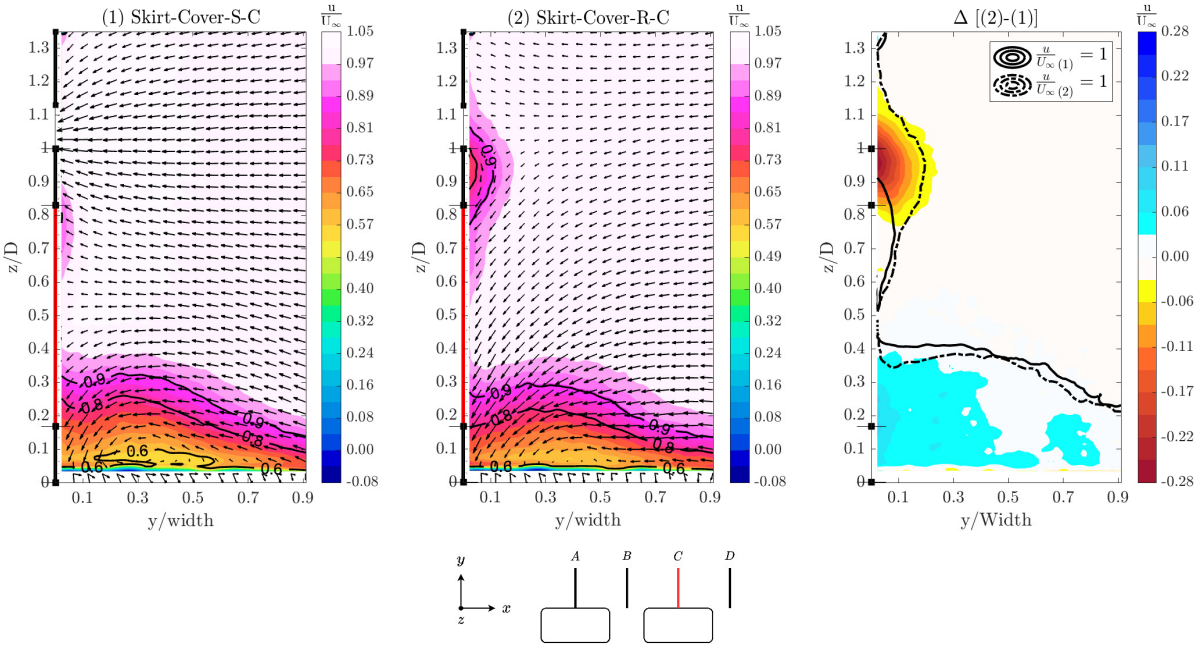

Figure 5.26: $\frac{u}{U_\infty}$ contours on plane A along with vectors of in-plane velocity for configuration *Skirt-No Cover*. Marked in black along the z axis is the side wall region of the wheel and the body. Marked in red is the region occupied by the wheel cover.

indicator of the pressure over the wheel, a strong function of wheel rotation. The second is the region spanning the wheel cavity, and the third is the region near the contact patch of the wheel.

Figure 5.27 plots the vertical variation of the normalized horizontal velocity component, along the edge of the wheel, spanning about 7 mm $\left(0.02 \leq \frac{y}{W} \leq 0.1\right)$. This is done for both plane A and C. For the front wheel (plane A, figure 5.27a), a net inflow is seen in the region between the top of the wheel and the body for all the configurations. Moreover, this inflow is larger for the stationary wheel for any given configuration. This is in line with the expectation of lower pressure near the top of a stationary wheel due to attached flow. The difference between stationary and rotating is significantly larger for plane C, where the stationary wheel continues to show an inflow, whereas the rotating wheel shows either an outflow or a (near) zero net flow. This is also as expected considering the separated flow over the top of the leading wheel. It is also in agreement with literature to the extent that the second wheel in a tandem configuration has been shown to produce a net downforce when rotating (Rasani et al. 2018).

Next, looking at the flow through the wheel cavity of the front wheel, an inflow is seen for the top half and an outflow for the bottom half, with the outflow being higher than the inflow. Also, regardless of the configuration, the flow is higher for the rotating wheel. Figure 5.28 shows these differences through contour plots of v/U_∞, wherein the higher inflow velocity in the wheel-body gap for the stationary wheel and the higher inflow velocity in the top half of the wheel cavity, as well as the higher outflow velocity in the bottom half of the wheel cavity, both for the rotating wheel, can be seen. For the rear wheel (plane C, figure 5.27b), the opposite is observed wherein an outward flow exists in the top half of the cavity and an inward flow in the bottom, except for the configuration *No Skirt-No Cover-S* which shows

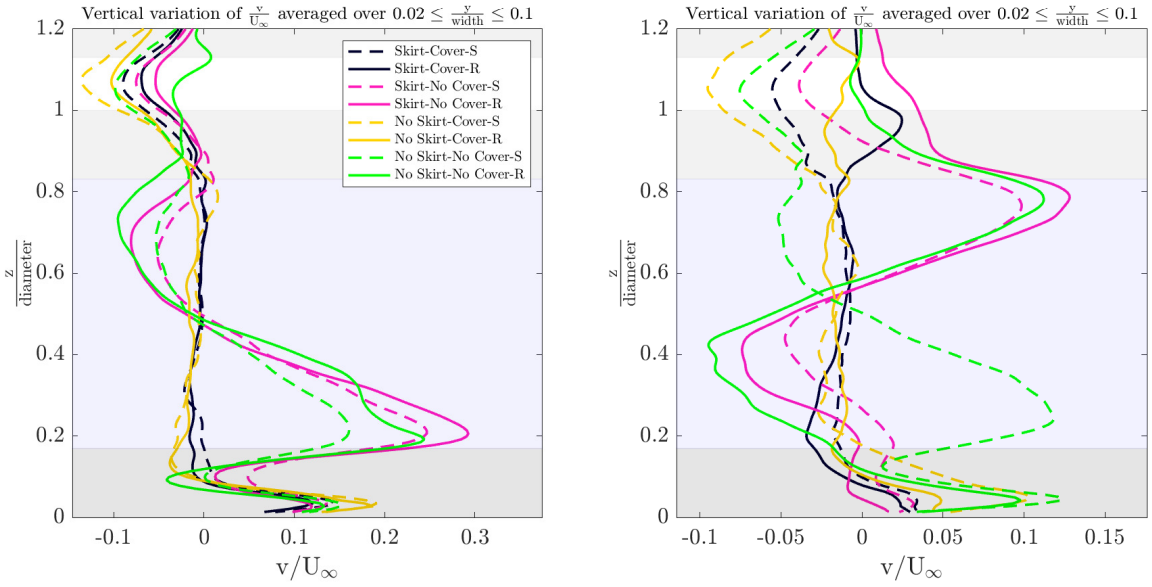

(a) Results on plane A

(b) Results on plane C

Figure 5.27: Vertical variation of the normalized horizontal velocity component averaged over $0.02 \leq \frac{y}{width} \leq 0.1$ beside the wheel. Marked in grey are the regions beside the side walls of the wheel and the body. Marked in light blue is the region beside the wheel cavity.

similar behavior to the front wheel. The reason for this observation is difficult to ascertain from the planar velocity data measured during the experiment. Even so, the general trend of the inflow/outflow velocity being higher for the rotating wheel remains, although the outflow velocities are nearly identical for the *No Skirt-No Cover* configuration.

Finally, looking at the region next to the contact patch, a sideward flow can be seen in figure 5.27a, where the horizontal velocity shows a peak between $v/U_\infty = .12$ and $v/U_\infty = .2$, depending on the configuration and wheel rotation. Figure 5.29 shows the velocity plot for this region.

As can be seen, there is a systematic trend of the velocity being higher for the stationary wheel, especially for configurations other than *No Skirt-Cover*. Figure 5.30 shows the contour plots where this difference can be seen for the configuration *Skirt-Cover*. The general trend of an outward velocity in this region is expected as the flow above the ground accelerates in front of the wheel as it traverses the contracting space between the wheel and the ground. On encountering the contact patch it emerges as a sideward jet and decelerates in the expanding space beside the wheel. In a setup with the wheel having a contact with the ground and with the ground moving, the sideward flow (or the jetting phenomenon as termed by Fackrell) is greater for the rotating wheel. However, in the current setup, where a gap of $2\ mm$ is present between the wheel and ground, and the ground is static regardless of wheel rotation, the expected trend reverses as the rotating wheel produces a lower pressure under it, thus dissuading flow from moving sidewards. This is supported by the surface pressure result measured by (Stapleford and G. W. Carr 1970), for wheels rotating above the ground. It also corresponds with the higher velocity seen in the lower half of the rotating wheel on the wake plane (figure 5.3). Moreover, a significant source of difference between

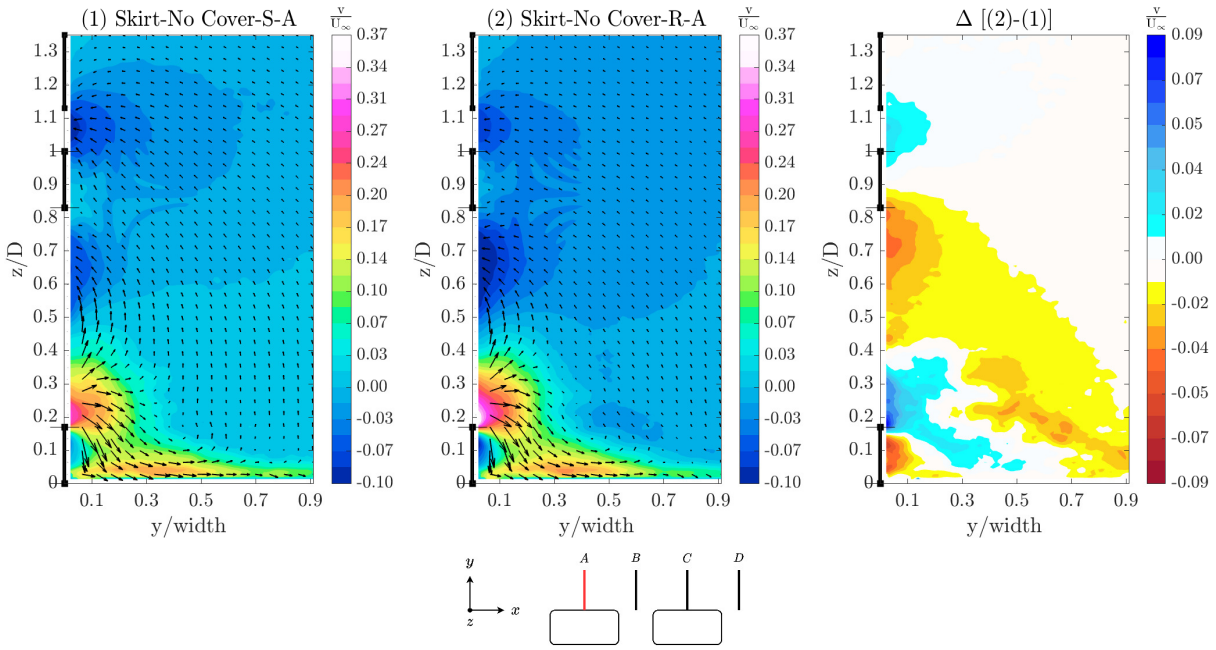

Figure 5.28: $\frac{v}{U_\infty}$ contours on plane A along with vectors of in-plane velocity for configuration *Skirt-No Cover*. Marked in black along the z axis is the side wall region of the wheel and the body.

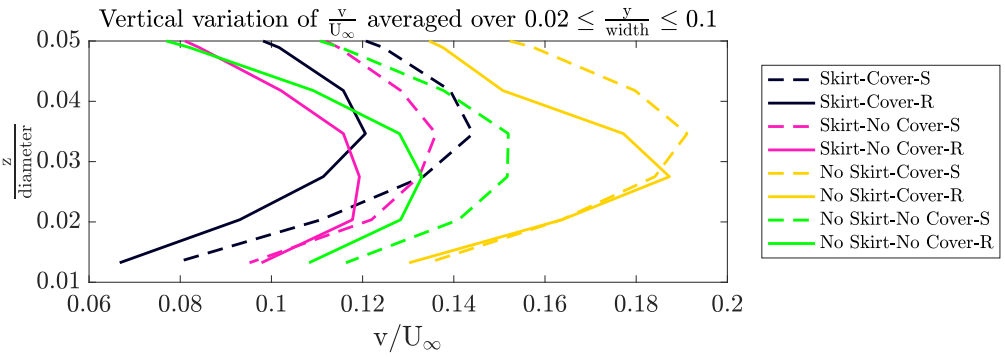

Figure 5.29: Vertical variation of the normalized horizontal velocity component, averaged over $0.02 \leq \frac{y}{width} \leq 0.1$ beside the wheel, for the region near the contact patch

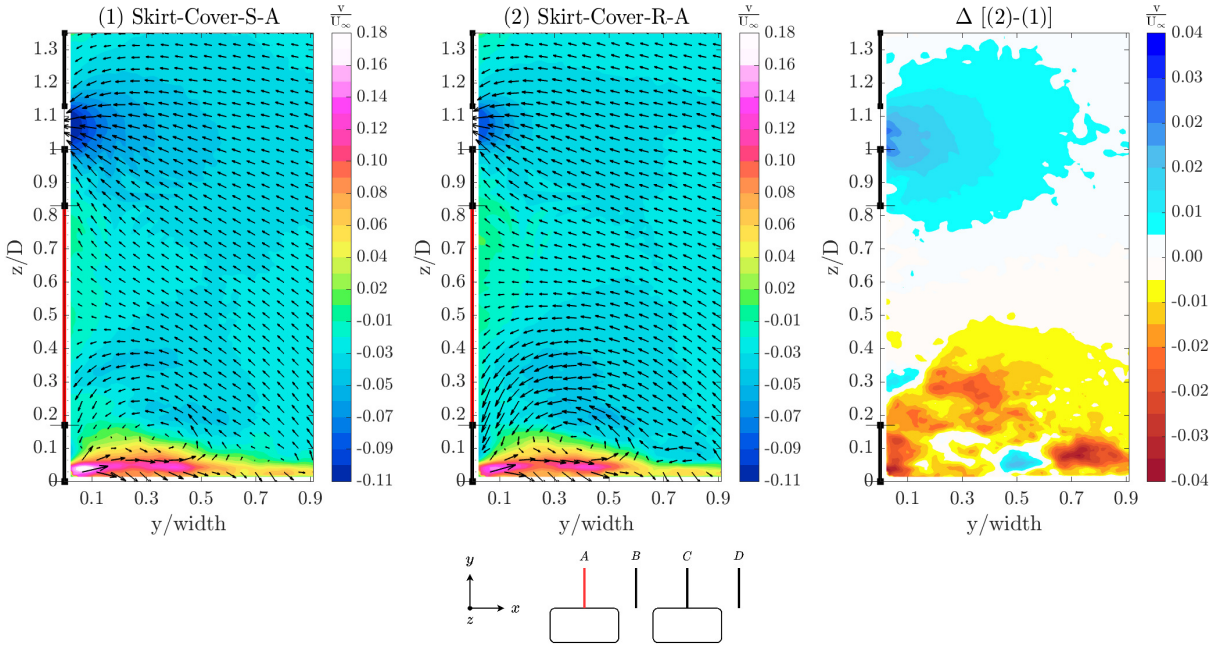

Figure 5.30: $\frac{v}{U_\infty}$ contours on plane A along with vectors of in-plane velocity for configuration *Skirt-Cover*. Marked in black along the z axis is the side wall region of the wheel and the body. Marked in red is the region occupied by the wheel cover.

the velocity fields besides rotating and stationary wheels comes from the rate at which the outward flow is convected away. For a rotating wheel the moving ground ensures a thinner boundary layer and thus faster convection, which means the sideward flow deflects more and the separation region beside the wheel is smaller. This effect is also inconsequential in the current setup, and is also one of the reasons for the limited variation observed between the streamwise velocity fields of the stationary and rotating wheel.

5.3.2 Effect of skirt

The effect of a skirt on the streamwise velocity in the planes beside the wheels was seen to be significantly greater than the effect of rotation. Figure 5.31 shows the comparison for the configuration *Skirt-Cover-R-A* and *No Skirt-Cover-R-A*. In the absence of the skirt, a large area of separated flow is seen, spanning the entire height of the wheel. Such a separation is not seen for an isolated wheel and is peculiar to the current setup, where, in the absence of a skirt, a shear layer is expected to form as the high momentum flow beside the model gets entrained in the low momentum flow ahead of the wheel and impinge on the wheel at an angle. In the absence of upstream velocity data though, the exact mechanism at play is difficult to ascertain. Moving downwards, the configuration without the skirt shows a gradual reduction in the width of the separated region, and a greater velocity deficit, over a larger region, is observed for the configuration with the skirt. This is primarily due to the vortex centered around $(y = 0.38, z = 0.12)$, seen in all configurations with a skirt.

Looking at the horizontal velocity contours for the same comparison (figure 5.32), the configuration *No*

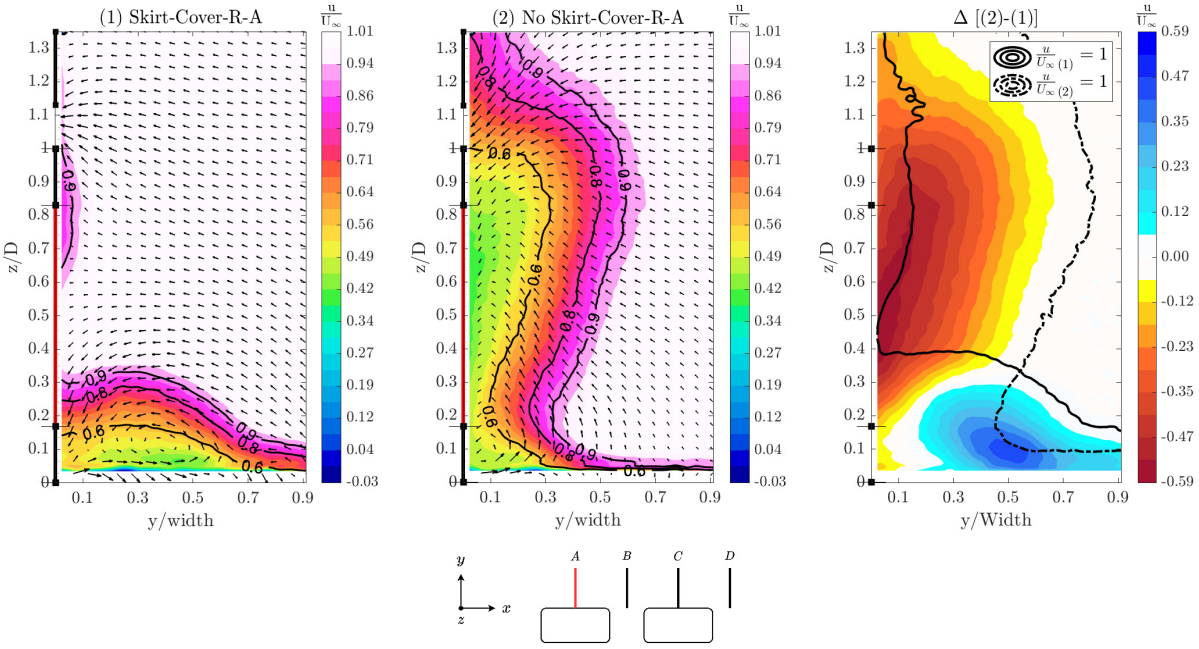

Figure 5.31: $\frac{u}{U_\infty}$ contours on plane A along with vectors of in-plane velocity for configuration *Skirt-Cover-R-A* and *No Skirt-Cover-R-A*. Marked in black along the z axis is the side wall region of the wheel and the body. Marked in red is the region occupied by the wheel cover.

Skirt-Cover-R shows a significantly higher inflow into the wheel-body gap, in fact, the highest of any configuration (as can be seen in figure 5.27a). This corresponds with the leftward (when looking at the back of the model) shift in the wake, which was also oberved to be the highest for this configuration (can be seen in figure 5.11). Also of note is the higher outflow near the contact patch, again the highest of any configuration. The higher outflow for a configuration without a skirt is expected as the oncoming, near ground, flow to the wheel is expected to have a higher momentum for this case.

Next, comparing the effect of skirts in the absence of a wheel cover, figure 5.33 shows the streamwise velocity for cases *Skirt-No Cover-R-A* and *No Skirt-No Cover-R-A*. Both configurations show a region of reduced velocity near the top of the wheel, extending upwards to the wheel-body gap. The deficit, however, is greater for the case without the skirt. The lower region for both the configurations is dominated by the outwards flow from the bottom half of the wheel cavity, resulting in a small region of reversed flow and a larger area with a velocity deficit. The deficit is again much larger without the skirt.

The horizontal velocity plot comparing the same configurations is in figure 5.34. Here the outward velocity at the bottom of the wheel cavity, between $.18 \leq z/D \leq .3$, is higher for the skirted configuration. In the without skirt configuration, a lower velocity is observed, but the outflow itself is spread over a greater vertical distance. The inflow at the top of the cavity is also higher for this case, resulting in a stronger shear layer near the central region of the wheel cavity. The inward velocities in the wheel-body gap are lower for the *No Skirt-No Cover-R-A* configuration, also the lowest of any of the configurations tested (figure 5.27a).

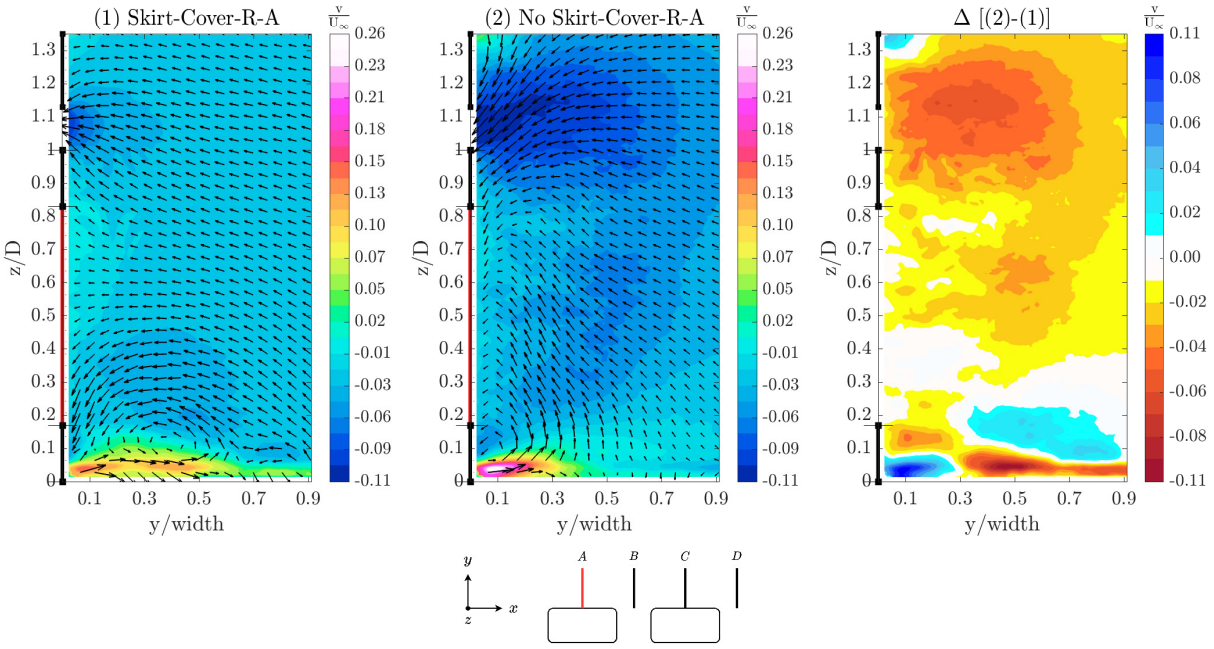

Figure 5.32: $\frac{v}{U_\infty}$ contours on plane A along with vectors of in-plane velocity for configuration *Skirt-Cover-R-A* and *No Skirt-Cover-R-A*. Marked in black along the z axis is the side wall region of the wheel and the body. Marked in red is the region occupied by the wheel cover.

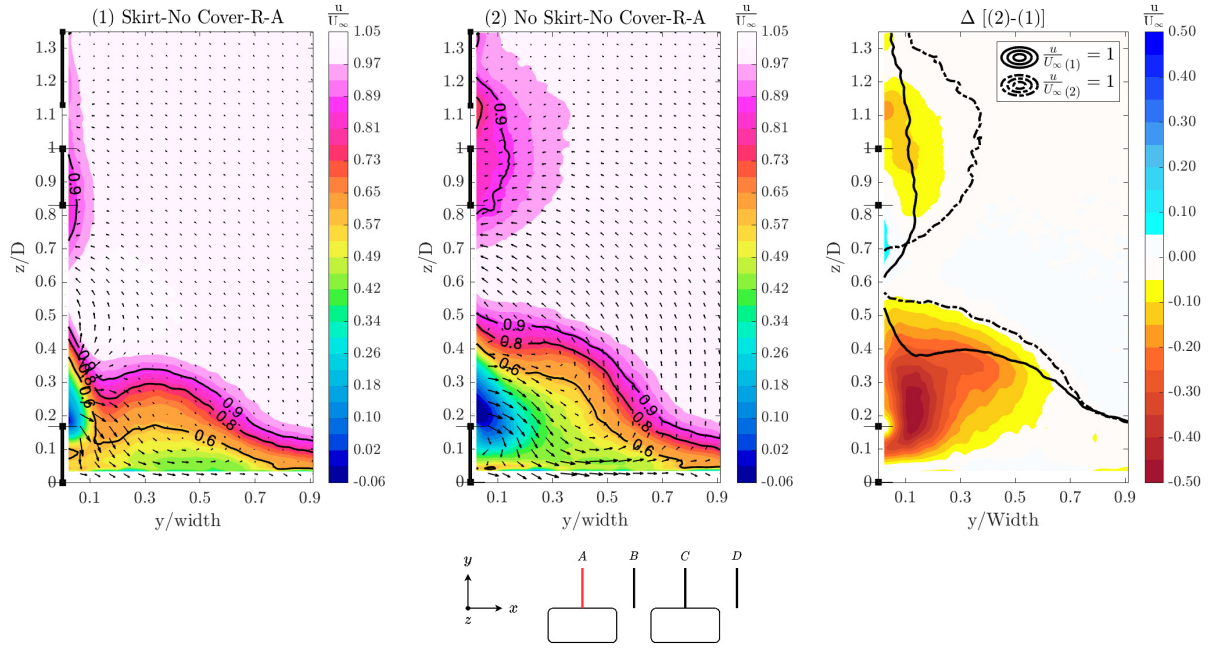

Figure 5.33: $\frac{u}{U_\infty}$ contours on plane A along with vectors of in-plane velocity for configuration *Skirt-No Cover-R-A* and *No Skirt-No Cover-R-A*. Marked in black along the z axis is the side wall region of the wheel and the body.

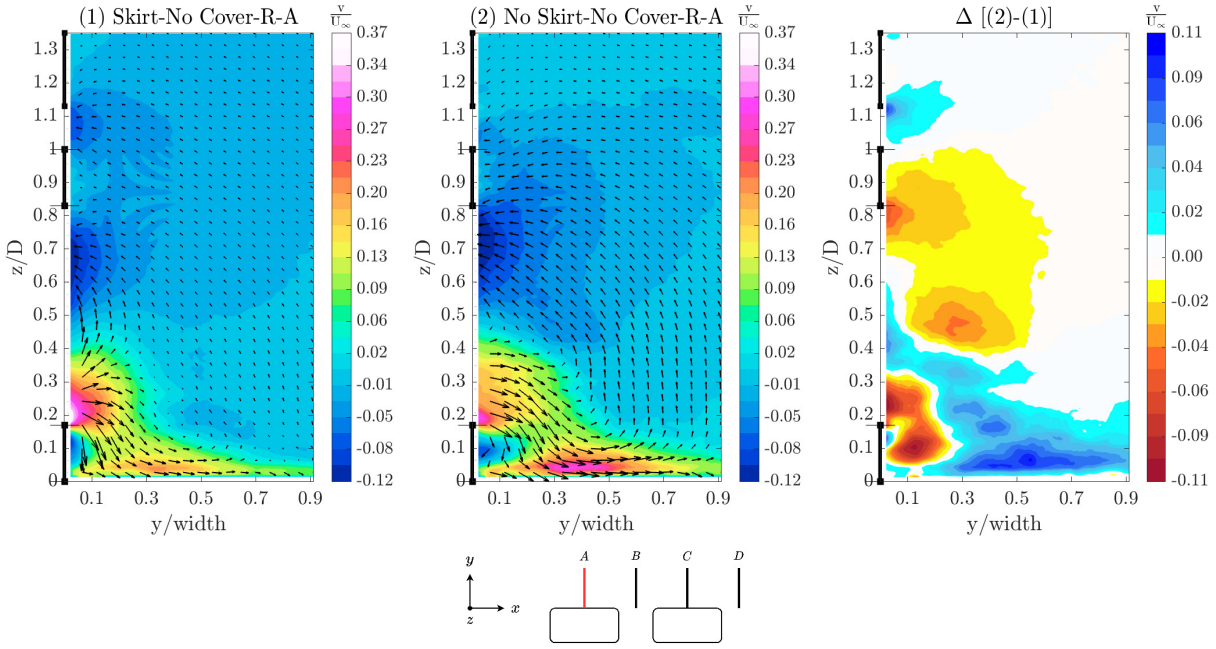

Figure 5.34: $\frac{v}{U_\infty}$ contours on plane A along with vectors of in-plane velocity for configuration *Skirt-No Cover-R-A* and *No Skirt-No Cover-R-A*. Marked in black along the z axis is the side wall region of the wheel and the body.

5.3.3 Effect of wheel covers

The results for the horizontal velocity component are presented first as the primary impact of the covers was on the in-plane velocity field (visible as vector arrows in the contour plot).

Figure 5.35 shows the comparison between the configurations *Skirt-Cover-R-A* and *Skirt-No Cover-R-A*. The difference exists only in the region occupied by the wheel cavity, with an outflow in the lower region and an inflow in the top region as seen before. The effect of the flow into and out of the wheel cavity is seen on the streamwise velocity as well (figure 5.36), which shows an area of flow reversal and a velocity deficit to the covered wheel near the lower region of the wheel cavity.

A similar comparison for configurations without a skirt is in figure 5.37. Here differences are seen not only in the wheel cavity region but also in the wheel-body gap and near the contact patch. The wheel cavity flow difference is the same as noted above for the skirted configurations. For the wheel-body gap, the covered configuration shows a significant inflow, absent for the configuration with uncovered wheels. As noted earlier, the covered wheel without a skirt shows the highest inflow of any of the configurations in this region, while the uncovered wheel without a skirt shows the lowest. Given that the upstream conditions between these can be expected to be similar, the greater inflow indicates a more attached flow at the top of the covered wheel. The plot for the turbulent kinetic energy in the wake plane for the region within the projected wheel (figure 5.9), also shows significantly larger velocity fluctuations for the uncovered wheels in the upper half of the model, which corresponds with the finding here.

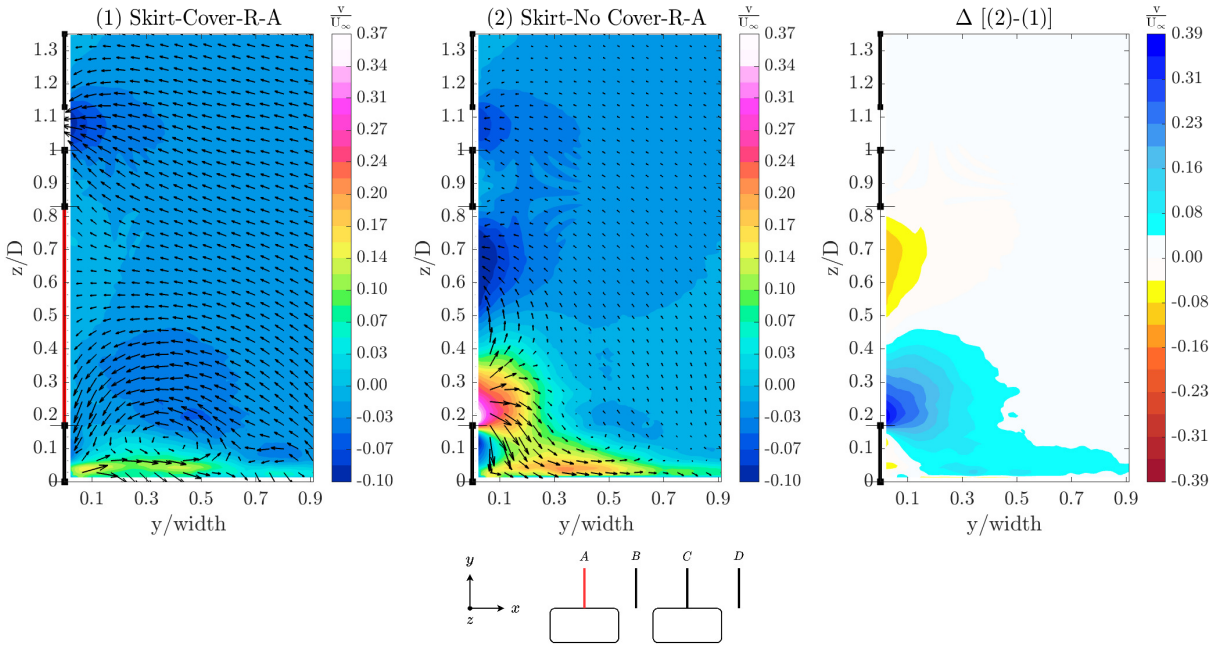

Figure 5.35: $\frac{v}{U_\infty}$ contours on plane A along with vectors of in-plane velocity for configuration *Skirt-Cover-R-A* and *Skirt-No Cover-R-A*. Marked in black along the z axis is the side wall region of the wheel and the body. Marked in red is the region occupied by the wheel cover.

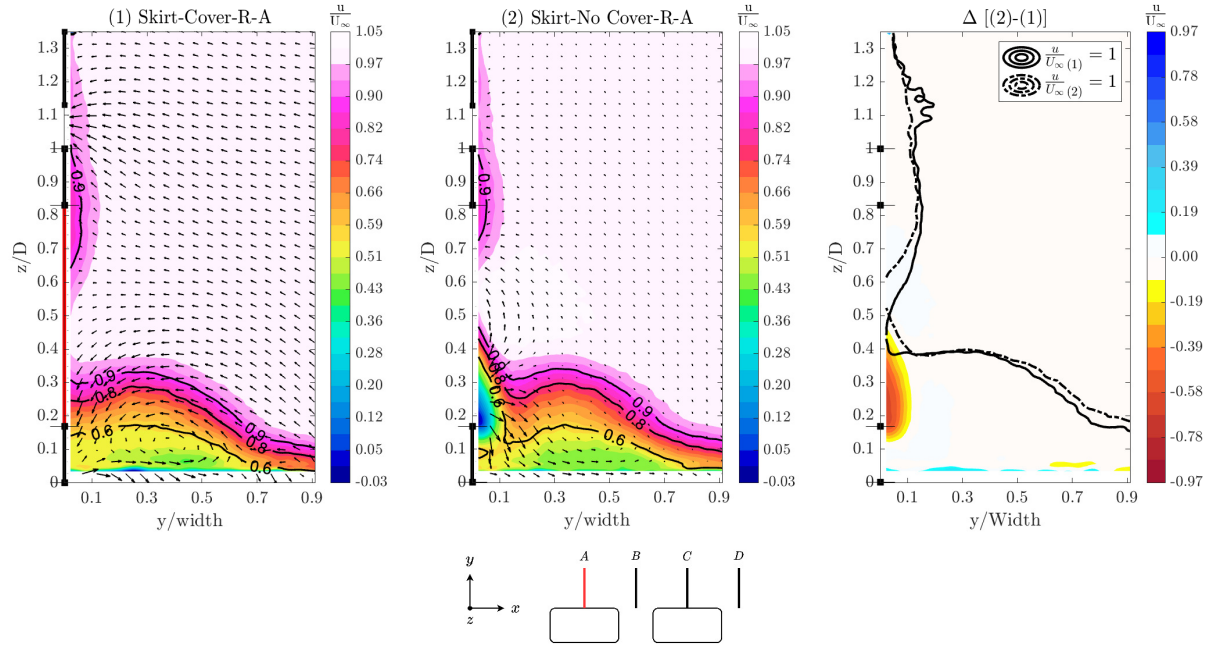

Figure 5.36: $\frac{u}{U_\infty}$ contours on plane A along with vectors of in-plane velocity for configuration *Skirt-Cover-R-A* and *Skirt-No Cover-R-A*. Marked in black along the z axis is the side wall region of the wheel and the body. Marked in red is the region occupied by the wheel cover.

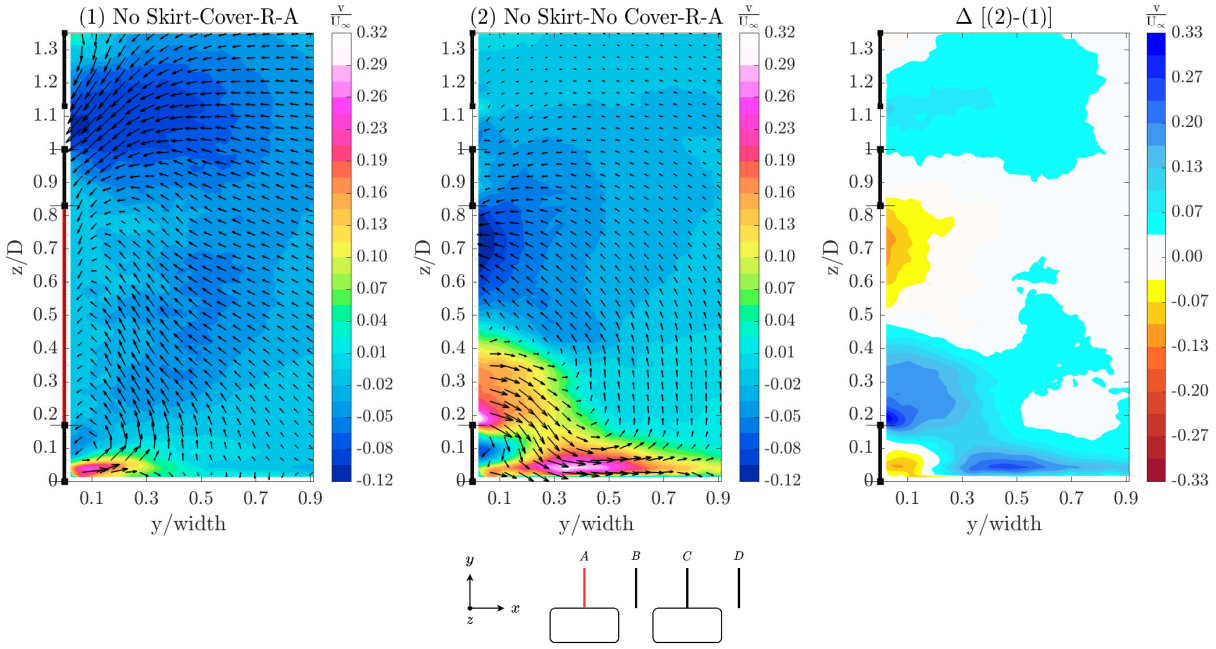

Figure 5.37: $\frac{v}{U_\infty}$ contours on plane A along with vectors of in-plane velocity for configuration *No Skirt-Cover-R-A* and *No Skirt-No Cover-R-A*. Marked in black along the z axis is the side wall region of the wheel and the body. Marked in red is the region occupied by the wheel cover.

5.4 Wheel covers with openings

In this section, the results for wheel covers with openings (differing the percentage of coverage area and radial placement, described in section 4.2) are discussed. The discussion is limited to the horizontal component of velocity as the most appreciable difference was seen here. Moreover, the configuration *Skirt-Cover-R* is used as the baseline for comparison as the wheel covers with the different openings were only tested with the skirt fitted and the wheels rotating.

To begin with, the baseline is compared with the configuration having 50% coverage, with the openings in the outer region, ie. *Skirt-50% Out-R*, as the variation between these is the maximum amongst all of the configurations. As can be seen in the delta plot (figure 5.38), the differences in the velocity field are largely restricted to the region near the openings. Similar to the case with the wheel cavity open (*Skirt-No Cover-R*), an outflow is seen in the bottom opening and an inflow in the top opening, with the outflow velocity being higher than the inflow.

Next, in figure 5.39, line plots are presented, showing the vertical variation of the normalized horizontal velocity component, averaged over $\left(.02 \leq \frac{y}{W} \leq .04\right)$. Worth noting here is that the horizontal velocity component next to the wheel cover is negative in the plots. This is because the velocity data next to the cover, spanning about $2\ mm$, was discarded due to reflections. Any inflow or outflow noted henceforth is a superposition on this negative velocity.

Starting with the plot for the outer radial position (figure 5.39a), a net outflow is seen in the lower region, aligned with, and peaking close to the lower edge, of the bottom opening. Also, regardless of the coverage

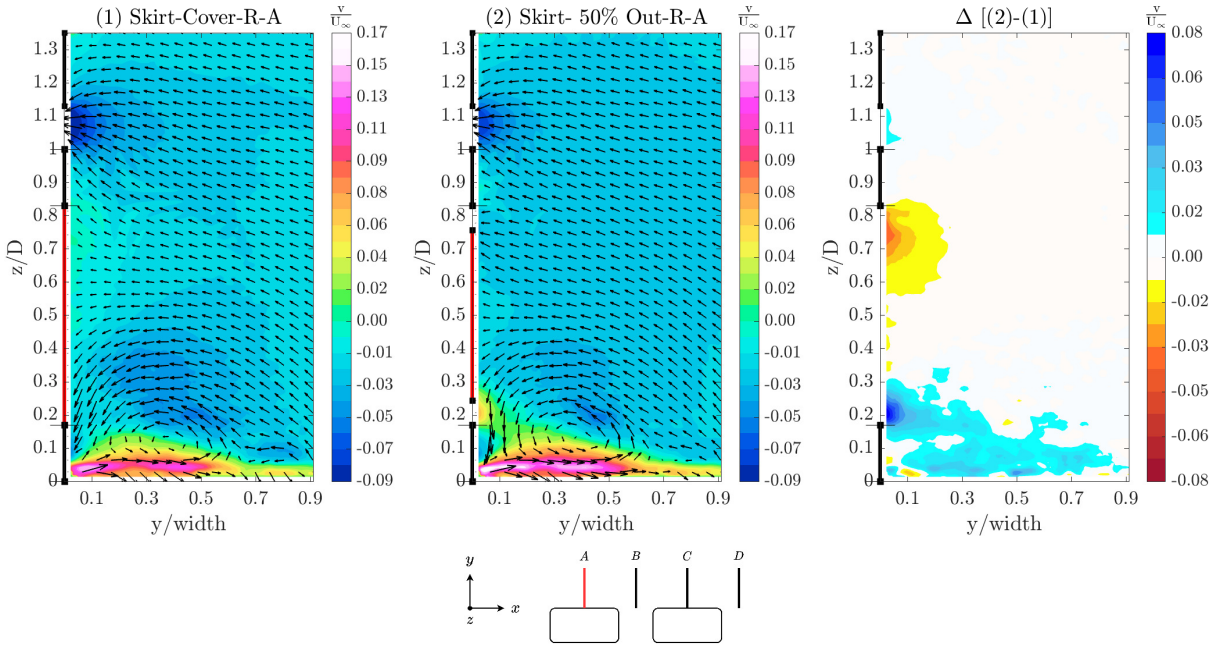

Figure 5.38: $\frac{v}{U_\infty}$ contours on plane A along with vectors of in-plane velocity for configuration *No Skirt-Cover-R-A* and *Skirt-50% Out-R-A*. Marked in black along the z axis is the side wall region of the wheel and the body. Marked in red is the region occupied by the wheel cover.

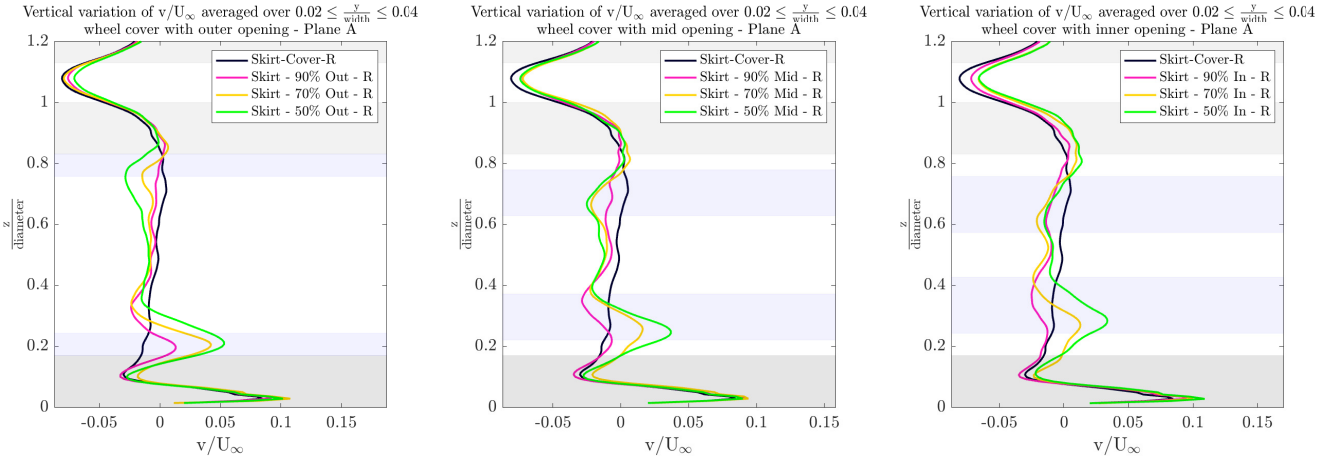

(a) Outer Opening (b) Middle Opening (c) Inner Opening

Figure 5.39: Vertical variation of the normalized horizontal velocity besides the wheel. Marked in grey are the regions beside the side walls of the wheel and the body. Marked in light blue is the region beside the wheel with an opening in the wheel cover.

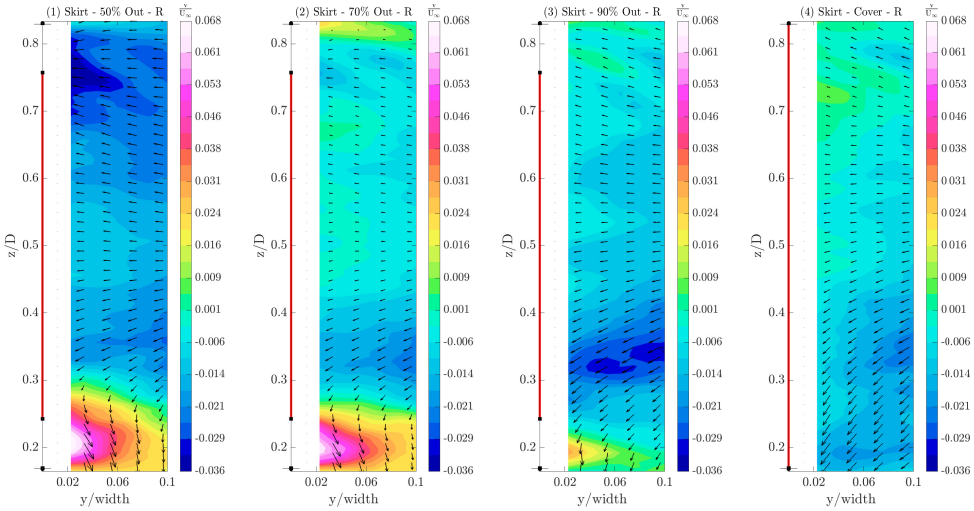

Figure 5.40: $\frac{v}{U_\infty}$ contours on plane A along with vectors of in-plane velocity for configuration wheel covers with outer opening. Marked in red is the region occupied by the wheel cover.

percentage, the outflow is present over (nearly) the entire radial span of the opening. At the top, a clear peak for the inflow velocity is only seen for the 50% coverage area. A small net inflow is observed for the 70% coverage and a near-zero inflow/outflow for the 90% coverage (see figure 5.41b). The velocity contour plot for this comparison is in figure 5.40. Visible here is the decrease in the outward and inward velocities with increasing coverage, with a significant inflow at the top limited to the 50% coverage area case.

Next, looking at the line plot for the middle opening (figure 5.39b), a significant net outflow at the bottom is seen only for the 50% coverage area and a significant net inflow at the top for the 50% and 70% coverage areas. Worth noting is the considerable inflow at the bottom for the 90% coverage case (seen in contour plot of figure 5.42 and in absolute value in figure 5.41a). This is because the underlying velocity field on plane A has a negative horizontal component. A similar scenario is observable in other cases as well, wherein, because the horizontal component of the in-plane velocity on plane A is primarily negative (unless otherwise affected by a particular flow structure), an inflow into the openings in the wheel cover is seen by default, unless the outward velocity from an opening is large enough to produce a net positive outflow when superimposed on the underlying velocity field. Despite the net inflow into the bottom opening for the case with 90% coverage, a decrease in the negative horizontal component can be seen in figure 5.39b, indicating the possibility of a weak outflow had the velocity data adjacent to the cover (without the $2\ mm$ gap) been available.

Finally looking at the inner radial position (figure 5.39c), a net outflow at the bottom, similar to the middle position, is only present for the 50% coverage area. For all other coverage areas, both top and bottom openings show either a net inflow or a near-zero flow on account of a weak outflow over a part of the opening combined with an inflow over the rest (for e.g. the 70% coverage area in figure 5.43). The net inflow/outflow over the openings is summarized in figure 5.41.

Comparing the velocity contours across radial positions for each of the coverage areas, the outflow at

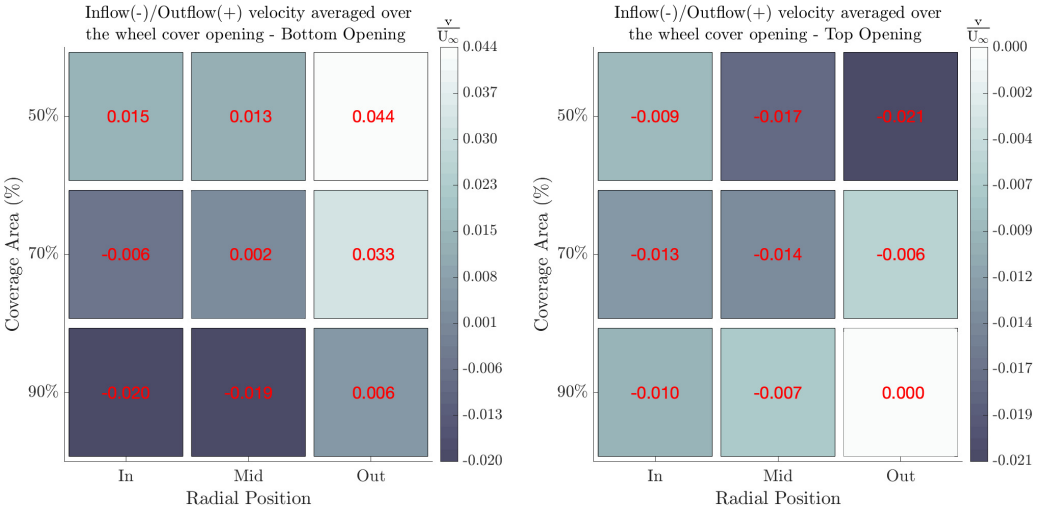

(a) Bottom Opening (b) Top Opening

Figure 5.41: $\frac{v}{U_\infty}$ variation with percentage coverage and radial position, averaged over the opening in the wheel cover, for both the top and the bottom opening, on plane A. Top and bottom openings refer to the opening above and below the wheel centerline respectively when viewed on the measurement plane.

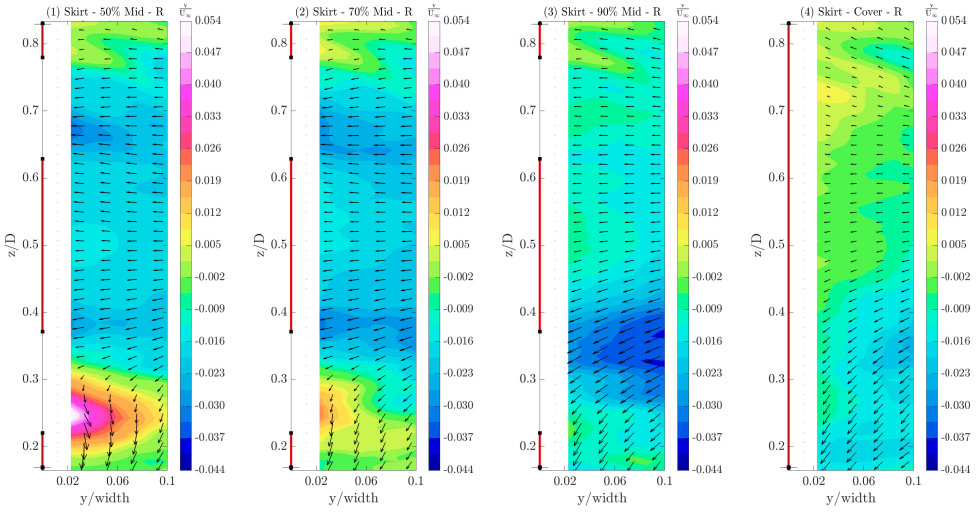

Figure 5.42: $\frac{v}{U_\infty}$ contours on plane A along with vectors of in-plane velocity for configuration wheel covers with middle opening. Marked in red is the region occupied by the wheel cover.

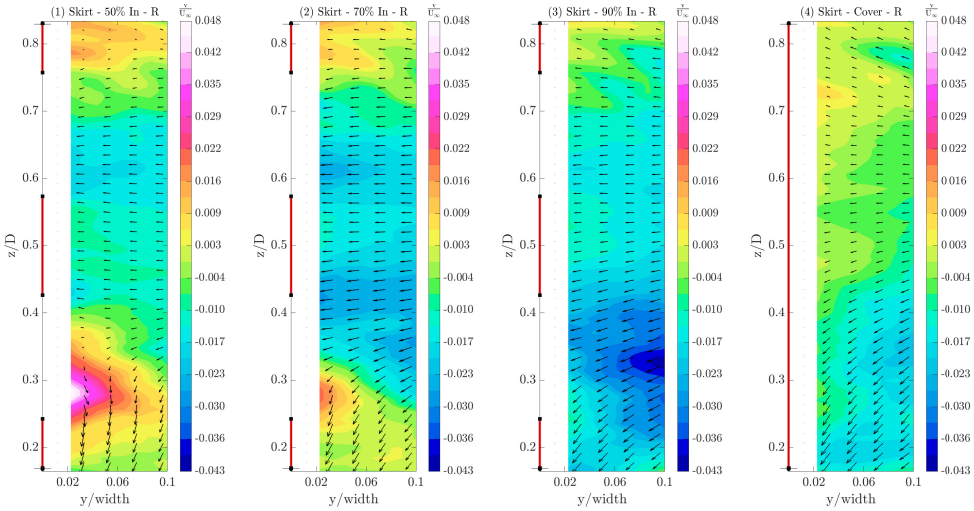

Figure 5.43: $\frac{v}{U_\infty}$ contours on plane A along with vectors of in-plane velocity for configuration wheel covers with inner opening. Marked in red is the region occupied by the wheel cover.

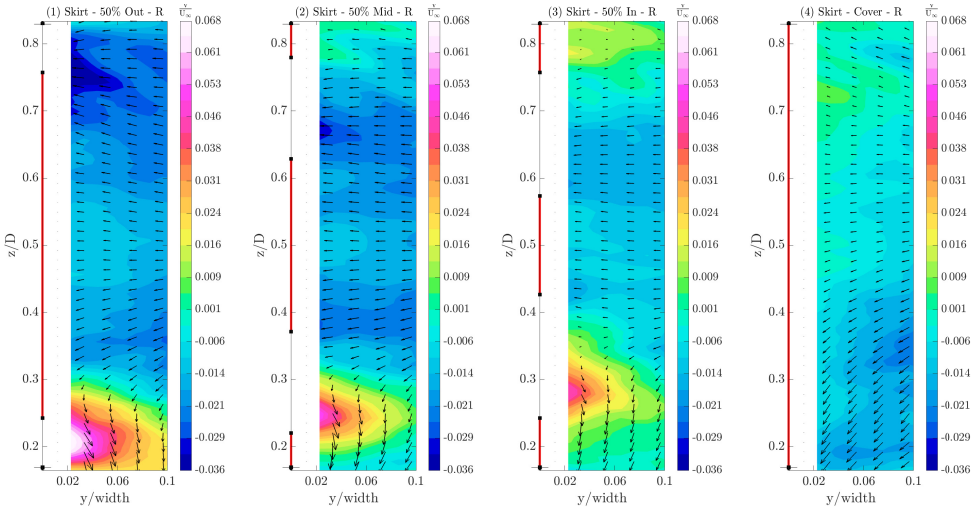

Figure 5.44: $\frac{v}{U_\infty}$ contours on plane A along with vectors of in-plane velocity for configuration wheel covers with 50% coverage. Marked in red is the region occupied by the wheel cover.

the bottom of the wheel cavity, if observed, is seen to decrease as the opening is moved towards the center of the wheel. Furthermore, for the 70% and 90% coverage areas, the outflow reduces enough to change to an inflow as the the effect of the opening on the flow reduces with increasing coverage and the underlying velocity field starts to dominate (for example the middle position in figure 5.45) . The trend for the inflow at the top is similar to the outflow at the bottom for only the 50% coverage area (figure 5.44), wherein the outer radial position has the highest inflow.

For the higher coverage areas (70% and 90%), the trend differs, with the middle and inner openings showing a higher inflow velocity than the outer opening, once again due to the decreasing influence of the openings with increasing coverage. Therefore, the middle and inner openings simply align with an existing flow field, which now dominates, and in the absence of a restriction, a higher negative velocity is seen. This is seen in figure 5.45, where the in-plane horizontal velocity near the top opening is similar for the *70% In* and *70% Mid* cases whereas the *70% Out* matches more to the completely covered

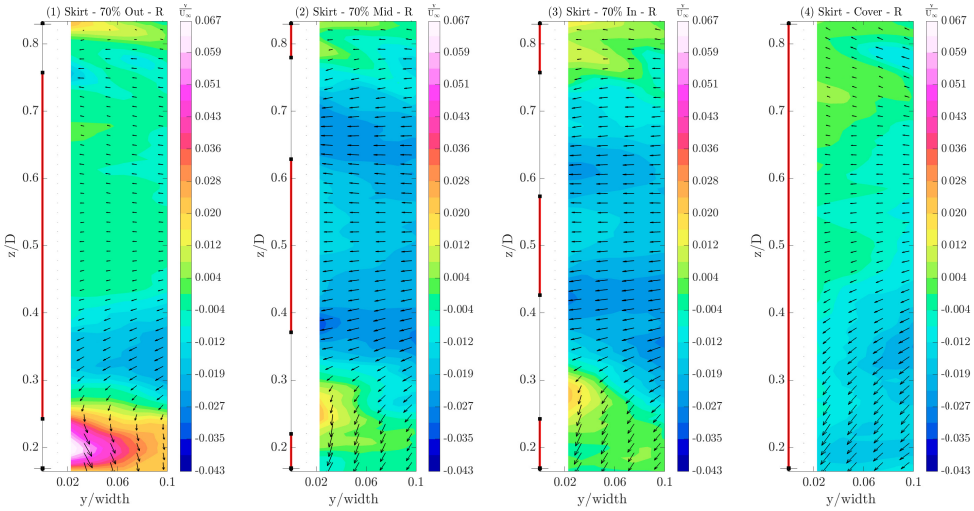

Figure 5.45: $\frac{v}{U_\infty}$ contours on plane A along with vectors of in-plane velocity for configuration wheel covers with 70% coverage. Marked in red is the region occupied by the wheel cover.

configuration.

Chapter 6

Conclusion and Recommendations

6.1 Conclusion

The work in this thesis was focused on studying the aerodynamics of trailer wheels in tandem. Of particular importance was to study the effect of wheel rotation, side-skirts, and wheel covers on the flowfield and drag. For this planar stereo PIV measurements were made in the near wake of the model, and on planes beside the wheels.

Looking at the drag values, it was seen, expectedly, that the configuration without skirt or wheel covers produced the highest drag. Treating this as the baseline, it was seen that the long side-skirt was the most effective in reducing drag, followed by the configuration with both the short skirt and wheel covers fitted, then only the short skirt, and finally only with wheel covers fitted. A systematic trend was observed, across configurations, of the rotating wheels producing more drag than the stationary wheels, although a statistically significant increase was only seen for the configuration *Skirt-No Cover*. In general, uncovered wheels showed a greater increase in drag due to rotation than covered wheels, with the configuration having the long skirt fitted showing almost no difference. As a consequence, rotation had a noteworthy influence on the effectiveness of the drag-reducing devices when compared with each other. In particular, it was seen that the wheel covers only showed an appreciable benefit to drag for the rotating wheel. As such, the inclusion of wheel rotation in the test setup is important for evaluating wheel covers.

Distinct differences were also seen in the spatial distribution of the streamwise velocity deficit in the wake of the rotating and the stationary wheels. This was particularly so for the region within the width of the projected wheel, with the rotating wheel showing a larger deficit in the top half of the wheel and the stationary wheel in the bottom half. This is expected to have occurred due to the earlier separation of flow on top of a rotating wheel, corresponding with the higher turbulent kinetic energy observed in the upper region. The effect of the difference in the separation point between the rotating and stationary wheels was also seen in the vertical velocity component, with a much stronger downwash for the stationary wheel. These differences in the wake velocity would have an impact on the drag of any

downstream device such as mud-flaps, reiterating the importance of including wheel rotation in the test setup when geometries in and around the wheels are of interest. On the planes beside the wheels (plane A and C), the effect of rotation on the streamwise velocity was observed to be limited, with the flow field being dominated by the influence of the side-skirt and wheel covers.

The effect of the side-skirt on the streamwise velocity in the wake plane was primarily seen in the magnitude of the streamwise velocity deficit, the width of the wake, and the degree of asymmetry of the wake, with the configurations without the skirt fitted showing a higher velocity deficit, a wider wake, especially in the top half of the model, and greater asymmetry with the wake shifted to the left when viewed from behind. On the planes beside the wheels, the effect of the skirt was seen to be considerably greater than wheel rotation, with the configurations without the skirt fitted showing a greater region of separated flow and greater velocity deficit than the configurations with the skirt fitted. This can be, as a fair assumption, thought to be the result of a shear layer forming in the absence of a skirt, starting near the rear-edge of the bluff body where the front-edge of the skirt fits, and entraining the high momentum flow beside the model into the low momentum flow in front of the wheel, thus impinging on the wheel at a certain angle. In the absence of data upstream of plane A though, the exact flow conditions that motivate this are not determinable and should be focussed upon in further studies.

The effect of wheel covers on the streamwise velocity in the wake plane was limited primarily to a marginally wider wake and a slightly higher velocity deficit for the uncovered wheel. This was seen in the drag values as well which did not vary significantly between the covered and uncovered configurations, especially for the stationary wheel. As mentioned earlier, the effects of wheel rotation were observed to be enhanced in the absence of wheel covers. This was seen for example in the greater downwash in the region behind the projected body for the uncovered wheel, which corresponded with the higher turbulent kinetic energy observed in the upper region of the projected wheel. On the planes beside the wheels, the effect of wheel covers was more apparent with clear inflow/outflow seen over the region of the wheel cavity. For the front wheel, an inflow in the top half of the cavity and an outflow from the bottom half were seen regardless of the rest of the configuration. For the rear wheel, the opposite behavior was seen except for the configuration *No Skirt-No Cover-S*, which replicated the behavior of the front wheel. The reason for this observation is difficult to ascertain from the planar velocity data measured during the experiment and motivates further study.

Finally, 9 wheel covers with openings varying in the percentage of coverage and radial placement were tested with the skirt fitted and the wheels rotating. Flow through the wheel cover was observed, varying the magnitude and direction (inflow/outflow) depending on the coverage area and radial position. With regards to the coverage area, the general trend of inflow from the top and outflow from the bottom of the wheel cavity, also seen with the wheel cavity open, was repeated (with lower magnitudes) for the 50% and 70% coverage areas. On the other hand, the wheel cover with 90% coverage area showed either an inflow or (near)zero net flow for both the top and bottom openings, with the underlying flow structures on the plane dominating. With regards to the radial placement, the outermost opening had the greatest influence on the flowfield, showing the greatest outflow at the bottom for all the coverage

areas. By comparison, the middle and inner openings had a smaller influence on the underlying flowfield (especially for the 70% and 90% coverage areas), and therefore primarily showed an inflow for both the top and bottom openings, in line with the underlying negative horizontal component of velocity.

6.2 Recommendations

In this section certain recommendations are made for future studies on the aerodynamics of trailer wheels.

As noted above in the conclusion, certain flow phenomena were observed in the results presented herein, where the exact mechanism at play was not determinable due to limited data i.e. planar data on a limited number of crossflow planes (normal of the plane aligned with the freestream direction). In this regard, it is recommended to either gather data on certain streamwise planes (normal of the plane aligned with the y- or the z-axis) or use a volumetric technique. Of particular importance is the flow field upstream of the wheels and the region between the front wheel and the rear wheel.

A volumetric technique would also allow the determination of the flow around the surface of the wheel, which is necessary to get an accurate measurement for the mass flow into or out of the wheel cavity. This is shown in figure 6.1 which depicts the various regions where the flow can go in or out of the wheel. As an alternative, data can also be gathered on vertical streamwise planes (normal of the plane aligned with the y axis) on both sides of the wheel, with the flow in/out of the gap between the dual wheels determined through mass conservation.

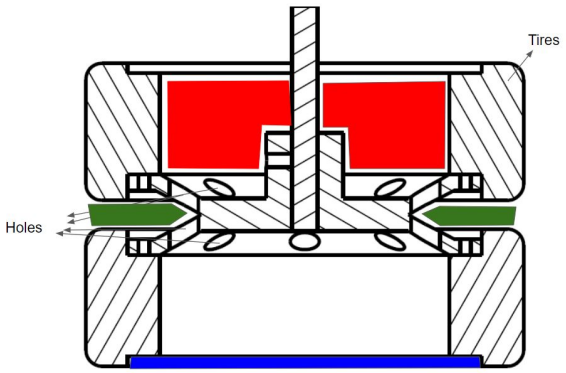

Figure 6.1: Schematic of the wheel with the regions of inflow/outflow marked. In red is the inboard region of the wheel where the brakes are housed, in blue is the area covered by the wheel cover, and in green is the region between the two wheels.

Another limitation of the current study is the uncertainty in the drag measurements. As was seen, the effect of wheel covers on the drag is rather small and therefore such a measurement will benefit from a force balance with the required precision.

To gain a more complete understanding of the overall parasitic effect of a rotating wheel on the power source of a vehicle (engine/ electric motor etc.), the moment created by the off-center aerodynamic force

acting on the wheel (called "fan moment" or "ventilation drag") should also be accounted for, especially when the design of wheel covers is of primary interest. This moment is usually either not accounted for in a balance measurement or cannot be segregated from the total force depending on the measurement setup, and therefore may need a separate torque or load measurement device. More information on this effect can be found in the reference (Wickern, Zwicker, and Pfadenhauer 1997).

Bibliography

(CARB), California Air Resources Board (2008). *Initial Statement of Reasons for Proposed Rulemaking, Proposed Regulation for In-Use On-Road Diesel Vehicles, Appendix G: Emissions Analysis Methodology and Results*.

(EPA), United States Environmental Protection Agency (2016). *Final Rule for Phase 2 Greenhouse Gas Emissions Standards and Fuel Efficiency Standards for Medium- and Heavy-Duty Engines and Vehicles*.

Arora, P. and Z. Lyu (2016). "Aerodynamic Wind Tunnel in Passenger Car Application". MA thesis. Chalmers University of Technology.

Axerio, J. and G. Laccarino (2012). "An Aerodynamic Investigationof an Isolated Rotating Formula 1 Wheel Assembly". In: *Journal of Fluids Engineering*.

Axon, L. (1999). "The aerodynamic characteristics of automobile wheels—CFD prediction and wind tunnel experiment". PhD thesis. Cranfield University, Bedfordshire, UK.

Batchelor, G. K. (2000). *An Introduction to Fluid Dynamics*. Cambridge Mathematical Library. Cambridge University Press. DOI: 10.1017/CBO9780511800955.

Bearman, P. W., D. de Beer, E. Hamidy, and J. K. Harvey (1988). "The effect of a moving floor on wind-tunnel simulation of road vehicles". In: *Technical Paper 880245, Society of Automotive Engineers, Warrendale, PA*.

Berg, H. and A. Brandt (2018). "Investigation of Aerodynamic Wheel Design". MA thesis. Chalmers University of Technology.

Bolzon, M., S. Sebben, and A. Broniewicz (2019). "Effects of Wheel Configuration on the Flow Field and the Drag Coefficient of a Passenger Vehicle". In: *International Journal of Automotive Technology, Vol. 20, No. 4*, pp. 763–777.

Boslaugh, S. (2012). "Statistics in a Nutshell, Second Edition". In: ed. by M. Treseler. O'Reilly. Chap. The t-Test, pp. 155–168.

Brandt, A., H. Berg, M. Bolzon, and L. Josefsson (2019). "The Effects of Wheel Design on the Aerodynamic Drag of Passenger Vehicles". In: *SAE International Journal of Advances and Current Practices in Mobility*, pp. 1279–1299. DOI: https://doi.org/10.4271/2019-01-0662.

Cabral, B. and L. C. Leedom (1993). "Imaging Vector Fields Using Line Integral Convolution". In: *Proceedings of the 20th Annual Conference on Computer Graphics and Interactive Techniques*. SIGGRAPH '93. Anaheim, CA: Association for Computing Machinery, pp. 263–270. ISBN: 0897916018. DOI: 10.1145/166117.166151. URL: https://doi.org/10.1145/166117.166151.

Carr, G. (1988). "A Comparison of the Ground-Plane-Suction and Moving-Belt Ground-Representation Techniques". In: *SAE Technical Paper 880249*. DOI: https://doi.org/10.4271/880249.

Cavusoglu, O. M. (2017). "Aerodynamics Around Wheels and Wheel houses". MA thesis. Chalmers University of Technology.

Cogotti, A. (1983). "Aerodynamic characteristics of car wheels". In: *International Journal of Vehicle Design*, pp. 173–196.

Cooper, K. (1998). "Bluff-body blockage corrections in closed-and open-test-section wind tunnels". In: *Wind Tunnel Wall Correction (AGARD-AG-336), BFR Ewald, ed., Advisory Group for Aerospace Research and Development, North Atlantic Treaty Organization, Neuilly-sur-Seine Cedex, France*.

Cooper, K. R. (1993). "Bluff-body aerodynamics as applied to vehicles". In: *Journal of Wind Engineering and Industrial Aerodynamics* 49.1, pp. 1–21. ISSN: 0167-6105. DOI: 10.1016/0167-6105(93)90003-7. URL: https://www.sciencedirect.com/science/article/pii/0167610593900037.

Cooper, K. R. (2003). "Truck Aerodynamics Reborn - Lessons from the Past". In: *SAE International*. DOI: 10.4271/2003-01-3376. URL: https://doi.org/10.4271/2003-01-3376.

Cooper, K. R. (2004). "Commercial Vehicle Aerodynamic Drag Reduction: Historical Perspective as a Guide". In: *The Aerodynamics of Heavy Vehicles: Trucks, Buses, and Trains*. Ed. by R. McCallen, F. Browand, and J. Ross. Berlin, Heidelberg: Springer Berlin Heidelberg, pp. 9–28.

Cooper, K.R. (1984). "The wind-tunnel simulation of surface vehicles". In: *Journal of Wind Engineering and Industrial Aerodynamics* 17.2, pp. 167–198. ISSN: 0167-6105. DOI: https://doi.org/10.1016/0167-6105(84)90055-2. URL: https://www.sciencedirect.com/science/article/pii/0167610584900552.

Dimitriou, I. and S. Klussmann (2006). "Aerodynamic Forces of Exposed and Enclosed Rotating Wheels as an Example of the Synergy in the Development of Racing and Passenger Cars". In: *SAE Technical Paper 2006-01-0805*. DOI: https://doi.org/10.4271/2006-01-0805.

Duncan, B. D., S. Kandasamy, K. Sbeih, T. Lounsberry, and M. Gleason (2010). "Further CFD Studies for Detailed Tires using Aerodynamics Simulation with Rolling Road Conditions". In: *SAE Technical Paper 2010-01-0756*. DOI: https://doi.org/10.4271/2010-01-0756.

Eagles, N. and M. Cragun (2013). "A Parametric Assessment of Skirt Performance on a Single Bogie Commercial Vehicle". In: *SAE International Journal of Commercial Vehicles* 2, pp. 459–476. DOI: https://doi.org/10.4271/2013-01-2415.

Fackrell, J. E. (1974). "The Aerodynamics of an Isolated Wheel Rotating in Contact with the Ground". PhD thesis.

Fackrell, J. E. and J. K. Harvey (1973). "The Flowfield and Pressure Distribution of an Isolated Road Wheel". In: *Advances in Road Vehicle Aerodynamics*. Ed. by H.S. Stephens. BHRA Fluid Engineering, pp. 155–165.

Fackrell, J. E. and J. K. Harvey (1975). "The Aerodynamics of an Isolated Road Wheel". In: *Proceedings of the Second AIAA Symposium of Aerodynamics of Sports and Competition Automobiles*. Ed. by B. Pershing.

Fancher, P., C. Winkler, and M. Campbell (1992). *The Influence of Braking Strategy on Brake Temperatures in Mountain Descent*. Tech. rep. The University of Michigan Transportation Research Institute.

Figures, Transport in (2020). Tech. rep. Directorate-General for Mobility and Transport (European Commission).

Garner, H. C., E. W. Rogers, W. E. Acum, and EC Maskell (1996). "Subsonic wind tunnel wall corrections". In: *Advisory Group For Aerospace Research And Development Neuilly-Sur-Seine (France)*.

Hackett, J., J. Williams, J. Baker, and S. Wallis (1987). "On the Influence of Ground Movement and Wheel Rotation in Tests on Modern Car Shapes". In: *SAE Technical Paper 870245*. DOI: https://doi.org/10.4271/870245.

Hakansson, C. and M. J. Lenngren (2010). "CFD Analysis of Aerodynamic Trailer Devices for Drag Reduction of Heavy Duty Trucks". MA thesis. Chalmers University of Technology.

Hill, N., S. Finnegan, J. Norris, C. Brannigan, D.Wynn, H. Baker, and I. Skinner (2011). *Reduction and Testing of Greenhouse Gas Emissions from Heavy Duty Vehicles - Lot 1: Strategy (Recardo-AEA)*. Tech. rep. Final Report to European Commission - DG Climate Action.

Hucho, W. (1998). *Aerodynamics of Road Vehicles, fourth edition*. Society of Automotive Engineers.

Landman, Drew, Richard Wood, Whitney Seay, and John Bledsoe (Oct. 2009). "Understanding Practical Limits to Heavy Truck Drag Reduction". In: *SAE International Journal of Commercial Vehicles* 2.2, pp. 183–190. ISSN: 1946-391X. DOI: https://doi.org/10.4271/2009-01-2890. URL: https://doi.org/10.4271/2009-01-2890.

Leuschen, J. (2013). "The Effects of Ground Simulation on Tractor-Trailer Combinations". In: *SAE Int. J. Commer. Veh. 6(2)*. DOI: 10.4271/2013-01-2454.

Leuschen, J. and K. R. Cooper (2006). "Full-Scale Wind Tunnel Tests of Production and Prototype, Second-Generation Aerodynamic Drag-Reducing Devices for Tractor-Trailers". In: *SAE Technical Paper 2006-01-3456*. DOI: https://doi.org/10.4271/2006-01-3456.

McManus, James and Xin Zhang (Oct. 2005). "A Computational Study of the Flow Around an Isolated Wheel in Contact With the Ground". In: *J. Fluids Eng* 128.3, pp. 520–530. ISSN: 0098-2202. DOI: 10.1115/1.2175158. URL: https://doi.org/10.1115/1.2175158.

Mears, A. P., S. C. Crossland, and R. G. Dominy (2004). *An Investigation into the Flow-Field About an Exposed Racing Wheel*. DOI: 10.4271/2004-01-0446. URL: https://doi.org/10.4271/2004-01-0446.

Mears, A. P., R. G. Dominy, and D. B. Sims-Williams (Dec. 2002). "The Air Flow About an Exposed Racing Wheel". In: *SAE Technical Paper*. SAE International. DOI: 10.4271/2002-01-3290. URL: https://doi.org/10.4271/2002-01-3290.

Mercker, E. and H. Berneburg (1992). "On the simulation of road driving of a passenger car in a wind tunnel using a moving belt and rotating wheels". In: *Proceedings of 3rd international conference on innovation and reliability, Florence, Italy*.

Mercker, E. and J. Wiedemann (1996). "On the Correction of Interference Effects in Open Jet Wind Tunnels". In: *SAE TechnicalPaper; SAE International: Warrendale, PA, USA*.

Meszler, D., O. Delgado, F. Rodríguez, and R. Muncrief (2018). *EU HDVs: Cost Effectiveness of Fuel Efficiency Technologies for Long-Haul Tractor - Trailers in the 2025 - 2030 Timeframe*. Tech. rep. International Council on Clean Transportation.

Mihelic, R., D. Schaller, and M. Roeth (2016). *Confidence Report on Trailer Aerodynamic Device Solutions*. Tech. rep. North American Council for Freight Efficiency.

Morelli, A. (1969). "Aerodynamic Effects on an Automobile Wheel". In: *Technical Report Trans. 47/69, MIRA*.

Nigbur, J. E. (1999). "Characteristics of the wake downstream of an isolated automotive wheel". MA thesis. Cranfield University, Bedfordshire, UK.

Patten, J., B. McAuliffe, W. Mayda, and B. Tanguay (2012). *Review of Aerodynamic Drag ReductionDevices for Heavy Trucks and Buses*. Tech. rep. National Research Council Canada.

Peikert, R. (2007). *Vector Field Topology*. Tech. rep. URL: https://cgl.ethz.ch/teaching/former/scivis_07/Notes/Slides/08-topology.pdf.

Prasad, A. K. (2000). "Stereoscopic particle image velocimetry". In: *Experiments in Fluids* 29.2, pp. 103–116. ISSN: 1432-1114. DOI: 10.1007/s003480000143. URL: https://doi.org/10.1007/s003480000143.

Raffel, M., C. Willert, F. Scarano, C. Kähler, S. Wereley, and J. Kompenhans (2018). *Particle Image Velocimetry*. 3rd ed. Springer International Publishing. ISBN: 978-3-319-68851-0.

Rasani, M. R., A. Shamsudeen, Z. Harun, and W.M.F.W. Mahmood (2018). "A Computational Aerodynamic Study of Tandem Rotating Wheels in Contact with the Ground". In: *International Journal of Engineering and Technology*.

Rodríguez, F., R. Muncrief, O. Delgado, and C. Baldino (2017). *Market Penetration of Fuel Efficiency Technologies for Heavy-Duty Vehicles in the European Union, the United States, and China*. Tech. rep. International Council on Clean Transportation.

Saddington, A. J., R. D. Knowles, and K. Knowles (2007). "Laser Doppler anemometry measurements in the near-wake of an isolated Formula One wheel". In: *Experiments in Fluids* 42.5, p. 671. ISSN: 1432-1114. DOI: 10.1007/s00348-007-0273-7. URL: https://doi.org/10.1007/s00348-007-0273-7.

Scarano, F. (2013). *Course Reader for Flow Measurement Techniques (AE4-180)*. Tech. rep. Delft University of Technology.

Sciacchitano, A. (2014). "Uncertainty quantification in particle image velocimetry and advances in time-resolved image and data analysis". PhD thesis. Delft University of Technology.

Sciacchitano, A. and B. Wieneke (2016). "PIV uncertainty propagation". In: *Meas. Sci. Technol. 27 084006*.

Sharpe, B., O. Delgado, and N. Lutsey (2014). *Integrating Trailers into HDV Regulation: Benefit-Cost Analysis. International Council on Clean Transportation*. Tech. rep. International Council on Clean Transportation.

Sherwood, A. W. (1974a). "Wind Tunnel test of Trailmobile Trailers - 2nd Series". In: *University of Maryland Wind Tunnel Report No. 85 College Park, MD*.

Sherwood, A. W. (1974b). "Wind Tunnel test of Trailmobile Trailers." In: *University of Maryland Wind Tunnel Report No. 85 College Park, MD*.

Soloff, S. M., R. J. Adrian, and Z. C. Liu (Dec. 1997). "Distortion compensation for generalized stereoscopic particle image velocimetry". In: *Measurement Science and Technology* 8.12, pp. 1441–1454. DOI: 10.1088/0957-0233/8/12/008. URL: https://doi.org/10.1088/0957-0233/8/12/008.

Stapleford, W. R. and G. W. Carr (1970). "Aerodynamic Characteristics of Exposed Rotating Wheels". In: *Technical Report 1970/2, MIRA*.

Stephens, Richard and Holger Babinsky (Apr. 2016). "An Experimental Study on Truck Side-Skirt Flow". In: *SAE International Journal of Passenger Cars - Mechanical Systems* 9. DOI: 10.4271/2016-01-1593.

Stephens, Richard G., Patrick R.R.J. Stevens, and Holger Babinsky (Sept. 2016). "A Method for Truck Underbody Aerodynamic Investigation". In: *SAE International Journal of Commercial Vehicles* 9.2, pp. 429–437. ISSN: 1946-391X. DOI: https://doi.org/10.4271/2016-01-9020. URL: https://doi.org/10.4271/2016-01-9020.

Terra, W., A. Sciacchitano, and F. Scarano (2016). "Aerodynamic drag of transiting objects by large-scale tomographic PIV". In: *Proceedings of the 18th International Symposium on the Application of Laser and Imaging Techniques to Fluid Mechanics*.

Van Oudheusden, B.W. (2013). "PIV-based pressure measurement". In: *Measurement Science and Technology, 24, 1-32.*

Van Raemdonck, G. M. R. (2006). "Design of an aerodynamic aid for a tractor-trailer combination". MA thesis. Delft University of Technology.

Van Raemdonck, G. M. R. (2012). "Design of Low Drag Bluff Road Vehicles". PhD thesis. Delft University of Technology.

Wäschle, Alexander (Apr. 2007). "The Influence of Rotating Wheels on Vehicle Aerodynamics - Numerical and Experimental Investigations". In: *SAE World Congress and Exhibition*. SAE International. DOI: https://doi.org/10.4271/2007-01-0107. URL: https://doi.org/10.4271/2007-01-0107.

Wäschle, Alexander, Stephane Cyr, Timo Kuthada, and Jochen Wiedemann (Mar. 2004). "Flow around an Isolated Wheel - Experimental and Numerical Comparison of Two CFD Codes". In: *SAE Technical Paper*. SAE International. DOI: 10.4271/2004-01-0445. URL: https://doi.org/10.4271/2004-01-0445.

Westerweel, J (Dec. 1997). "Fundamentals of digital particle image velocimetry". In: *Measurement Science and Technology* 8.12, pp. 1379–1392. DOI: 10.1088/0957-0233/8/12/002. URL: https://doi.org/10.1088/0957-0233/8/12/002.

Westerweel, J., F. Scarano, B. McKeon, G. Comte-Bellot, J. Foss, C. Tropea, J. Meyers, J. Lee, A. Cavone, R. Schodl, M. Koochesfahani, Y. Andreopoulos, W. Dahm, J. Mullin, J. Wallace, P. Vukoslavčević, S. Morris, E. Pardyjak, and A. Cuerva (2007). "Velocity, Vorticity, and Mach Number". In: *Springer Handbook of Experimental Fluid Mechanics*. Ed. by C. Tropea, A. L. Yarin, and J. Foss. Berlin, Heidelberg:

Springer Berlin Heidelberg, pp. 215–471. ISBN: 978-3-540-30299-5. DOI: 10.1007/978-3-540-30299-5_5. URL: https://doi.org/10.1007/978-3-540-30299-5_5.

Wickern, G., K. Zwicker, and M. Pfadenhauer (1997). "Rotating Wheels - Their Impact on Wind Tunnel Test Techniques and on Vehicle Drag Results". In: *SAE Technical Paper 970133*.

Wieneke, B. (2005). "Stereo-PIV using self-calibration on particle images". In: *Experiments in Fluids (2005) 39: 267-280*.

Wood, R. (2012). "EPA Smartway Verification of Trailer Undercarriage Advanced Aerodynamic Drag Reduction Technology". In: *AE Int. J. Commer. Veh. 5(2):2012*. DOI: 10.4271/2012-01-2043.